Series 01 Aerodynamics 10

Prediction of Bypass Transition with Differential Reynolds Stress Models

K.J.A. Westin/R.A.W.M. Henkes

Delft University Press

Prediction of Bypass Transition with Differential Reynolds Stress Models

Series 01: Aerodynamics 10

Prediction of Bypass Transition with Differential Reynolds Stress Models

K.J.A. Westin/R.A.W.M. Henkes

Delft University Press / 1998

Published and distributed by:

Delft University Press
Mekelweg 4
2628 CD Delft
The Netherlands
Telephone +31 (0)15 278 32 54
Fax +31 (0)15 278 16 61
e-mail: DUP@DUP.TUDelft.NL

by order of:

Faculty of Aerospace Engineering
Delft University of Technology
Kluyverweg 1
P.O. Box 5058
2600 GB Delft
The Netherlands
Telephone +31 (0)15 278 14 55
Fax +31 (0)15 278 18 22
e-mail: Secretariaat@LR.TUDelft.NL
website: http://www.lr.tudelft.nl/

Cover: Aerospace Design Studio, 66.5 x 45.5 cm, by:
Fer Hakkaart, Dullenbakkersteeg 3, 2312 HP Leiden, The Netherlands
Tel. +31 (0)71 512 67 25

90-407-1573-4

Printed in The Netherlands

Contents

Chapter 1

Introduction

Laminar-turbulent transition is a physical phenomena that is not only of great scientific interest, but also of large practical importance in many industrial applications. The significant increase in friction drag and heat transfer in turbulent flows as compared to laminar flows, makes it important to know where precisely the transition takes place. Although transition has been studied for more than a century, beginning with the pioneering work by Reynolds (1883), it is still not well understood. Due to the large range of possible disturbance sources and the different ways in which these disturbances can grow, the transition process becomes a very intricate problem to study.

Usually one can divide the transition process into three sub topics: receptivity, disturbance growth and breakdown. If we restrict our attention to boundary layer flows, receptivity refers to the possible ways in which disturbances can enter into the boundary layer. Examples of disturbance sources can be vibrations, surface roughnesses, sound, free stream turbulence etc. Depending on the characteristics and the amplitudes of the disturbances, the downstream development can take different routes. The most well documented transition scenario is the exponential growth of initially small amplitude waves, i.e. Tollmien-Schlichting waves, which at relatively low amplitudes (1-2%) become affected by non-linear interactions followed by a rapid breakdown to turbulence. The growth of these waves can with good accuracy be described by linear theory, which is the basis for the presently dominating prediction method for transition, the so-called e^N-method. The relative success obtained with this method at small outer disturbance levels can be ascribed to the long region with slowly growing wave amplitudes which dominates the transition process, compared with the rapid non-linear breakdown.

However, in many applications the initial amplitude of the disturbances is fairly large, and the e^N-method, which is based on linearized equations, will fail to serve as a prediction tool for transition. The notation *by-pass transition* was first introduced by Morkovin (1969), when he suggested that the TS-wave route to transition could be by-passed if it could be replaced by another strongly amplifying mechanism. By-pass transition has later become an expression often used when traditional linear instability mechanisms, like TS-waves or cross-flow vortices, are not recognized as being of primary importance in the transition process. However, the ongoing progress in the understanding of transition has led to a more strict definition of by-pass transition: "transition emanating from linear mechanisms other than exponential instabilities" (Henningson 1994).

One essential object of transition research is to develop prediction methods which rely on a sound description of the essential dynamics in the boundary layer. Although much

knowledge about transition at higher disturbance levels has been added during the last years, such prediction methods can not be expected within the near future. However, there is an increasing demand of improved methods for predicting transition in industrial applications, where the dominating methods that are used today are still based on empirical correlations. In many internal flows, for example turbomachinery applications, the disturbance levels can be of the order of 10-20%. This is the case in for instance gas-turbines, where the stator blades generate disturbances which affect the boundary layer on the rotor blades. In order to efficiently design the turbine it is of great importance to know how the boundary layer characteristics vary along the chord of the blades. It should be emphasized that a correct modelling of the behaviour inside the transition region is as important as the knowledge of where transition starts, since a predominant part of the turbine blades can be affected by transitional flow.

During the last years there has been some ongoing research on the possibilities to use turbulence models for transition prediction at high levels of free stream turbulence. Since 1990 the efforts have been organized by Dr. A.M. Savill as a special interest group within ERCOFTAC (the European Research Community On Flow Turbulence And Combustion), and an overview of the achievements so far is reported in Savill (1995b). The majority of the studies have been focussed on different eddy-viscosity models, sometimes modified to include empirical information concerning the start of the transition region. The results shown so far reveal large differences between different models, but in some cases the reported results exhibit reasonable agreement for a wide range of experimental test cases. The results indicate that the use of turbulence models as a prediction tool might be a possibility which has to be further investigated.

The use of turbulence models for transition prediction is also the topic of the present report, in which some models, mainly differential Reynolds stress models, have been tested. In chapter 2 some important experimental observations are shown, which intend to illustrate the characteristics of the disturbances that are induced in the boundary layer by the FST. Also, some of the general shortcomings associated with the approach of using turbulence models are discussed. The basic equations and the turbulence models are described in chapter 3, and some details concerning the numerical schemes are given in chapter 4. The different test cases are described in chapter 5, and, finally, the results from the calculations can be found in chapter 6.

Chapter 2

Experimental results

During the last years there has been a considerable interest in studying the influence of free stream turbulence (FST) on boundary layer transition. Experiments as well as numerical simulations and theoretical studies have been undertaken, leading to an increased knowledge about the disturbances that are induced into the laminar boundary layer and their downstream development. The present chapter intends to give a short summary of some of the characteristics of these disturbances, which can be of importance when later considering the application of turbulence models. In the following the streamwise, wall-normal and spanwise directions are denoted by x, y and z respectively, and the corresponding fluctuating velocity components by u, v and w.

2.1 Low-frequency fluctuations

A general observation from a number of experiments is the large difference in spectral distribution of the disturbances that are induced in the laminar boundary layer, as compared with the free stream turbulence (see for instance Arnal & Juillen 1978; Kendall 1985; Westin *et al.* 1994). This can easily be observed from the hot-wire traces shown in figure 2.1, measured in a zero pressure gradient boundary layer at a free stream turbulence level (Tu) of 1.5%. While the free stream turbulence consists of a wide range of frequencies and wave numbers, the induced boundary layer disturbances are dominated by large amplitude, low-frequency fluctuations in the streamwise component. The fluctuations are also very different from those in a turbulent boundary layer, which can be observed in figure 2.2. The plot shows profiles of the energy contribution to $\overline{uu}$ filtered in narrow frequency bands, measured at positions upstream and downstream of the transition region. At the upstream location there is a significant energy growth in the lower frequencies inside the boundary layer, while the contributions to higher frequencies are continuously damped towards the wall. In contrast, the fully turbulent boundary layer exhibits high frequency contributions also in the near-wall region.

During the downstream development, the disturbances grow in amplitude at a rate proportional to the displacement thickness (δ^*), and can attain values of the order of 10-15% of the free stream velocity (U_0) before transition occurs. It should be emphasized that, despite the large perturbation amplitudes, the boundary layer has still characteristics close to the unperturbed boundary layer. Both the shape factor and the wall shear stress are close to the Blasius values, although a small deviation in the mean profiles can be observed

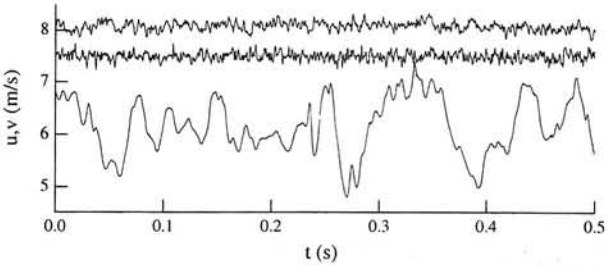

Figure 2.1: Hot-wire traces measured inside and outside a laminar boundary layer subjected to a FST-level of 1.5%. The traces are from top to bottom: u-component in the free stream, v-component in the free stream (note: $v_{plot} = v + 7.5$) and u inside the boundary layer.

due to the growing disturbances. Moreover, there is no turbulent intermittency in the measured signal. The pre-transitional region of the boundary layer is sometimes referred to as a "pseudo-laminar" boundary layer.

Another important observation is the fairly strong spanwise correlation that can be measured inside the boundary layer (figure 2.3). The strong negative correlation reveals the existence of structures which have a preferred spanwise scale. These structures appear irregularly in time and space, which means that they can not be detected by simply measuring the rms-value at different spanwise positions. If a typical streamwise scale of the disturbances is estimated from the energy spectra measured in the boundary layer, it becomes clear that the structures must be very long in comparison to the spanwise scale obtained from the correlation. While moving downstream the major energy content in the spectra is shifted towards lower frequencies, indicating that the streamwise length of the structures is increasing during the downstream development. The above findings have also been verified in flow visualizations (Kendall 1985; Gulyaev *et al.* 1989; Alfredsson & Matsubara 1996), in which long and narrow streaky structures have been observed.

An interesting comparison can be made with a recent experiment by Bakchinov *et al.* (1995). The aim of the experiment was to generate a localized free stream disturbance which could serve as a model for a free stream vortex impinging onto the boundary layer. The localized disturbance resulted in a set of high-velocity and low-velocity streaks inside the boundary layer, and the streaks were elongated in the streamwise direction due to the mean shear. It seems likely that the low frequency fluctuations observed in laminar boundary layers subjected to FST originate from similar streaks generated by free stream vortices. However, in the case of FST this generation is random both in time and space, thus leading to a fluctuating signal when measured with a fixed hot-wire probe in the boundary layer. One can also expect that the continuous forcing from the free stream, as well as interactions between adjacent streaks, can affect the downstream development in the case of FST. From the experimental results one can conclude that the perturbations observed in the pseudo-laminar boundary layer are not what we usually call turbulence. The fluctuations do not contain the wide range of scales normally observed in turbulence, but should rather be considered as an irregular movement of large-scale structures in the boundary layer.

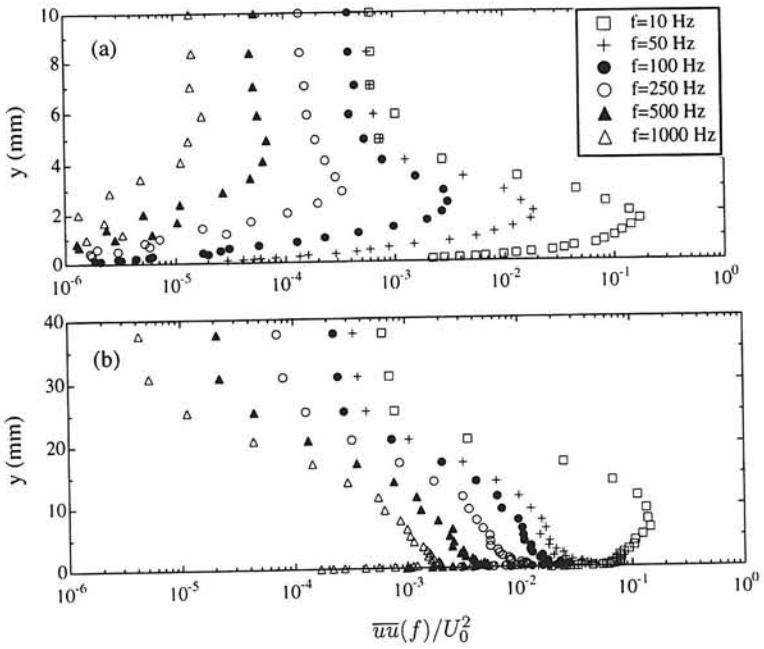

Figure 2.2: Profiles of fluctuating energy in narrow frequency bands. (a) Laminar region ($R = 1.72\,(Re_x)^{1/2} = 1.72\,(U_0 x/\nu)^{1/2} = 1080$); (b) turbulent region ($R = 2050$). $U_0 = 11.9$ m/s; $Tu = 1.5\%$. (Matsubara, 1995, unpublished).

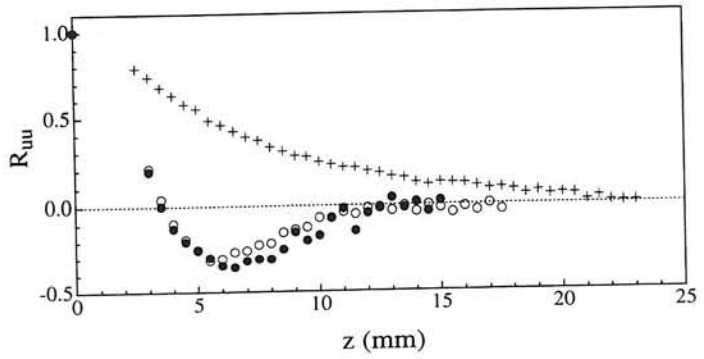

Figure 2.3: Spanwise correlations in the boundary layer, measured close to the maximum of u_{rms}: $x = 500$ mm ($R = 890$) ($\circ$), $x = 1000$ mm ($R = 1260$) ($\bullet$). Spanwise correlation in the free stream ($x = 500$ mm) (+). (From Westin *et al.*, 1994, measured at $Tu = 1.5\%$)

2.1.1 Some theoretical results

The fact that longitudinal, streaky structures can be observed in the pseudo-laminar boundary layer may be corroborated by recent studies on transient growth. In order to get transition at subcritical Reynolds numbers (i.e. when linear stability analysis predicts stable eigenmodes) it was shown by Henningson & Reddy (1994) that there must be an underlying linear growth mechanism. This elucidates the importance of recent studies on transient growth, which are based on eigenmodes to the linearized Navier-Stokes operator. Although individual modes are damped, the combination of non-orthogonal modes can result in significant transient energy growth. Butler & Farrell (1992) studied transient growth in the Blasius boundary layer (using the parallel flow assumption), and found that the optimal initial disturbance is a streamwise vortex. Optimal disturbance means in this case the initial conditions that gain the most energy over a specified time period. Although the vortex itself is damped, it forces transiently growing high and low velocity streaks in the u-component. The streaks are generated by the wall-normal movement of fluid elements that conserve their horizontal momentum, which is an inviscid mechanism that was originally denoted as *lift-up* by Landahl (1975).

However, although the growth mechanism is linear, a non-linear mechanism is necessary in order to generate the initial streamwise vortex. This can efficiently be done in shear flows by generating two oblique waves, which non-linearly transfer energy to the streamwise vortex. The same idea has been used in studies of boundary layer receptivity to free stream disturbances. In direct numerical simulations by Berlin & Henningson (1994), oblique waves were generated in the free stream above a flat plate boundary layer. Also in this case longitudinal streaks were formed inside the boundary layer.

Although it is not clear yet how the low-frequency fluctuations in the boundary layer are generated, it is encouraging that the structures observed in the experiments are similar to those that are predicted to be the transiently most growing disturbances. It is also plausible to expect that the wide range of frequencies and wave lengthes observed in free stream turbulence include energy in the wave lengthes close to the optimal disturbance for transient growth. However, the disturbances will at some point start to decay, unless the initial amplitude exceeds a certain threshold level which results in transition. Furthermore, the effect of the continuous forcing from the FST along the boundary layer edge is not clearly understood. In experiments at moderate and high levels of FST (larger than 0.5–1%), the rms-level in the pseudo-laminar layer is continuously growing during the downstream development. Whether this growth is due to a continuous forcing of disturbances that are introduced into the boundary layer in the leading edge region, or due to the generation of new and stronger disturbances at downstream positions, is an issue that deserves further experimental and numerical investigation.

2.2 Scaling of fluctuating profiles

As previously mentioned, the measured disturbances grow in amplitude while moving downstream, resulting in very large fluctuation levels. The fluctuations are mainly in the u-component, while the v-component is of the order of 5 to 10 times smaller. Further, the maximum amplitude appears approximately in the middle of the boundary layer, which is different from the turbulent boundary layer where the maximum in u_{rms} is positioned close to the wall. These features can be observed from the u_{rms} and v_{rms} profiles shown in figure 2.4.

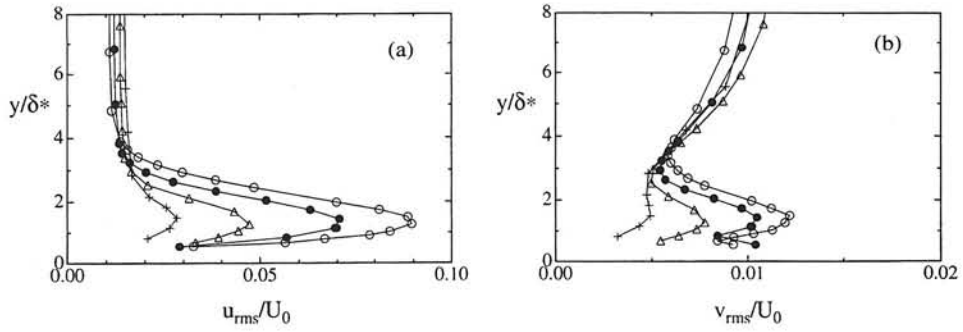

Figure 2.4: Profiles of (a) u_{rms} and (b) v_{rms} in the pseudo-laminar boundary layer at $Tu = 1.5\%$ ($U_0 = 8$ m/s). The different x-positions are 100 mm (+), 250 mm (△), 500 mm (•) and 800 mm (○).

Also the wall-normal behaviour of the two components is quite different. For the streamwise component the fluctuating amplitude is fairly constant throughout the free stream, but it increases inside the boundary layer due to the low-frequency fluctuations. The $\overline{uv}$-Reynolds stresses have a similar behaviour, with a zero contribution in the free stream and a non-zero value mainly restricted to the boundary layer (not shown). This is also expected as the $\overline{uv}$-correlation represents the mixing inside the shear layer. However, this behaviour is not relevant for the wall-normal fluctuations, which start to decay outside the boundary layer edge. In figure 2.4 the y-axis is scaled with the displacement thickness (δ^*), which means that the boundary layer thickness (δ_{99}) corresponds to approximately $3\delta^*$. The v_{rms}-level starts to decrease at least three boundary layer thicknesses above the plate, and is continuously damped towards the boundary layer edge. Inside the layer a small local maximum can be observed, which is caused by the low-frequency fluctuations. The damping outside the boundary layer is caused by wall-reflections in the plate, and the size of the affected region is dependent on the dominating scales in the free stream turbulence. In most experiments grid generated turbulence is used, which is allowed to decay for a distance in order to obtain isotropy and homogeneity before reaching the model. This usually results in an energy distribution dominated by fairly large scales, thus giving a large region which is affected by the wall-reflection.

The damping of v-fluctuations outside the boundary layer is important to take into account in calculations. The importance is substantiated by results obtained from large-eddy simulations by Yang & Voke (1993). They computed transition on a flat plate subjected to approximately 5.5% FST, while changing the characteristics of the incoming turbulence. By generating one dimensional fluctuations at the inlet, they showed that the wall-normal fluctuations had the major influence on the location of the transition region. While v-disturbances resulted in transition close to the position obtained for isotropic turbulence, w-disturbances gave a delayed transition and the test with fluctuations only in the u-component did not result in transition at all. Consequently, a reduced v_{rms}-level close to the boundary layer edge has a delaying effect on the transition process. This is intuitively an expected result, since a wall-normal motion will more easily penetrate and displace fluid in the boundary layer, and thus more efficiently induce disturbances, than motions in the horizontal plane. The same conclusion can also be drawn from the experiments by Bakchinov *et al.* (1995), in

which a strong negative v-perturbation in the localized free stream disturbance resulted in the generation of strong u-perturbations in the boundary layer.

2.3 Breakdown

So far only results for the pseudo-laminar boundary layer have been shown, i.e. upstream of the region where turbulent spots become frequent and the boundary layer breaks down into turbulence. The breakdown phase of a boundary layer subjected to FST is not so well-understood, although there are indications that the breakdown is initiated by secondary instabilities of the longitudinal streaks. In a recent flow visualization of boundary layer transition at $Tu = 6.6\%$ by Alfredsson & Matsubara (1996), it was clearly seen that the longitudinal streaks began to oscillate in the spanwise direction just prior to breakdown.

Similar secondary instabilities have been observed in Direct Numerical Simulations of by-pass transition. In a simulation by Berlin, Lundbladh & Henningson (1994), starting with oblique waves in a Blasius boundary layer, longitudinal streaks were generated which finally broke down due to secondary instabilities. Similar spanwise oscillations of the streaks prior to breakdown have been observed in simulations of by-pass transition in Poiseuille flow (Lundbladh, Henningson & Reddy 1994) and Couette flow (Kreiss, Lundbladh & Henningson 1994). Based on the above findings, Berlin *et al.* (1994) conjectured that the following stages are universal for oblique transition in all shear flows: nonlinear generation of streamwise vortices by the oblique waves which are initially introduced into the flow, followed by transient growth of streaks due to the streamwise vortices, and finally a breakdown of the streaks associated with secondary instabilities.

Another experimental observation concerning the breakdown phase in transition induced by free stream turbulence was made by Boiko *et al.* (1994), who studied a boundary layer subjected to a FST-level of 1.5%. It was shown that the transition process was significantly enhanced if a small amplitude TS-wave was introduced, although it was not possible to see if this resulted in secondary instabilities of the streaks. However, further quantitative measurements on the breakdown phase, as well as new model experiments of possible secondary instabilities of streaks, are necessary in order to gain more insight into which mechanisms are responsible for the breakdown. For the time being, it is also unknown how the streaks develop in the presence of pressure gradients.

2.4 Can turbulence models be applied?

Before proceeding to the main topic of this report, one should address the following question: What are the prospects to succeed in predicting transition at high levels of FST by using Reynolds Averaged Navier-Stokes equations (RANS) together with one point closures for the modelling of the Reynolds stresses? One of the basic assumptions in one point closures is the self-similarity of the spectra of the turbulent energy, which is determined by one single length scale. This means that if individual spectral modes are crucial for transition, this can not be captured by a turbulence model. Further, the picture that emerges from the present chapter is a pseudo-laminar boundary layer distorted mainly by large-scale, three-dimensional (3D) structures which appear irregularly both in time and space. The importance of 3D-disturbances is a general result from most studies on subcritical transition. The present approach assumes a 2D state after time averaging. This is also in agreement with experimental

findings, but the model might fail if spectral information (both in time and spanwise direction) is important. Consequently, there might be some doubt whether a statistical turbulence model can perform well when different test cases are considered.

However, one can expect that when the free stream turbulence level is raised, the transition process becomes faster and the importance of individual spectral modes may become less important. In that case the simplification we make when using Reynolds-averaged Navier-Stokes equations will probably be more accurate, or at least the error we introduce will be less observable. Thus we can assume that above a certain, still unknown, lower limit of Tu the use of turbulence models for transition prediction can be justified, at least as an engineering tool. It can be difficult to estimate the lower level of Tu for which the models can be used, but a level of 1% or less is most likely outside the range of applicability, as the influence from TS-waves usually becomes significant.

Chapter 3

Equations and Models

3.1 Governing equations

The instantaneous pressure and velocity field in fluid flow is described by the well-known Navier-Stokes equations, which can be derived by applying Newton's second law to a fluid element. For an incompressible Newtonian fluid these equations read

$$\frac{\partial \tilde{U}_i}{\partial t} + \tilde{U}_j \frac{\partial \tilde{U}_i}{\partial x_j} = -\frac{1}{\rho}\frac{\partial \tilde{P}}{\partial x_i} + \nu \frac{\partial^2 \tilde{U}_i}{\partial x_j \partial x_j} \tag{3.1}$$

$$\frac{\partial \tilde{U}_i}{\partial x_i} = 0 \tag{3.2}$$

where equation 3.1 and 3.2 describe conservation of momentum and mass (continuity equation) respectively. Although the equations are valid both for laminar and turbulent flows, they are in most practical problems impossible, or at least too expensive, to solve directly. It is often convenient to make a Reynolds decomposition, i.e. the velocity and pressure fields are divided into a mean and a fluctuating part. Generally the mean part should be an ensemble average of the flow, but in many cases the flow is quasi steady and a time average can be used instead. Thus, if U_i and P denote the mean parts and u_i and p the fluctuating parts, the following decompositions

$$\tilde{U}_i = U_i + u_i \quad \text{and} \quad \tilde{P} = P + p$$

are substituted into equations 3.1 and 3.2. After averaging the so-called Reynolds-averaged Navier-Stokes equations (or shorter Reynolds equations) are obtained:

$$\frac{\partial U_i}{\partial t} + U_j \frac{\partial U_i}{\partial x_j} = -\frac{1}{\rho}\frac{\partial P}{\partial x_i} + \frac{\partial}{\partial x_j}(\nu \frac{\partial U_i}{\partial x_j} - \overline{u_i u_j}) \tag{3.3}$$

$$\frac{\partial U_i}{\partial x_i} = 0 \tag{3.4}$$

A new term appears in the right hand side of equation 3.3, in which the overbar denotes an averaged quantity and $\overline{u_i u_j}$ represent correlations between the fluctuating components. This term can be interpreted as an additional stress in the momentum equation, and describes the mean transfer of momentum due to the turbulent fluctuations. However, the Reynolds stress tensor ($\tau_{ij} = -\rho\overline{u_i u_j}$) includes six new unknown correlations which need to be calculated or

modelled in order to close equation 3.3. An equation for $-\overline{u_i u_j}$ can be derived by subtracting equation 3.3 from 3.1 and multiplying the result by u_j. If the obtained equation is averaged and added to the same equation, but with the indices $_i$ and $_j$ interchanged, the Reynolds stress transport equation can be obtained after some manipulations:

$$\frac{\partial \overline{u_i u_j}}{\partial t} + U_k \frac{\partial \overline{u_i u_j}}{\partial x_k} = -\left(\overline{u_i u_k} \frac{\partial U_j}{\partial x_k} + \overline{u_j u_k} \frac{\partial U_i}{\partial x_k} \right) + \overline{\frac{p}{\rho} \left(\frac{\partial u_i}{\partial x_j} + \frac{\partial u_j}{\partial x_i} \right)}$$
$$-2\nu \left(\overline{\frac{\partial u_i}{\partial x_k} \frac{\partial u_j}{\partial x_k}} \right) + \frac{\partial}{\partial x_k} \left[-\overline{u_i u_j u_k} - \overline{\frac{p}{\rho} (u_i \delta_{jk} + u_j \delta_{ik})} + \nu \frac{\partial \overline{u_i u_j}}{\partial x_k} \right] \tag{3.5}$$

The different terms on the right hand side of the equation describe successively turbulent production ($\mathcal{P}_{ij}$), energy redistribution between components (pressure-strain, ϕ_{ij}), dissipation ($-\epsilon_{ij}$) and a transport term (d_{ij}). The last term (d_{ij}) includes transport due to turbulent velocity fluctuations, pressure fluctuations and viscous diffusion. It should be mentioned that the viscosity related terms and the terms including pressure fluctuations can be split in other ways, but the above equation is the form most frequently seen in the literature.

A scalar equation for the turbulent kinetic energy ($k = \overline{u_i u_i}/2$) can be obtained by contracting indices in equation 3.5 and divide the result by two. The k-equation reads

$$\frac{\partial k}{\partial t} + U_k \frac{\partial k}{\partial x_k} = -\overline{u_i u_k} \frac{\partial U_i}{\partial x_k} - \nu \left(\overline{\frac{\partial u_i}{\partial x_k} \frac{\partial u_i}{\partial x_k}} \right) + \frac{\partial}{\partial x_k} \left[-\frac{1}{2} \overline{u_i u_i u_k} - \overline{\frac{p}{\rho} u_k} + \nu \frac{\partial k}{\partial x_k} \right] \tag{3.6}$$

The different terms on the right hand side can be denoted with $\mathcal{P}$, $-\epsilon$ and d. Note that the pressure strain term disappears, as it only represents a redistribution of energy among the components and therefore has a zero trace. In many turbulence models a separate equation for the (homogeneous) dissipation is solved. The exact equation for ϵ reads:

$$\frac{\partial \epsilon}{\partial t} + U_k \frac{\partial \epsilon}{\partial x_k} = -2\nu \left(\overline{\frac{\partial u_i}{\partial x_k} \frac{\partial u_j}{\partial x_k}} + \overline{\frac{\partial u_k}{\partial x_i} \frac{\partial u_k}{\partial x_j}} \right) \frac{\partial U_i}{\partial x_j} - 2\nu \overline{u_j \frac{\partial u_i}{\partial x_k} \frac{\partial^2 U_i}{\partial x_j \partial x_k}}$$
$$-2\nu \overline{\frac{\partial u_i}{\partial x_j} \frac{\partial u_i}{\partial x_k} \frac{\partial u_j}{\partial x_k}} - 2 \overline{\left(\nu \frac{\partial^2 u_i}{\partial x_j \partial x_k} \right)^2} + \nu \frac{\partial}{\partial x_k} \left[-\overline{u_k \epsilon} - \frac{2}{\rho} \overline{\frac{\partial p}{\partial x_i} \frac{\partial u_k}{\partial x_i}} + \frac{\partial \epsilon}{\partial x_k} \right] \tag{3.7}$$

The first two terms on the right hand side can be interpreted as production terms due to the mean strain field, while the third term describes production caused by vortex stretching. The fourth term is a viscous destruction term, and finally there is a transport term which as usual includes turbulent transport, pressure transport and viscous diffusion.

3.2 Turbulence modelling

The aim of turbulence modelling is to solve the closure problem that appears in the Reynolds equation (3.3), in which the Reynolds stress tensor must be determined. Even if new equations are derived in order to calculate $\overline{u_i u_j}$, new unknown higher-order correlations will appear, and modelling will always be necessary at some level. The simplest approach is to model the Reynolds stress tensor directly. This is usually done by introducing an eddy-viscosity (ν_t) which directly relates $\overline{u_i u_j}$ to the mean strain field. Zero-, one- and two-equation models

are based on the eddy-viscosity concept, but they use different levels of approximation to determine ν_t. Most eddy-viscosity models use a linear relation between $\overline{u_i u_j}$ and the mean strain field, which has the disadvantage that in simple shear flows the models predict more or less isotropic turbulence. An improvement in this respect can be achieved by using non-linear eddy-viscosity models, which still have a relatively low computational cost.

The next higher level of complexity is to solve a transport equation for each independent component in the Reynolds stress tensor, which means that $\overline{u_i u_j}$ is not modelled directly, but instead different terms in the transport equations are modelled. This group of models is usually called Reynolds stress models or second-moment closures. A common notation for both eddy-viscosity models and Reynolds stress models is one-point closures, which means that they use spectral information only from one point in space. Consequently they make use of only one characteristic length scale of the turbulence. Although there is ongoing research on more sophisticated models incorporating space-correlations in the modelling (so-called two-point closures), these models are far too complex for being a realistic alternative in engineering applications. In the present work a two-equation, linear eddy-viscosity model and two different Reynolds stress models have been tested in transitional test cases. The essential characteristics of the models are described in the following sections.

3.2.1 $k-\epsilon$ models

The most frequently used group of turbulence models is $k-\epsilon$ models, which are eddy-viscosity models where the characteristic velocity and length scale are determined from transport equations for k and ϵ. The linear relation between $\overline{u_i u_j}$ and the mean strain field as formulated by Boussinesq (1877) reads:

$$\frac{\tau_{ij}}{\rho} = -\overline{u_i u_j} = \nu_t\left(\frac{\partial U_i}{\partial x_j} + \frac{\partial U_j}{\partial x_i}\right) - \frac{2}{3}\delta_{ij}k \tag{3.8}$$

The eddy-viscosity is usually considered as a product of a typical velocity and length scale. In the $k-\epsilon$ model the velocity scale is given by $\sqrt{k}$ and the length scale by $k^{3/2}/\epsilon$, which leads to:

$$\nu_t = c_\mu f_\mu \frac{k^2}{\epsilon} \tag{3.9}$$

The constant c_μ is a model parameter and f_μ is a low-Reynolds-number function which is included to reduce ν_t close to solid surfaces. The k- and ϵ-equation are usually modelled as:

$$\frac{\partial k}{\partial t} + U_k\frac{\partial k}{\partial x_k} = \mathcal{P} - \epsilon + \frac{\partial}{\partial x_k}\left[\left(\nu + \frac{\nu_t}{\sigma_k}\right)\frac{\partial k}{\partial x_k}\right] + D \tag{3.10}$$

$$\frac{\partial \epsilon}{\partial t} + U_k\frac{\partial \epsilon}{\partial x_k} = c_{\epsilon 1} f_{\epsilon 1}\mathcal{P}\frac{\epsilon}{k} - c_{\epsilon 2} f_{\epsilon 2}\frac{\epsilon^2}{k} + \frac{\partial}{\partial x_k}\left[\left(\nu + \frac{\nu_t}{\sigma_\epsilon}\right)\frac{\partial \epsilon}{\partial x_k}\right] + E \tag{3.11}$$

in which

$$\mathcal{P} = \frac{\tau_{ij}}{\rho}\frac{\partial U_i}{\partial x_j}$$

For the "standard" $k-\epsilon$ model, in which the constants are determined such that the model performs well in regions with relatively high turbulence levels, the constants take the values $c_\mu = 0.09$, $c_{\epsilon 1} = 1.44$, $c_{\epsilon 2} = 1.92$, $\sigma_k = 1.0$, $\sigma_\epsilon = 1.3$, $f_\mu = f_{\epsilon 1} = f_{\epsilon 2} = 1.0$ and $D = E = 0$.

Low-Reynolds number modifications

In the case of wall-bounded flows the near wall region needs special treatment, as the viscosity effects become more important and the turbulent Reynolds number reduces to zero at the wall. A possible solution is to use the standard model, but with the first grid point positioned at a certain distance from the wall. The boundary conditions at the first grid point are determined by using the law of the wall, based on the assumption of quasi-equilibrium turbulence. However, in many cases it is desirable to solve the equations down to the wall, which requires some modifications of the turbulence model in order to fulfil the kinematic constraints. The behaviour close to the wall can be estimated by a Taylor expansion in y, where the leading terms for the different quantities are proportional to the following powers of y:

$$u \sim y, \quad v \sim y^2 \quad w \sim y, \quad uv \sim y^3$$
$$\epsilon \sim 2\nu \left(\frac{\partial \sqrt{k}}{\partial y} \right)^2$$

As can be observed, the dissipation has a finite and non-zero value close to the wall. If equation 3.11 is applied directly, the term $c_{\epsilon 2} f_{\epsilon 2} \epsilon^2 / k \rightarrow \infty$ as k is reduced to zero at the wall. A common way to overcome this problem is to use the variable $\tilde{\epsilon}$ instead of ϵ, where $\tilde{\epsilon}$ is defined as

$$\tilde{\epsilon} = \epsilon - 2\nu \left(\frac{\partial \sqrt{k}}{\partial y} \right)^2$$

The use of $\tilde{\epsilon}$ in equations 3.10 and 3.11 (i.e. change all ϵ to $\tilde{\epsilon}$ in the equations) implies the need of an extra term (D) in the k-equation, in order to get the correct dissipation. The low-Reynolds number $k-\epsilon$ model that has been used in the present study is the model by Launder & Sharma (1974). The model has shown to perform fairly well in a number of transitional test cases, and is currently considered to be the best two-equation model for transitional flows (Savill 1995b). The Launder & Sharma model uses the following modifications to the standard $k - \epsilon$ model:

$$f_\mu = \exp\left(\frac{-3.4}{(1 + Re_t/50)^2} \right)$$
$$f_{\epsilon 1} = 1.0, \quad f_{\epsilon 2} = 1 - 0.3 \exp(-Re_t^2)$$
$$D = -2\nu \left(\frac{\partial \sqrt{k}}{\partial y} \right)^2, \quad E = 2\nu\nu_t \left(\frac{\partial^2 U}{\partial y^2} \right)^2$$
$$\text{where} \quad Re_t = \frac{k^2}{\nu \tilde{\epsilon}}$$

Note that the turbulent Reynolds number normally is defined as $Re_t = k^2/(\nu\epsilon)$, but in the Launder & Sharma model the use of $\tilde{\epsilon}$ also results in the slightly modified definition, namely $Re_t = k^2/(\nu\tilde{\epsilon})$. The model by Launder & Sharma is a modified version of the model by Jones & Launder (1972). This model was originally developed for prediction of relaminarization in flows with strong favourable pressure gradients. The low-Reynolds number function $f_{\epsilon 2}$ was chosen to fit experimental data for the decay of isotropic grid turbulence both at high

and low Reynolds numbers. The second low-Reynolds number function, f_μ, was determined from Couette flow experiments, in which the measured mean-velocity gradient was used to calculate an eddy viscosity based on a mixing length according to van Driest ($\nu_T = l_m^2|\partial U/\partial y|$, with $l_m = \kappa y\,(1 - e^{-\sqrt{\tau/\rho}yA/\nu})$, in which τ is the total shear stress and κ and A are constants). Further, the dissipation equation was adjusted to get a reasonable level of kinetic energy in the viscous sublayer. With these values of ϵ and ν_T the shape of the low-Reynolds number function was determined as $f_\mu = \nu_T\epsilon/(k^2 c_\mu)$, to which a suitable analytical function was fitted. Moreover, an additional source term (E) was introduced in the dissipation equation in order to increase ϵ at $y^+ \approx 20$. A similar term, which also contains the second derivative of U, can be traced in eq. 3.7. However, as the authors point out, there is no physical argument for the term, and it is only adopted due to empirical reasons.

3.2.2 Differential Reynolds Stress Models

A slightly more complex approach than two-equation models is the use of Differential Reynolds Stress Models (DSM-models). The main advantage is that the Reynolds stress tensor (τ_{ij}) does not need to be modelled directly, and that it also provides a natural way to treat anisotropies between the different components. However, in DSM-models a transport equation is solved for each independent component in τ_{ij}, which leads to a higher computational cost. It also implies new question marks concerning the modelling of some terms in the transport equations. In the present study two different DSM-models have been tested, which both include low-Reynolds-number modifications and make use of linear pressure strain terms.

The HJH-model

The DSM-model by Hanjalić, Jakirlić and Hadžić (1995, see also Jakirlić *et al.* 1994) in the following denoted as the HJH-model, is developed for fully turbulent wall-bounded flows. Thus, no tuning in order to improve transition prediction has been done. The model includes wall-reflection terms as proposed by Gibson & Launder (1978), transport terms modelled by simple gradient diffusion (Daly & Harlow 1970), and an invariant form of the so-called Yap-correction (S_l-term below). The Yap-correction increases the dissipation to suppress excessive growth of the turbulent length scale, which can occur for example close to solid walls in adverse pressure gradient flows. The additional term $S_{\epsilon 4}$ was originally proposed by Hanjalić & Launder (1980), and aims to increase the effect of normal stresses on the production of ϵ. This term has an effect primarily in flows with streamwise pressure gradients. Further, the physically different effects of wall-proximity and viscosity have been modelled separately, using low-Reynolds number functions depending on either the turbulent Reynolds number or the invariants of the stress anisotropy and dissipation anisotropy tensors.

The model is summarized as follows, where the notations of the modelled terms refer to equation 3.5:

$$\phi_{ij} = \phi_{ij,1} + \phi_{ij,2} + \phi^w_{ij,1} + \phi^w_{ij,2}$$

$$\phi_{ij,1} = -C_1\epsilon a_{ij}, \quad \phi_{ij,2} = -C_2\Big(\mathcal{P}_{ij} - \frac{2}{3}\mathcal{P}\delta_{ij}\Big)$$

$$\phi^w_{ij,1} = C_1^w f_w \frac{\epsilon}{k}\Big(\overline{u_k u_m} n_k n_m \delta_{ij} - \frac{3}{2}\overline{u_i u_k} n_k n_j - \frac{3}{2}\overline{u_k u_j} n_k n_i\Big)$$

$$\phi^w_{ij.2} = C^w_2 f_w\Big(\phi_{km.2}n_k n_m\delta_{ij} - \frac{3}{2}\phi_{ik.2}n_k n_j - \frac{3}{2}\phi_{kj.2}n_k n_i\Big)$$
$$f = \min\left\{\left(\frac{Re_t}{150}\right)^{3/2}; 1\right\}, \quad F = \min\{0.6; A_2\}, \quad C = 2.5AF^{1/4}f$$
$$C_1 = C + \sqrt{A}E^2, \quad C_2 = 0.8\sqrt{A}, \quad C^w_1 = \max\{1 - 0.7C; 0.3\}, \quad C^w_2 = \min\{A; 0.3\}$$
$$f_w = \min\left\{\frac{k^{3/2}}{2.5\epsilon x_n}; 1.4\right\}$$

$$\epsilon_{ij} = f_s\epsilon^*_{ij} + (1 - f_s)\frac{2}{3}\delta_{ij}\epsilon$$
$$\epsilon^*_{ij} = \frac{\epsilon}{k}\frac{[\overline{u_iu_j} + (\overline{u_iu_k}n_jn_k + \overline{u_ju_k}n_in_k + \overline{u_ku_l}n_kn_ln_in_j)f_d]}{1 + \frac{3}{2}\frac{\overline{u_pu_q}}{k}n_pn_qf_d}$$
$$f_s = 1 - \sqrt{A}E^2, \quad f_d = (1 + 0.1Re_t)^{-1}$$

$$d_{ij} = \frac{\partial}{\partial x_k}\left[\left(\nu + C_s\frac{k}{\epsilon}\overline{u_ku_l}\right)\frac{\partial\overline{u_iu_j}}{\partial x_l}\right], \quad \text{with } C_s = 0.22$$

In the above formulation n_i denotes a unit vector normal to the solid surface and x_n is the wall-normal distance. The invariants of the stress anisotropy and the dissipation anisotropy tensors are defined as:

$$a_{ij} = \frac{\overline{u_iu_j}}{k} - \frac{2}{3}\delta_{ij}, \quad A_2 = a_{ij}a_{ji}, \quad A_3 = a_{ij}a_{jk}a_{ki}, \quad A = 1 - \frac{9}{8}(A_2 - A_3)$$
$$e_{ij} = \frac{\epsilon_{ij}}{\epsilon} - \frac{2}{3}\delta_{ij}, \quad E_2 = e_{ij}e_{ji}, \quad E_3 = e_{ij}e_{jk}e_{ki}, \quad E = 1 - \frac{9}{8}(E_2 - E_3)$$

The modelled version of the dissipation equation takes the following form:

$$\frac{\partial\epsilon}{\partial t} + U_k\frac{\partial\epsilon}{\partial x_k} = -C_{\epsilon1}f_{\epsilon1}\frac{\epsilon}{k}\overline{u_iu_j}\frac{\partial U_i}{\partial x_j} - C_{\epsilon2}f_{\epsilon2}\frac{\epsilon\tilde{\epsilon}}{k} + C_{\epsilon3}f_\mu\nu\frac{k}{\epsilon}\overline{u_ju_k}\frac{\partial^2U_i}{\partial x_j\partial x_l}\frac{\partial^2U_i}{\partial x_k\partial x_l}$$
$$+\frac{\partial}{\partial x_k}\left[\left(\nu + C_\epsilon\frac{k}{\epsilon}\overline{u_ku_l}\right)\frac{\partial\epsilon}{\partial x_l}\right] + S_{\epsilon4} + S_l \tag{3.12}$$

where

$$S_{\epsilon4} = C_{\epsilon4}k\frac{\partial U_i}{\partial x_j}\frac{\partial U_l}{\partial x_m}\epsilon_{ijk}\epsilon_{lmk} \tag{3.13}$$
$$S_l = \max\left\{\left[\left(\frac{1}{C_l}\frac{\partial l_t}{\partial x_n}\right)^2 - 1\right]\left(\frac{1}{C_l}\frac{\partial l_t}{\partial x_n}\right)^2; 0\right\}\frac{\epsilon\tilde{\epsilon}}{k}A$$
$$l_t = \frac{k^{3/2}}{\epsilon}, \quad f_{\epsilon1} = 1, \quad f_{\epsilon2} = 1 - \frac{C_{\epsilon2} - 1.4}{C_{\epsilon2}}\exp\left[-\left(\frac{Re_t}{6}\right)^2\right], \quad f_\mu = 1$$
$$C_\epsilon = 0.18, \quad C_{\epsilon1} = 1.44, \quad C_{\epsilon2} = 1.92, \quad C_{\epsilon3} = 0.25, \quad C_{\epsilon4} = 1.16, \quad C_l = 2.5$$

The term $S_{\epsilon4}$ requires a comment. For 2D boundary layer flows, as considered in the present study, the term is replaced by (see Hanjalić & Launder 1980)

$$C_{\epsilon 4}(\overline{vv} - \overline{uu})\frac{\partial U}{\partial x}\left(\frac{\epsilon}{k}\right) \tag{3.14}$$

which means that the production of ϵ due to normal stresses is augmented. However, it is not straightforward how this term is derived from the general formulation of $S_{\epsilon 4}$ (3.13). The derivation is as follows: If 3.13 is evaluated for 2D boundary layer flows it takes the form

$$C'_{\epsilon 4}k\left(\frac{\partial U}{\partial y} - \frac{\partial V}{\partial x}\right)^2 \approx C'_{\epsilon 4}k\left(\frac{\partial U}{\partial y}\right)^2$$

i.e. it is expressed in terms of the rotational part of the mean strain field. This can be rewritten in terms of $\overline{uv}$ if the eddy-viscosity concept (with $c_\mu f_\mu = 1$) is applied in combination with the $k - \epsilon$ approach for the velocity and the length scale:

$$\left(\frac{k^2}{\epsilon}\frac{\partial U}{\partial y}\right)\frac{\partial U}{\partial y}\frac{\epsilon}{k} = -\overline{uv}\frac{\partial U}{\partial y}\frac{\epsilon}{k}$$

This term is identical to the production of ϵ due to *shear* stresses, which appears as part of the first term on the right hand side of equation 3.12:

$$C_{\epsilon 1}\frac{\epsilon}{k}\left(-\overline{uv}\frac{\partial U}{\partial y} - \overline{uv}\frac{\partial V}{\partial x} + (\overline{vv} - \overline{uu})\frac{\partial U}{\partial x}\right) \tag{3.15}$$

Thus, in order to emphasize the production of ϵ due to *normal* stresses, 3.13 must be added to equation 3.12 with a negative coefficient. However, instead of reducing the production due to shear stresses it is suggested to increase the contribution from normal stresses by adding 3.14 with a positive coefficient $C_{\epsilon 4} = 1.16$. If the boundary layer approximation is applied to the equations, the production term (3.15) takes the form $-C_{\epsilon 1}(\epsilon/k)\overline{uv}(\partial U/\partial y)$. In this case, in order to keep the production of ϵ due to normal stresses constant, the coefficient $C_{\epsilon 4}$ takes the value 2.6 ($C_{\epsilon 1} + C_{\epsilon 4}$).

Also the term S_l in the dissipation equation requires a comment. Convergence problems due to initial transients appeared when this term was included in the calculations, but this problem was avoided if the term was initially switched off. After the initial transients in the solution have settled down, the term is smoothly increased by a weight function and attains its intended value a short distance downstream of the starting position. This damping has to be applied to all calculations, both for fully turbulent and transitional flows.

Finally, it should also be mentioned that equation 3.12 solves the "true" dissipation (not $\tilde{\epsilon}$), while $\tilde{\epsilon}$ only is included in the $C_{\epsilon 2}$-term to assure that the term goes to zero close to the wall.

The SLY-model

The SLY-model is a DSM-model developed by Savill, and is based on a model by Kebede, Launder & Younis (1985). The model has been tuned in order to work well for transitional flows, and the results presented by Savill show good agreement with experiments and simulations in a number of test cases at different FST-levels and pressure gradients. The model which is described below is sometimes denoted as "basic SLY" by the originator, as later versions of the model have been extended with terms intended to model pressure diffusion and non-local effects in the pressure strain (Savill 1995a). Some terms are similar to the previously described HJH-model, and only the differences are given below:

$$C_1 = 1.8, \quad C_2 = 0.6, \quad C_1^w = 0.5, \quad C_2^w = 0.3$$

$$f^* = \frac{k^{3/2}}{\epsilon x_n}; \qquad f^*_{max} = \max_{x_n} f^*; \qquad f_w = \begin{cases} 1 & : 0 < x_n < (x_n)_{max} \\ f^*/f^*_{max} & : x_n > (x_n)_{max} \end{cases}$$

$$\epsilon_{ij} = f_s \epsilon^*_{ij} + (1 - f_s)\frac{2}{3}\delta_{ij}\epsilon$$

$$\epsilon^*_{ij} = \frac{\epsilon}{k} \frac{[\overline{u_i u_j} + \overline{u_i u_k} n_j n_k + \overline{u_j u_k} n_i n_k + \delta_{ij}\overline{u_k u_l} n_k n_l]}{1 + \frac{5}{2}\frac{\overline{u_p u_q}}{k} n_p n_q}$$

$$f_s = (1 + 0.1 Re_t)^{-1}$$

$$f_{\epsilon 1} = \max\left\{ \frac{1}{c_{\epsilon 1}} \left(2.0 - \frac{0.725 R_y}{65} \right); 1 \right\} \quad \text{where} \quad R_y = \frac{\sqrt{k}\, x_n}{\nu}$$

$$f_{\epsilon 2} = 1 - \frac{0.4}{c_{\epsilon 2}} \exp\left[- \min\left\{ \left(\frac{Re_t}{6} \right)^2 ; 20 \right\} \right]$$

$$f_\mu = \exp\left(\frac{-3.4}{(1 + Re_t/50)^2} \right), \quad S_{\epsilon 4} = S_l = 0$$

$$C_\epsilon = 0.15, \quad C_{\epsilon 1} = 1.275, \quad C_{\epsilon 2} = 1.8, \quad C_{\epsilon 3} = 0.25$$

The function f_μ is taken from the $k - \epsilon$ model by Launder & Sharma, in which it is used to reduce ν_t close to the wall. The SLY-model also makes use of a Reynolds number (R_y) which depends on the distance from the wall, and another important difference as compared to the HJH-model is the coefficients C_1, C_2, C_{1w} and C_{2w}. In the SLY-model these are all constants, while in the HJH-model they are dependent on the turbulence characteristics. Furthermore, the viscous destruction term in the dissipation equation takes the form $-C_{\epsilon 2} f_{\epsilon 2} \epsilon^2/k$, i.e. no $\tilde{\epsilon}$ is used. The boundary condition (BC) for ϵ is not the usual Dirichlet BC, but instead Savill uses $\partial\epsilon/\partial y = 0$ at the wall. However, still the $C_{\epsilon 2}$-term grows towards infinity close to the wall, but this deficiency has been corrected in more recent versions of the model by an additional pressure diffusion term (private communication).

3.3 Boundary layer simplifications

In the present study the calculations are restricted to 2D boundary layers, i.e. the spanwise mean velocity (W) as well as all spanwise gradients are assumed to be zero. For boundary layer flow it is common to simplify the equations by using the boundary-layer approximations. This means that all terms including streamwise derivatives are neglected (except for the streamwise convection), and the pressure is assumed to be constant across the boundary-layer thickness. The approximations can be summarized as:

$$\frac{\partial}{\partial y} \gg \frac{\partial}{\partial x}, \quad \frac{\partial p}{\partial y} = 0, \quad \frac{\partial p}{\partial x} = -\rho U_0 \frac{dU_0}{dx}$$

where U_0 is the free stream velocity. The approximations are usually fairly good at high Reynolds numbers and weak pressure gradients. The main advantage of the boundary layer simplifications is that these equations are parabolic, in contrast to the Reynolds-averaged Navier-Stokes equations which are elliptic and thus require much more computer time to be

solved. In the sequel of this report three different levels of approximations have been used, which are summarized as follows:
(i) The boundary layer simplifications are applied to all equations, which are solved with a parabolic code.
(ii) The complete formulation of the production and pressure strain terms are used, including terms dependent on streamwise derivatives of the mean velocity field, and the additional normal stress $-\partial\overline{uu}/\partial x$ is added to the momentum equation. The equations are solved with a parabolic code.
(iii) The Reynolds-averaged Navier-Stokes equations as given in eq. (3.3), thus including streamwise diffusion and allowance for pressure variations across the boundary layer, are solved with a 2D elliptic code.

The different formulations will be referred to as formulation (i), (ii) and (iii) respectively.

Chapter 4

Numerical methods

4.1 Boundary-layer code

The equations formulated with approximations (i) and (ii) respectively are solved with a parabolic boundary layer code, which implies that only one sweep in the streamwise direction is necessary. The code makes use of a rectangular grid with non-equidistant mesh size both in the streamwise (x) and wall-normal (y) direction. Moreover, a staggered grid is used in the y-direction (see figure 4.1a). The staggered grid points (e.g. $y_{j-1/2}$) are positioned precisely in the centre between the neighbouring non-staggered ones (y_{j-1} and y_j). The quantities k, ϵ and U are evaluated at the staggered grid points, while the V-velocity and the Reynolds stresses are evaluated at the non-staggered ones. The spatial distribution of the grid points can be varied by using different stretching functions (e.g. quadratic, exponential or logarithmic) in the streamwise and the normal directions.

The discretization is based on the finite volume method, which has become widely used due to its good conservation properties. The equations are discretized in integral form, and for each unknown grid point a control volume is defined. The change in time of the considered quantity within the volume is expressed as the sum of the incoming and outgoing fluxes through the boundaries plus additional source terms. Normally the unknown is positioned in the centre of the control volume, however, since the equations are parabolic, and are thus most naturally solved by a marching procedure, the unknown quantity is positioned at the downstream boundary of the control volume (se figure 4.1a). The code makes use of a second-order upwind scheme in the x-direction, while the wall-normal discretization is a so-called hybrid scheme. This means that it can either be a central scheme or a first-order upwind scheme depending on the relative ratio between the convection term and the diffusion term. If the local-grid Reynolds number ($R_{cell} = V\,\Delta y/(\nu + \nu_T)$, in which Δy is the size of the grid cell and ν_T is the contribution from turbulent transport) is larger than 2, the discretization will switch to the upwind scheme. Since the large truncation error in the first-order upwind scheme acts as an artificial viscosity, the diffusion term is neglected in this case. However, when the central scheme is used, both convection and diffusion terms are discretized with second-order accuracy. The previously described discretizations apply to all transport equations that are used in the present calculations, which, in the case of RST-closures, imply equations for U, $\overline{uu}$, $\overline{vv}$, $\overline{uv}$, k, ϵ and the continuity equation.

The convection and diffusion terms are treated implicitly, which results in a tri-diagonal equation system at each streamwise step, with the unknowns positioned at grid-points representing a line normal to the streamwise direction in the computational domain. Since the

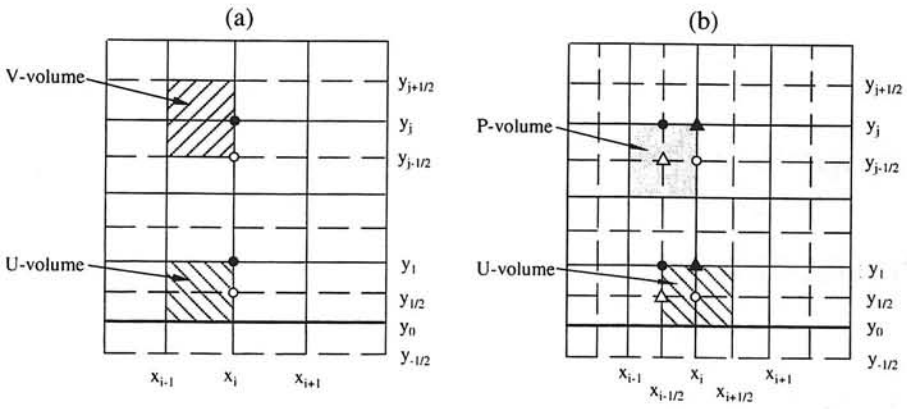

Figure 4.1: Finite volume grid in (a) Boundary layer code and (b) elliptic code. The symbols denote grid points where the different quantities are evaluated: (a) V, $\overline{uu}$, $\overline{vv}$, $\overline{ww}$ and $\overline{uv}$ (•); U. k and ϵ (○); (b) $\overline{uv}$(▲), U (○); P, k, ϵ, $\overline{uu}$, $\overline{vv}$ and $\overline{ww}$ (△); V (•).

equations include non-linear terms, an iterative solution procedure is necessary. The streamwise and wall-normal convection velocities are thus taken from the previous iteration level, and the additional terms that appear in the transport equations are treated as source terms evaluated from the previous iteration as well. In this way the equations become decoupled and can be solved one after another using a line Gauss-Seidel method. Each tri-diagonal equation system is solved with the Thomas algorithm, and the considered quantity is updated directly after the equation is solved. A convergence criterion, defined as the maximum allowed change between two iterations for any quantity or grid point, is used before the next streamwise position is considered.

Stability

The linear equation system that appears at each iteration step is well-conditioned if the coefficient matrix is diagonal dominant. Usually this is also a requirement in order to obtain converging solutions with an iterative method. In the present calculations the convergence were improved by using two different types of relaxation.

(1) A relaxation factor (α) was used to obtain sufficient under-relaxation. The diagonal in the coefficient matrix is then multiplied with $1/\alpha$, and a corresponding contribution $(1/\alpha - 1)$ times the solution from the previous iteration was added to the right hand side (RHS). A typical value for α was 0.7, but in some cases an even smaller relaxation factor was used.

(2) An additional adjustment of the magnitude of the diagonal was obtained through the source terms. Negative source terms in the RHS were divided with the solution from the previous iteration and added to the diagonal of the coefficient matrix. In this manner the magnitude of the diagonal elements could be increased in comparison with the off-diagonal elements.

Inclusion of streamwise derivatives

As mentioned in chapter 3.3 different levels of approximations were used in the calculations. Terms including streamwise derivatives were incorporated in the parabolic code, resulting in

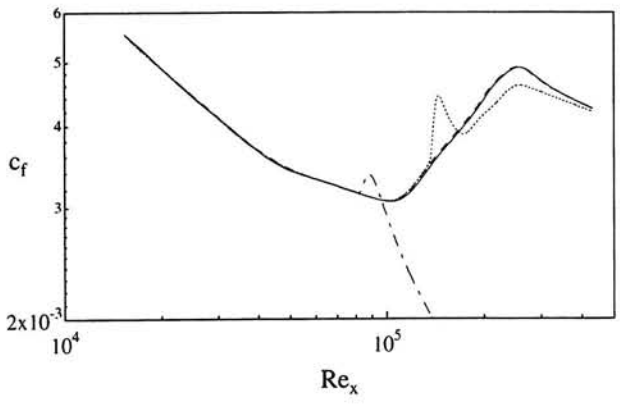

Figure 4.2: Wall-shear stress coefficient calculated with different streamwise grid spacing: 200×100 grid points (—), 400×100 (- - -), 1000×100 ($\cdots$) and 2000×100 ($- \cdot -$). Streamwise diffusion terms are included in the transport equations and solved with a parabolic code.

the approximation (ii) as described in section 3.3. In some calculations also the streamwise diffusion term were included. Since the inclusion of this term makes the equations elliptic, one should expect problems when trying to use a parabolic solver. Figure 4.2 shows the behaviour of the wall-shear stress in the transition region when the grid was systematically refined in the streamwise direction. Obviously numerical instabilities appear when the grid spacing becomes small, which is an effect that can be ascribed to the inconsistent solution procedure for the elliptic equations.

4.1.1 Boundary conditions

The boundary conditions at the inflow boundary (i.e. west side) are specified by the initial conditions, and these are further described in section 5.3. The free stream boundary conditions for all equations except the U-equation are specified as homogeneous Neumann boundary conditions, i.e.

$$\frac{\partial \phi}{\partial y} = 0 \text{ when } y \to \infty$$

in which ϕ denotes any of the considered quantities. The boundary condition for U is a Dirichlet boundary condition, which is given by the free stream velocity ($U_0(x)$) in the test case specifications. The boundary conditions at the wall are specified as homogeneous Dirichlet conditions, i.e.

$$U = V = \overline{uu} = \overline{vv} = k = \overline{uv} = 0$$

However, the wall boundary condition for the ϵ-equation differs between the models. The HJH-model uses

$$\epsilon|_{y=0} = 2\nu \left(\frac{\partial \sqrt{k}}{\partial y} \right)^2_{y=0}$$

which can be derived from Taylor expansions of u_i close to the wall. In calculations with the model by Launder & Sharma an equation for $\tilde{\epsilon}$ is solved (see section 3.2.1 for definition), which implies that $\tilde{\epsilon} = 0$ at the wall. Finally, in the model by Savill (SLY-model), a homogeneous Neumann condition is used as wall boundary condition for ϵ.

A note on the wall-boundary conditions

As mentioned earlier the discretization based on the finite volume method considers the net-change of the incoming and outcoming fluxes through each control volume. For instance the diffusion part of the wall normal flux of ϕ through the control volume corresponding to node $(x_i, y_{j-1/2})$ can be written as

$$\begin{aligned}\frac{\partial}{\partial y}\left((\nu+\nu_T)\frac{\partial\phi}{\partial y}\right)\Big|_{y_{j-1/2}} dx\,dy &\approx \frac{((\nu+\nu_T)\frac{\partial\phi}{\partial y})|_{y_j} - ((\nu+\nu_T)\frac{\partial\phi}{\partial y})|_{y_{j-1}}}{y_j - y_{j-1}}(x_i - x_{i-1})(y_j - y_{j-1}) \\ &\approx \left(\frac{(\nu+\nu_T|_{y_j})(\phi_{j+1/2}-\phi_{j-1/2})}{y_{j+1/2}-y_{j-1/2}} - \frac{(\nu+\nu_T|_{y_{j-1}})(\phi_{j-1/2}-\phi_{j-3/2})}{y_{j-1/2}-y_{j-3/2}}\right)(x_i - x_{i-1}) \qquad (4.1)\end{aligned}$$

ϕ corresponds to a quantity which is evaluated at the staggered grid points, i.e. k, ϵ or U. The flux leaving this volume $((\nu+\nu_T)(\partial\phi/\partial y)|_{y_j})$ will also be used as the flux entering the neighbouring volume, and so on. To discretize the equations at the boundaries virtual grid points are introduced (see figure 4.1a). The virtual points at the wall are defined as $y_{-1/2} = -y_{1/2}$, and they are used in the equations for k, ϵ and U. One advantage with the use of virtual grid points is that the discretization scheme used for internal volumes can also be used for the volumes at the boundary. To obtain $\phi = \phi_{wall}$ at the wall the simplest choice for the value at the virtual grid point is a linear extrapolation, i.e. $0.5(\phi_{i,j-1/2}+\phi_{i,j+1/2}) = \phi_{wall}$. However, this boundary condition turns out to give errors in the near-wall behaviour of ϵ. The explanation can be traced to the incorrect representation of the second-derivative of ϕ at the first real grid point $(x_i, y_{1/2})$. Since the viscous diffusion term in the k-equation is balanced by the dissipation near the wall, the dissipation will exhibit a kink at the first real grid point (see figure 4.3). A consistent discretization will be obtained if $\phi_{i,-1/2}$ is determined as

$$\phi_{i,-1/2} = \frac{2h(3h-m)}{m(m+h)}\phi_{i,3/2} + \frac{m-6h}{m}\phi_{i,1/2} + \frac{8h}{m+h}\phi_{wall} \qquad (4.2)$$

in which $h = y_{1/2} = -y_{-1/2}$, $m = y_{3/2} - y_{1/2}$ and ϕ_{wall} is the specified Dirichlet boundary condition at the wall. It should be noted that the discretization 4.1 can be used without modifications also at the wall if the values at the virtual grid points are specified as in 4.2.

4.2 Elliptic solver

When the streamwise diffusion and the allowance of pressure variations are included in the equations they become elliptic and have to be solved with an elliptic solver. The present code solves the Reynolds-Averaged Navier-Stokes equations (RANS) using a time-marching technique to the steady state. The discretization and the solution method is in many respects similar to the boundary layer code, but with some important extensions.

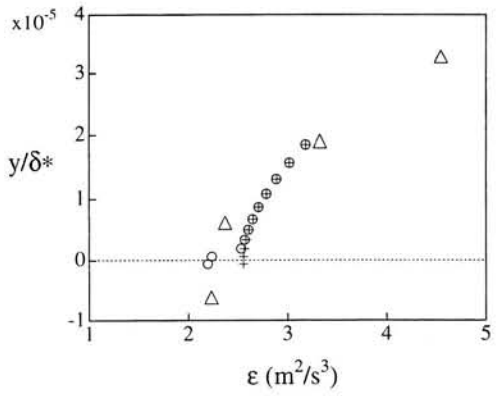

Figure 4.3: Near wall behaviour of the dissipation for different boundary conditions. Boundary condition from linear extrapolation and coarse grid (△), fine grid (○); boundary condition as specified in (4.2) (+).

The grid is a non-equidistant rectangular grid which is staggered both in the x- and y-direction (see figure 4.1b), and the equations are discretized according to the finite volume method. If a control volume is specified between the non-staggered grid lines, the scalars (P, k and ϵ) and the normal stresses ($\overline{uu}$, $\overline{vv}$ and $\overline{ww}$) are evaluated in the centre of the volume. The shear stress is found in the north-east corner, and the U and V velocities are evaluated in the centre of the east and north side of the volume respectively. The present distribution of the variables on a staggered grid has advantages when discretizing the pressure. For instance $(\partial P/\partial x)_{i,j-1/2}$ can be discretized with central differences using adjacent points (i.e. $(P_{i+1/2,j-1/2} - P_{i-1/2,j-1/2})/(x_{i+1/2} - x_{i-1/2})$), leading to second order accuracy at the grid point where $U_{i,j-1/2}$ is evaluated.

Similar to the boundary layer code a line Gauss-Seidel method is used, but in the present case sweeps are made alternatingly in both spatial directions. Grid points on vertical lines are updated during sweeps from west to east and vice versa, followed by sweeps between south and north boundaries in which the unknown variables are positioned on horizontal lines. The unsteady term in each equation is discretized with two time levels, i.e. the truncation error is of first order with respect to Δt. The spatial discretization of the equations makes use of a hybrid scheme in both directions, similar to the one described in section 4.1. In a sweep from the west to the east boundary the unknowns are positioned on a vertical line ($x = x_i$), while the information at line x_{i+1} is taken from the previous iteration level. Since all non-linear terms are evaluated at the previous level, a tri-diagonal equation system is formed at each line. The equations are solved sequentially, which implies that an equation is solved in the entire domain by making one sweep before the next equation is considered.

In addition to the equations that were solved in the boundary layer code, also an equation for the pressure is necessary. In the incompressible Navier-Stokes equations the pressure acts as a constraint on the velocity field in order to fulfil the continuity equation. The pressure is solved with a two-step pressure correction method (SIMPLE), which is briefly explained in the following. The equations for U and V are solved with the pressure terms evaluated at the previous iteration level. Note that a separate transport equation for V is solved in this

elliptic code, in contrast to the boundary layer code which uses the continuity equation to calculate V. Also the non-linear terms are evaluated at the previous iteration level in order to linearize the equations. The obtained solutions are denoted as U^* and V^*, but they do not satisfy the continuity equation at the new iteration level $(n+1)$. To get the correct solution at the new iteration level a correction is necessary ($U^{n+1} = U^* + U^c$ and similar for V). If the equations for U^* and V^* are subtracted from the corresponding equations for U^{n+1} and V^{n+1}, and neglecting all terms which include velocities evaluated at other grid points than the considered one, the following equations for the corrected velocities are obtained:

$$
\begin{aligned}
U^{n+1}_{i,j-1/2} &= U^*_{i,j-1/2} + a_{i,j-1/2}(\delta p_{i-1/2,j-1/2} - \delta p_{i+1/2,j-1/2}) \\
V^{n+1}_{i-1/2,j} &= V^*_{i-1/2,j} + b_{i-1/2,j}(\delta p_{i-1/2,j-1/2} - \delta p_{i-1/2,j+1/2})
\end{aligned}
\tag{4.3}
$$

$\delta p_{i,j-1/2}$ is the difference in pressure between the iteration levels n and $n+1$ at point $(x_i, y_{j-1/2})$, and $a_{i,j-1/2}$ and $b_{i-1/2,j}$ are grid dependent coefficients. If the previous expressions are substituted into the continuity equation, a Poisson equation for δp is obtained with the right hand side dependent on U^* and V^*. Once this equation for the pressure correction is solved, U^{n+1} and V^{n+1} can be determined from 4.3.

Time steps and relaxation

In the present calculations the number of sweeps at each time level was maximized to ten. The marching in time was continued until the maximum change of any variable between two iterations were of the order of the machine accuracy. In the code no explicit relaxation is used to improve the stability of the calculations, but the stability and the convergence can be affected by the size of the time step. It should be noted that we are only interested in the final steady solution. Therefore there is no need to make a very accurate time integration, or to obtain full convergence at each time level.

4.2.1 Boundary conditions

The boundary conditions in the elliptic code are specified in the same manner as described in section 4.1.1, but with a few extensions due to the elliptic solution procedure. At the downstream boundary homogeneous Neumann boundary conditions are used for all quantities, i.e. $(\partial\phi/\partial x) = 0$ at $x = x_{max}$. Mathematically, there is no need to specify separate boundary conditions for the pressure in order to obtain a well-posed problem. However, since the equations are solved sequentially in the present code, boundary conditions are specified also for the pressure correction equation. These are homogeneous Neumann conditions at all boundaries, together with a predefined value of the pressure in the node positioned at (x_{max}, y_{max}).

Chapter 5

Test case specifications

The transitional test cases that are used for model validation in the present study are mainly taken from the wide range of test cases specified within the ERCOFTAC Transition Special Interest Group, coordinated by Dr. A.M. Savill. An overview of the test cases is given by Savill (1995b). However, the number of test cases considered in the present study is quite small compared with what is available. One aim is to study in detail how the models perform in a few simple test cases, instead of making qualitative comparisons of the behaviour in many different cases. Some features of the considered test cases are summarized in table 5.1.

Case	Tu (%)	U_0 (m/s)	$\partial p/\partial x$	Experiment/LES
T3A–	1	19.6	0	Rolls-Royce (RR)
T3A	3	5.2	0	RR
T3B	6	9.6	0	RR
T3C1	≈ 7	6.3–9.3	< 0 & > 0	RR, trans. in accelerating flow
T3B-LES	5.5	9.6	0	LES by Yang & Voke (1993)
KTH-B	1.35	11.9	0	Royal Inst. of Technology
KTH-E	6.6	8.0	0	Royal Inst. of Technology
Wieghardt & Tillmann	–	33.0	0	Fully turbulent boundary layer
Samuel & Joubert	–	26–17	> 0	Fully turbulent boundary layer
Spalart DNS	–	–	0	DNS of turbulent boundary layer ($Re_\theta \in [225, 1410]$)

Table 5.1: Test cases

The experimental data obtained by Rolls-Royce were taken in a boundary-layer wind tunnel with a working section of 2 m length and cross-section 0.71×0.26 m^2. The experiments were carried out on a flat plate equipped with a sharp leading edge, and the plate had a small negative angle of attack to avoid leading edge separation. The turbulence was generated by grids positioned at the beginning of the test section, 610 mm upstream of the leading edge, which resulted in almost perfectly isotropic turbulence. The pressure gradient used in case T3C1 was obtained by a profiled wind-tunnel wall opposite to the working side of the plate. The normal and shear stresses were measured with hot-wire anemometry, using single and cross-wire probes, and the wall-shear stress was determined by different methods (Preston tube measurements, Clauser's method based on the law of the wall, momentum balance technique). More details can be found in Roach & Brierley (1992). In general, the

experimental observations described in chapter 2 are also valid for the experiments by Rolls-Royce. For instance the damping of the v-fluctuations observed outside the boundary layer can also be seen in the T3A and T3B test cases.

A similar transition experiment has been carried out in the low-turbulence wind tunnel at the Royal Institute of Technology (KTH) in Stockholm (Matsubara, unpublished results). The tunnel has a 7 m long test section with a cross stream dimension of 1.2×0.8 m^2. The same experimental set-up was used by Westin *et al.* (1994), and consisted of a flat plate with a 2 m long working part, and a specially designed asymmetric leading edge. The FST was generated by grids positioned inside the test section, 1.5 m upstream of the leading edge. A small anisotropy between the streamwise and cross stream components was observed, and the ratio v_{rms}/u_{rms} was 0.9 and 0.85 in the KTH-B and KTH-E case respectively. The measurements through the transition region include only the streamwise velocity component, which makes the Rolls-Royce data more suitable for detailed comparisons of different components in the Reynolds stress tensor. However, the KTH-data provides the possibility to compare results from two independent experimental set-ups at similar FST-conditions. In figure 5.1 the downstream development of the shape factor H is shown for the zero pressure gradient cases by Rolls-Royce and KTH ($H = \delta^*/\theta$, where δ^* is the displacement thickness and θ the momentum loss thickness). Qualitatively the agreement between the two experiments is fairly good for the highest FST-level (6% and 6.6% respectively). For the lower turbulence level (1% and 1.35% respectively) the difference in the start of the transition region becomes larger. This is expected, as the relatively late transition in those cases allows influence from exponential instabilities, e.g. TS-waves, and it is well-known that small differences regarding the experimental set-ups can highly influence the generation and development of TS-waves.

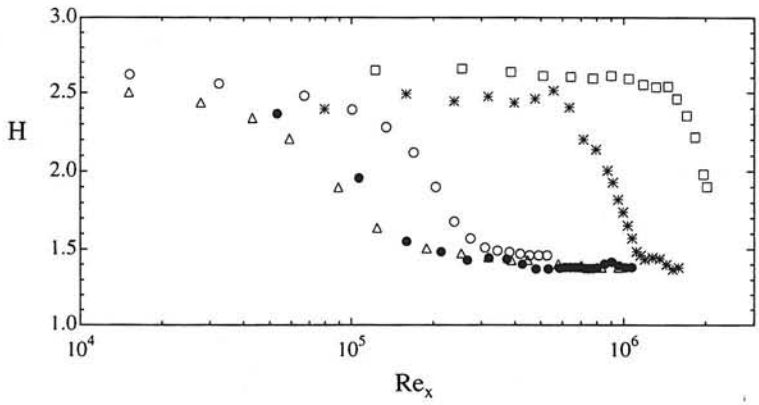

Figure 5.1: Downstream development of the shape factor (H) in different test cases: T3B ($\triangle$), T3A ($\circ$), T3A– ($\square$), KTH-E ($\bullet$) and KTH-B ($*$).

Besides the experimental test cases there is also a transitional test case based on Large Eddy Simulations by Yang & Voke (1993, see also Voke & Yang 1995). The LES were carried out with approximately the same parameters as for the experimental T3B case, in order to provide data for a detailed comparison. A general advantage with simulations is that some variables which are very difficult to measure, for instance the different components in the dissipation anisotropy tensor and the pressure correlations, can be extracted from simulated

data. However, one should bear in mind that also Large Eddy Simulations contain a modelling part for the smallest scales in the flow. In the LES by Yang & Voke a subgrid-scale model similar to that of Smagorinsky was used, but modified to allow for low-Reynolds-number effects which usually become important near solid walls. In order to check the influence of the subgrid-scale model Voke and Yang also carried out simulations with the model switched off (which gives a low-resolution "Direct" Numerical Simulation). This calculation showed that the influence of the model is in fact restricted to regions with turbulent flow (i.e. in the free stream and in the turbulent boundary layer), while the pre-transitional region as well as the predicted transition onset were only slightly affected.

Finally, there are also three test cases in table 5.1 which consider fully turbulent boundary layers. The test case based on experiments by Wieghardt & Tillman (1951) is a flat plate boundary layer at zero pressure gradient, while the experiment by Samuel & Joubert (1974) was carried out at a fairly strong adverse pressure gradient. The DNS by Spalart (1988) considers a fully turbulent boundary layer at relatively low Reynolds numbers (Re_θ up to 1410), and provides the possibility to study how the distribution among the different components in the Reynolds stress tensor is modelled. These test cases are considered in order to test that the models perform well in fully turbulent flows, which is an essential requirement that should be fulfilled also after any modification or tuning of the models for transition prediction is made.

5.1 Free stream boundary conditions

In the present calculations homogeneous Neumann boundary conditions have been specified at the free stream boundary for all variables except U, which is given by the specified free stream velocity (see section 4.1.1). Consequently, the decay rate of the free stream turbulence is given by the parameters in the turbulence model and the initial values of k and ϵ. The kinetic energy (k_0) at the starting position for the calculation (x_0) is given by the specified FST-level, but the initial dissipation (ϵ_0) must be chosen to attain the best fit to the experimental decay curve of the FST. However, for isotropic turbulence an analytic expression for the decay can easily be derived from the modelled k and ϵ equations (equation 3.10 and 3.11) if the free stream velocity (U_0) is constant and the streamwise diffusion is neglected. The expression reads:

$$\frac{u_{rms,0}}{U_0} = \frac{\sqrt{\frac{2}{3}}}{U_0}\left[\frac{(C_{\epsilon 2}-1)\epsilon_0}{k_0^{C_{\epsilon 2}} U_0}(x-x_0) + k_0^{1-C_{\epsilon 2}}\right]^{\frac{1}{2(1-C_{\epsilon 2})}} \tag{5.1}$$

in which the coefficient for the viscous destruction term ($C_{\epsilon 2}$) is usually taken as 1.92. It should be noted that in the present report $u_{rms,0}$ denotes the streamwise fluctuation level in the free stream, while Tu represents the corresponding value close to the leading edge (i.e. $Tu = (u_{rms,0}/U_0)_{x=0}$). In figure 5.2 the formula 5.1 is used to calculate the decay curve for the T3A case, and the results were confirmed by the corresponding $k-\epsilon$ calculations. With $k_0 = 0.042$ m^2/s^2 at $x_0 = 10$ mm ($Tu = 3.2\%$), a value of $\epsilon_0 = 1.8 \cdot 10^{-4}$ m^2/s^3 gives good agreement with experimental data. It is common to give the initial conditions in terms of k_0 and the turbulent length scale ($l_{t0} = k_0^{3/2}/\epsilon_0$), which gives a length scale of 9.8 mm in the present case. It should be mentioned that a value $l_{t0} = 30.1$ mm is given in the test case specifications for the T3A test case (Savill 1992). However, with the "standard" value of the model parameter (i.e. $c_{\epsilon 2} = 1.92$) this gives a too slow decay of the FST (figure 5.2).

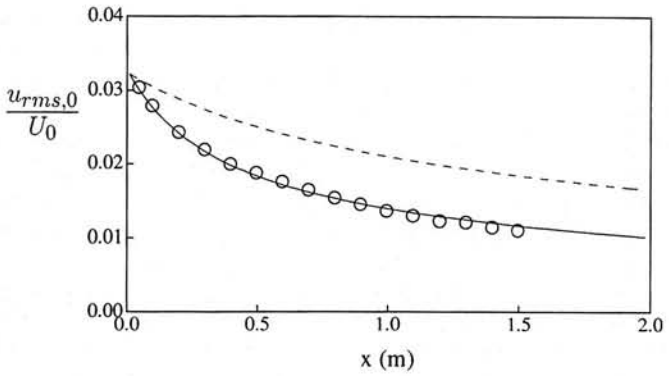

Figure 5.2: Downstream development of the FST-level (Tu) in the T3A case. Experimental results (o), Formula 5.1 with $l_{t0} = 9.8$ mm (—) and $l_{t0} = 30.1$ mm (- - -).

A remark on the specification of the free stream turbulence level

In most experiments the free stream turbulence level is given by Tu and a decay curve for $u_{rms,0}$ along the test section. However, if the turbulence is not isotropic, this does not provide sufficient boundary conditions for the calculations. As pointed out in chapter 2, the wall-normal component has proven to be more efficient in generating boundary layer perturbations than both the u- and the w-component. Consequently, a more relevant measure of the free stream turbulence level is $v_{rms,0}/U_0$, or, preferably, all three fluctuating components.

5.2 Some remarks on turbulent length scales

The turbulent length scale in the free stream can experimentally be determined from the turbulence decay rate, using the relation

$$L_\epsilon = -\frac{u_{rms}}{U_0} \frac{\overline{uu}}{\partial \overline{uu}/\partial x}$$

(cf. test case specifications in Savill 1992). L_ϵ denotes the experimentally determined length scale, which differs from the usual definition of the turbulent length scale (l_t) through a scaling constant. If the FST is assumed to be isotropic and the dissipation in the free stream is estimated from equations 3.10 and 3.11 (neglecting diffusion), the following relation can be derived:

$$l_t = \frac{k^{3/2}}{\epsilon} = \frac{\left(\frac{3}{2}\overline{uu}\right)^{3/2}}{-U_0 \frac{d}{dx}\left(\frac{3}{2}\overline{uu}\right)} = \sqrt{\frac{3}{2}} L_\epsilon$$

The turbulent length scale (l_t) is an integral length scale, representing a typical size of the larger eddies which contain the major part of the turbulent energy. Another, smaller scale, is the Taylor micro scale, which represents the smallest energetic eddies in the flow. For isotropic turbulence the streamwise micro-scale (λ_x) can be related to the dissipation through $\epsilon = 30\,\nu\,\overline{uu}/\lambda_x^2$ (cf. Hinze 1975), which leads to the following relation between λ_x and l_t:

$$\frac{\lambda_x}{l_t} = 20 Re_t^{-1/2}$$

in which $Re_t = k^2/(\nu\epsilon)$ is the turbulent Reynolds number. When the turbulent Reynolds number increases, the range of scales in the flow increases, which can be observed as a smaller ratio between λ_x and l_t as well as a turbulent spectra extending over a wider frequency range. The Taylor micro-scales are, however, not the smallest scales that can be found in the flow. Smaller scales exist (Kolmogorov scales), but their energy is rapidly transferred into heat through the viscous dissipation. However, as pointed out earlier, only one length scale (l_t) appears explicitly in one-point closures, although some influence from other scales can be modelled by empirical wall- and viscosity damping which are included in many low-Reynolds-number modifications.

5.3 Initial conditions

In the present study all calculations start at a small distance downstream of the leading edge, which means that initial profiles of all variables have to be specified at the inflow boundary. The exclusion of the leading edge region implies several simplifications. For instance the use of parabolic calculations become more justified, as the difficult flow around the stagnation point is avoided. Further, the available code only allows the use of rectangular grids, which are not applicable if other shapes than a sharp leading edge are to be considered. However, it is well-known from experiments that the shape of the leading edge is important for the receptivity and the generation of disturbances inside the boundary layer, wherefore separate studies of leading edge receptivity is of highest interest.

In most of the calculations, the initial conditions (IC) that have been used are rather artificial and not fitted to experimental profiles. The initial conditions specified below are referred to as "standard IC", which can be considered as a first choice if one has no specific knowledge about the initial profiles except for the free stream values k_0 and l_{t0}. The mean velocity profiles (U and V) are obtained from the Blasius solution, and the turbulent fluctuations are assumed to be isotropic and continuously damped towards the wall. Furthermore, a dissipation equal to the production predicted by the eddy-viscosity concept is assumed. This gives

$$\begin{aligned}
&\overline{uu} = \overline{vv} = \overline{ww} = \frac{2}{3}k \quad \text{where} \quad k = k_0 \left(\frac{U}{U_0}\right)^2 \\
&\overline{uv} = 0 \\
&\epsilon = \max\left\{\epsilon_0 \,;\, 0.3\, k \left|\frac{\partial U}{\partial y}\right|\right\} \quad \text{where} \quad \epsilon_0 = k_0^{3/2}/l_{t0}
\end{aligned}$$

Other initial profiles have been used in order to test the sensitivity to the initial conditions, but the different profiles are described in connection with the results in chapter 6.

It should be noted that the notation "initial conditions" above is only valid for the parabolic calculations. In the case of elliptic calculations the previously described profiles are used as inflow boundary conditions as well (with a minor difference in the BC for V, which is specified as a homogeneous Neumann condition). However, in addition, initial conditions have to be specified for the entire computational domain.

Chapter 6

Results

In this chapter the results obtained with the different models will be discussed. Unless otherwise stated the displayed solutions can be considered as almost grid independent. This was checked by increasing the number of grid points both in the streamwise and the normal direction until sufficiently small changes in the wall-shear stress coefficient or the shape factor were found. Further, the computational domain in the wall-normal direction (y_{max}) was chosen to be at least two times larger than the boundary layer thickness (δ_{99}) at the downstream boundary.

6.1 Launder & Sharma $k-\epsilon$ model

Since the ERCOFTAC Transition Special Interest Group was started in 1990, several independent studies have been carried out for different two-equation models. A general conclusion is that the best available model for transition is the $k-\epsilon$ model of Launder & Sharma, at least if models including empirical information in order to trigger the start of transition are excluded. The relative success with the Launder & Sharma model has been ascribed to the damping function (f_μ) for the turbulent viscosity, which shows a better agreement with LES-data than functions used in other $k-\epsilon$ models. The model gives reasonably good predictions for the start of transition in zero-pressure gradient flows within a fairly wide range of FST-levels, but there are problems to correctly reproduce the effects of pressure gradients. This is, however, a well known shortcoming also in fully turbulent flows for models which make use of only one length scale, and to improve the modelling of adverse pressure gradients it is common to use additional terms in the equation for ϵ.

Although the present study is focussed on Reynolds stress models, a few calculations have been carried out with the Launder & Sharma model in order to provide some data for later comparisons. Figure 6.1 shows predictions of the wall-shear stress coefficient (c_f) for zero-pressure gradient cases with Tu ranging from 1% to 6%. As mentioned above the start of transition is in reasonable agreement with experiments, although consistently somewhat too early, but the length of the transition region is severely underpredicted. This seems to be a general behaviour for eddy-viscosity models, unless they include some additional correction to prolong the transition region. It should be noted that figure 6.1 is plotted on a logarithmic scale, which slightly conceals the deviation. For instance in the T3A$^-$-case ($Tu = 1\%$) the start of transition is more than 20% further upstream than in the experiments.

Another important remark concerns the sensitivity to the specified initial profiles. In the

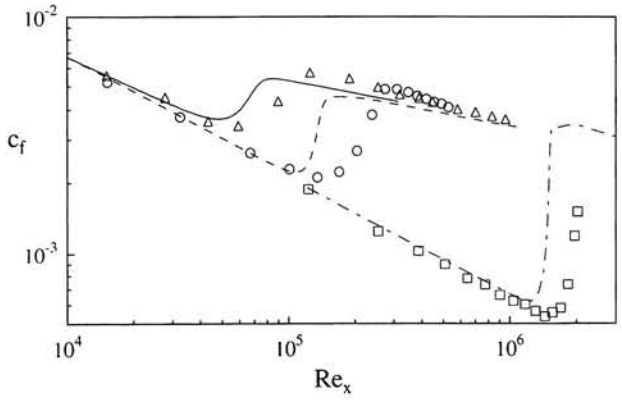

Figure 6.1: Wall-shear stress predicted with the Launder & Sharma model for different test cases. Symbols and lines show results from experiments and calculations respectively. T3B ($\triangle$,—), T3A ($\circ$,---), T3A$^-$ ($\square$,-·-).

calculations shown in figure 6.1 the "standard IC" are applied (see section 5.3). but in figure 6.2 calculations with different initial conditions are displayed. The "standard IC" is shown as solid lines, while the dashed k and ϵ profiles are taken from the simulations by Yang & Voke. However, these profiles are re-scaled to fit the present test case, i.e. the y-coordinate is scaled with the displacement thickness and the k-profile is scaled with the free stream value of k. The dissipation profile is obtained from the assumption that the variations of the turbulent length scale across the boundary layer can be scaled with the free stream length scale (l_{t0}), i.e. the re-scaled profile reads $l_t(y) = k^{3/2}/\tilde{\epsilon} = (l_{t0})_{T3A} \times (l_t(y)/l_{t0})_{LES}$ (note that $\tilde{\epsilon}$ is used instead of ϵ in the Launder & Sharma model). In all calculations the mean velocity profile was taken from the Blasius solution.

Although the initial profile of k taken from the LES shows a rather different shape than the "standard IC", with a peak inside the boundary layer and a reduced level in the region outside the boundary layer edge, the effect on the transition location is almost negligible (if all other profiles are unchanged). However, if also the re-scaled ϵ-profile is used, the transition is moved further upstream. The major difference is that the dissipation extracted from the simulation is much smaller than the production in the central part of the boundary layer, in contrast to the "standard IC" where a balance between the two terms is assumed. In the last calculation the dissipation profile is intentionally exaggerated (twice as large as the "standard IC" inside the boundary layer), which in turn results in a significant delay of the start of the transition region.

In a study by Dick & Vancoillie (1988) the $k-\epsilon$ equations were reformulated into a stability problem. Starting from the $k-\epsilon$ model of Launder & Sharma, the following simplifications were applied: the parallel flow assumption was used, the turbulence Reynolds number set to zero (i.e. the low-Reynolds number functions become constants), the turbulent viscosity was neglected in the diffusion terms, the additional near-wall terms (D and E) were neglected, and, finally, k and ϵ were assumed to behave as exponential perturbations. It should be noted that the exponential disturbances do not contain a frequency or wave length, only a spatial amplification factor, and the disturbances can be considered to consist of all frequencies and

wave lengthes.

Dick & Vancoillie (1988) showed that unstable solutions exist, and that their critical Reynolds-number is strongly dependent on the coefficient governing the destruction term in the dissipation equation ($c_{\epsilon 2} f_{\epsilon 2}$). The large sensitivity to this coefficient is illustrated in figure 6.2d, in which $c_{\epsilon 2}$ is changed from the specified value of 1.92 to 1.8. As mentioned in section 3.2.1 this coefficient is determined to fit experimental data of the turbulence intensity in decaying homogeneous turbulence. However, modification of the value of $c_{\epsilon 2}$ has a rather small influence on the decay curves for Tu, but it has a dramatic effect on the predicted start of the transition region.

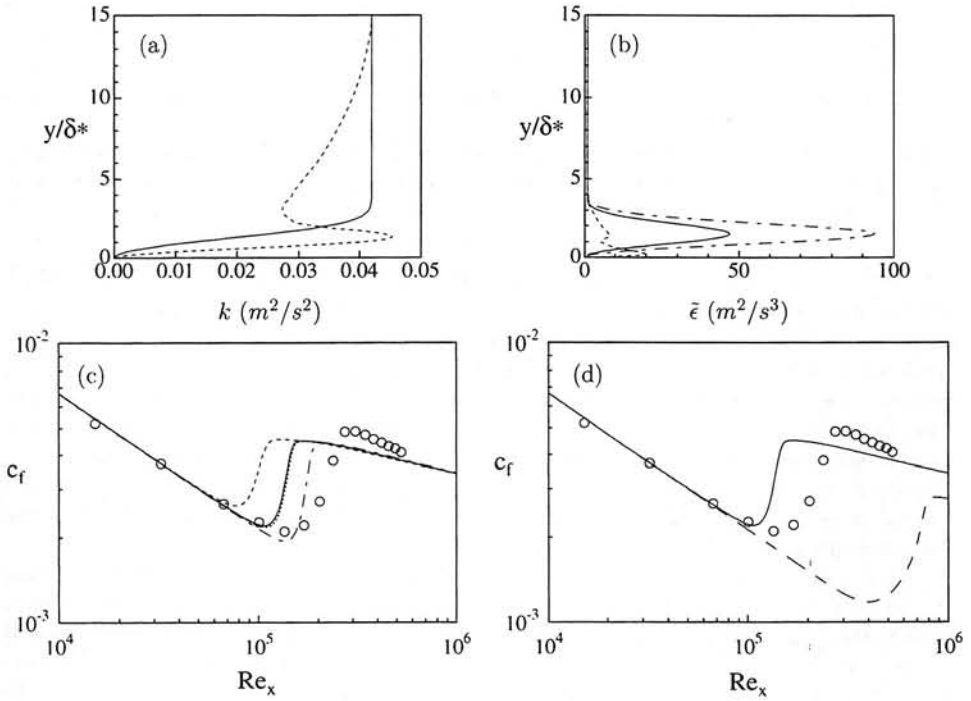

Figure 6.2: Initial profiles at $x = 10$ mm for (a) the kinetic energy and (b) the dissipation. Labels: "standard IC" (—), rescaled LES (- - -) and an additional (large) dissipation (– · –). (c) Calculated wall-shear stress coefficient with different initial profiles: "standard IC" (—), k-profile from the LES (otherwise as "standard IC") (· · ·), k and ϵ from the LES (- - -), k from the LES but ϵ from the additional ϵ-profile (– · –). (d) Wall-shear stress calculated with $c_{\epsilon 2} = 1.92$ (—) and $c_{\epsilon 2} = 1.8$ (– –) (using "standard IC" in both cases).

6.2 The HJH-model

6.2.1 Fully turbulent flows

To begin with, it is of interest to see how the model behaves in fully turbulent boundary layers. The boundary layer approximations are applied to the calculations in the present section, i.e. formulation (i) (section 3.3) is used. For the zero-pressure gradient case by Wieghardt & Tillmann, the model gives a friction coefficient (c_f) that is about 4% higher than the experimental results at $Re_x = 1.1 \times 10^7$ ($Re_\theta = 15700$), while the Launder & Sharma model shows an even smaller deviation. Figures 6.3a and 6.3b show the wall-shear stress and the maximum $\overline{uv}$-Reynolds stress inside the boundary layer for the test case by Samuel & Joubert. The boundary layer is subjected to a relatively strong adverse pressure gradient, which is intensified for $x > 2.5$ m. The HJH-model clearly gives an improved prediction compared with the Launder & Sharma model when the pressure gradient becomes stronger. This is most obvious in the plot of the Reynolds stresses, where the Launder & Sharma model shows a large overprediction. Although quantitative comparisons of $\overline{uv}$ might be dangerous as the experimental difficulties associated with these measurements are large, there is qualitatively a good agreement between the HJH-model and the experiments. The improvement in the prediction of $\overline{uv}$ can to a large extent be ascribed to the additional production term $S_{\epsilon 4}$, which enhances the effect of normal stresses. If this term is set to zero, also the HJH-model gives an overprediction of $\overline{uv}$.

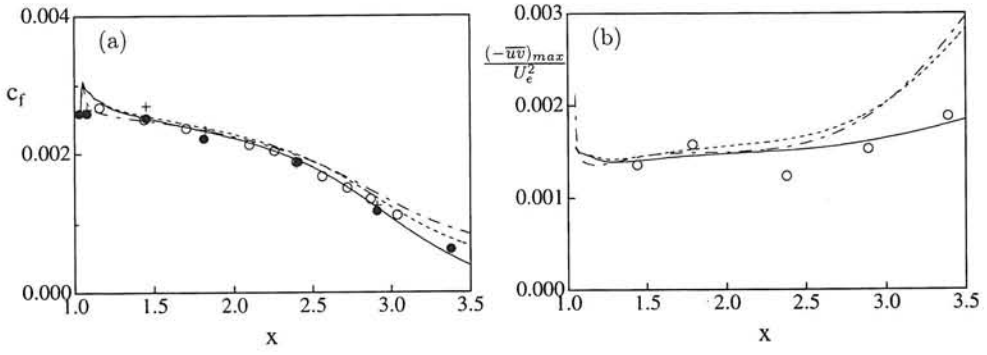

Figure 6.3: Adverse pressure gradient boundary layer measured by Samuel & Joubert. (a) Wall-shear stress coefficient $c_f = 2\nu(\partial U/\partial y)_w/(U_{ref})^2$ with $U_{ref} = 26.15$ m/s; (b) Maximum turbulent shear stress. (U_e equal to the local free stream velocity). Labels: experiments (o , •, +), HJH-model (—), HJH-model with $C_{\epsilon 4} = 0$ (- - -), Launder & Sharma $k - \epsilon$ (- · -).

The final test case with fully turbulent boundary layers is the Spalart DNS case. The calculations are started at a position corresponding to $Re_\theta = 300$, using initial profiles from the DNS. Figure 6.4 shows that the predicted wall shear stress is considerably underpredicted both in calculations with the Launder & Sharma model and the HJH-model. However, Spalart points out that there are some doubts about the accuracy of the c_f-value extracted from the DNS, since the DNS-data is about 5% higher than available experimental data.

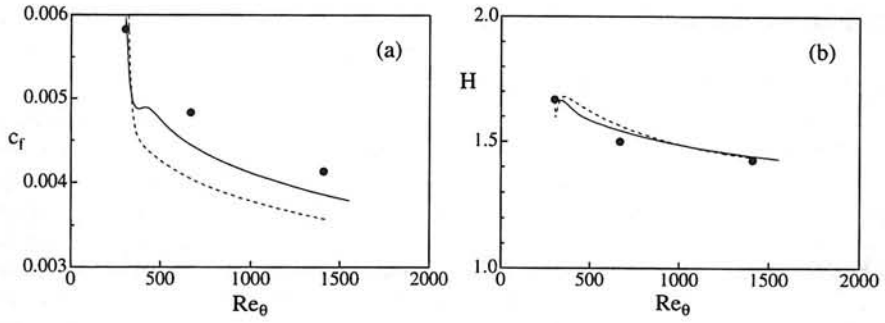

Figure 6.4: DNS of a fully turbulent boundary layer by Spalart (1988) (a) Wall-shear stress coefficient; (b) Shape factor. Labels: Spalart DNS (•), Launder & Sharma $k-\epsilon$ (---), HJH-model (—).

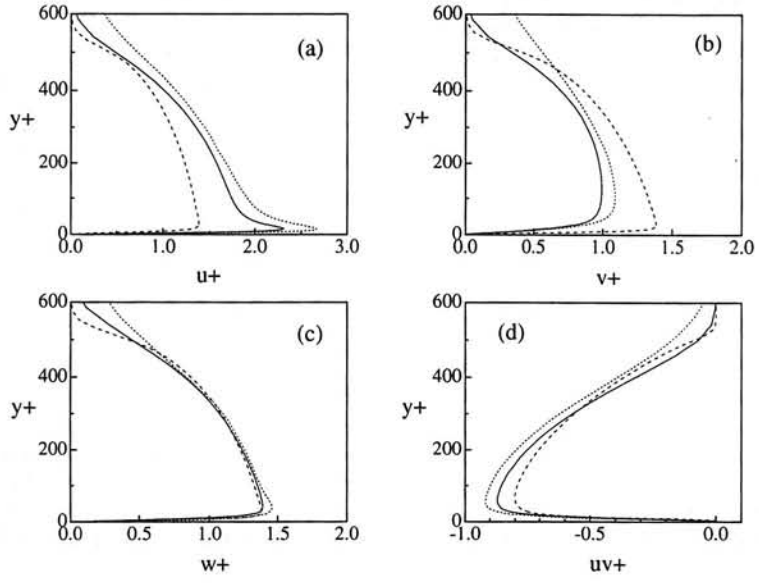

Figure 6.5: Profiles extracted at $Re_\theta = 1410$ (a) u^+, (b) v^+, (c) w^+, and (d) uv^+. Labels: Spalart DNS ($\cdots$), Launder & Sharma $k-\epsilon$ (---), HJH-model (—).

In figure 6.5 profiles of the different components in the Reynolds-stress tensor are plotted at $Re_\theta = 1410$. There is a consistent underprediction of all components in comparison to the DNS-data, although the shape of the profiles are well-predicted with the HJH-model.

6.2.2 Transitional flows

Turning the attention to the transitional test cases, figures 6.6a and 6.6b show the downstream development of the wall-shear stress and the shape factor for the test cases T3A ($Tu = 3\%$) and T3B ($Tu = 6\%$). In both calculations formulation (ii) (section 3.3) is used, and the "standard" initial conditions described in section 5.3 are applied. The free stream values of k_0 and l_{t0} at $x_0 = 10$ mm are chosen such that they give the best fit to the experimental decay of the FST, resulting in $k_0 = 0.042$ m^2/s^2, $l_{t0} = 9.8$ mm for the T3A case and $k_0 = 0.48$ m^2/s^2, $l_{t0} = 24$ mm for the T3B case. If only the location of the transition region is considered, the model gives a good prediction for the T3B-case. Also the rate with which c_f and H vary through the transition region is in fairly good agreement, and clearly much better than usually obtained with two-equation models. However, the behaviour in the pseudo-laminar region shows a significant deviation, since the calculated boundary layer profiles have a more turbulent-like shape than observed in the measurements.

When the turbulence level is reduced, the model predictions become successively worse. In the T3A-case, which is still a case with a relatively high FST-level (3%), the start of transition is at approximately 100% too large Re_x compared with the experiments, and the transition from a laminar to a turbulent boundary layer is extremely slow. It should also be mentioned that the calculations become sensitive to the grid resolution and the specified free stream boundary conditions. In the T3B-case 200×100 grid points are enough for almost grid independent solutions, while 2000×200 nodes are still not enough for the T3A-case. Tests with other l_{t0} in the T3A-case showed that the start of transition and the behaviour inside the transition region depend significantly on the choice of free stream boundary conditions.

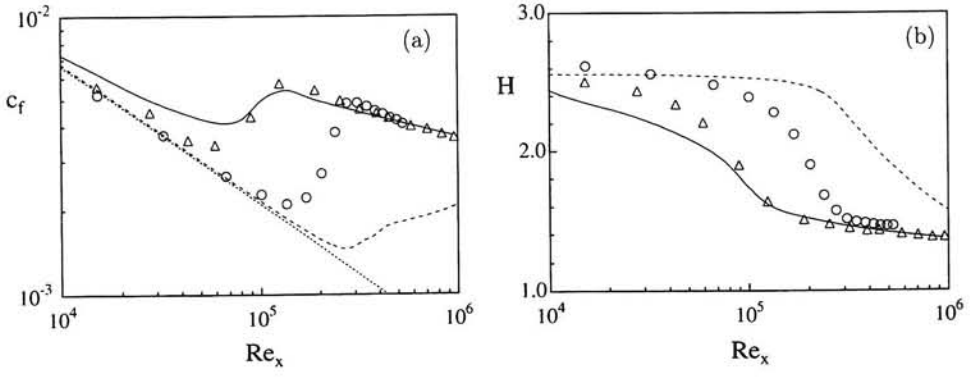

Figure 6.6: Transition prediction with the HJH-model for the T3A and T3B test cases. (a) Wall-shear stress coefficient; (b) Shape factor. Symbols and lines show results from experiments and calculations respectively: T3B (△, —); T3A (○, - - -).

Although the transition location is well predicted in the T3B-case, figure 6.6 gives only limited information about the behaviour inside the boundary layer. In figures 6.7a and b

the downstream development of the maximum Reynolds stresses are plotted for the two test cases (actually the square root of the normal stresses is plotted, i.e. $u_{rms} = \sqrt{\overline{uu}}$ etc.). The plots do not give any information about the y-location where the maxima appear, but they give a qualitative picture of whether the general behaviour is correct or not. In the beginning of the pseudo-laminar layer the maxima appear outside the boundary layer, especially for the $\overline{vv}$- and $\overline{ww}$-stresses. If no local maximum can be extracted within the boundary layer, the value plotted in figure 6.7 is taken at $y = 1.3\,\delta^*$, which is approximately in the middle of the boundary layer. This is the location where the experiments show a growing maximum. However, if the growing maximum predicted by the model appears at an erroneous position inside the boundary layer, this will result in a kink in the curve when the maximum exceeds the FST-level. This can clearly be observed in figure 6.7b.

In figure 6.7a the $\overline{uu}$-Reynolds stress grows inside the pseudo-laminar layer at a rate in good agreement with experiments, although the maximum value is slightly too low for all Re_x. Also from plots of individual $\overline{uu}$-profiles (not shown) the position where the maximum appears is in good agreement throughout the transition process. The corresponding plot for the T3A case shows that the model completely fails to predict the growth of the u-fluctuations in the pseudo-laminar layer, while a growth can only be observed just prior to transition. The relatively good agreement obtained in the T3B-case is encouraging, since it indicates that the model gives a good prediction of the transition location when the initial growth of $\overline{uu}$ is captured. However, the $\overline{vv}$- and $\overline{ww}$-stresses are not so well-predicted in the pseudo-laminar layer, where the computed profiles differ in both amplitude and shape compared with the measured ones. In the fully turbulent region the results are qualitatively good, although the relative magnitude of the different components is not in perfect agreement with the experiments, showing a too large redistribution from the streamwise to the transversal components. Finally, the shear stress ($\overline{uv}$) is overpredicted in the turbulent region. This is, however, partly due to an error in the measurements, which has been addressed by Rolls-Royce. In the experiment an incorrect hot-wire probe was used, and some later measurements resulted in approximately 30% higher values of $\overline{uv}$ than shown in figure 6.7. More details about the model behaviour will be given in sections 6.2.4 - 6.2.8.

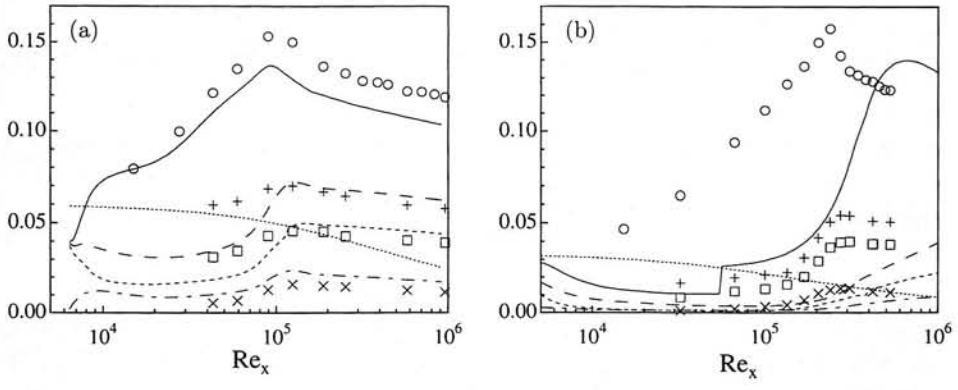

Figure 6.7: Downstream development of the maximum level of u_{rms}/U_0 ($\circ$, —), v_{rms}/U_0 ($\square$, - - -), w_{rms}/U_0 (+ , – –) and $-10\,\overline{uv}/U_0^2$ ($\times$, – · –) inside the boundary layer. Dotted line represent the FST-level ($u_{rms,0}/U_0$). (a) T3B-case, (b) T3A-case

Artifacts observed in the free stream

The additional wall-reflection terms in the pressure strain turn out to give an unexpected influence on the free stream turbulence. The wall-function (f_w), which is supposed to give a non-zero contribution only close to the wall, does not go to zero in the free stream if the FST-level is large enough. Although f_w is inversely proportional to the wall-distance, the high level of k in the free stream and the relatively small dissipation results in a non-zero value. Consequently, the wall-terms are active also in the free stream, resulting in a small redistribution from $\overline{vv}$ to the horizontal components. This artifact becomes more obvious in cases with large Tu. For instance in the T3B-case the anisotropy of $\overline{vv}$ (a_{22}) is approximately -0.11 at $x = 1.5$ m.

A second artifact with the present model is associated with the S_l-term, which is supposed to increase the dissipation if the turbulent length scale shows an excessive rise. The term contributes primarily in non-equilibrium flows (i.e. when the production and the dissipation have rather different magnitudes). This is the case in for instance impinging flows and pressure gradient flows, but the term should vanish in equilibrium regions and far away from walls. However, this term appears to be non-zero also in the region just outside the boundary layer edge (figure 6.8c) at the upstream positions. The non-zero value of this term can be ascribed to the variations of the kinetic energy close to the boundary layer edge (figure 6.8a), which is caused by the damping of $\overline{vv}$ outside the boundary layer. The variation of k influences the derivative of the turbulent length scale (figure 6.8b), and thus also the S_l-term. Note that $S_l = 0$ if $\partial l_t/\partial y < 2.5$ due to a delimiter. This implies that S_l is non-zero only for $y < \delta^*$ in the fully turbulent boundary layer at $x = 495$ mm.

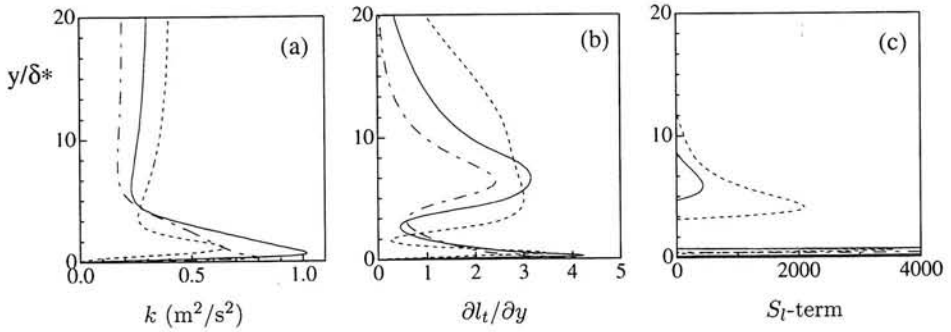

Figure 6.8: Profiles calculated with the HJH-model for the T3B-case. (a) Kinetic energy (k), (b) $\partial l_t/\partial y$, (c) S_l-term ("Yap-correction"). Labels: x=70 mm (R=4.4 × 10^4) (---), x=195 mm (R=1.2 × 10^5) (—) and x=495 mm (R=3.1 × 10^5) (-·-).

6.2.3 Elliptic/Parabolic calculations and influence of formulation

The influence of different terms was tested for the T3B-case. The different formulations were described in section 3.3, but are briefly recapitulated in the following. Formulation (i) makes use of the boundary layer approximation, i.e. the pressure is assumed to be constant across the boundary layer, and the terms including streamwise derivatives are neglected (except the streamwise convection). In formulation (ii) the complete formulations of the production and pressure strain terms are used, and the term $-\partial\overline{uu}/\partial x$ is added to the momentum

equation. Finally, formulation (iii) solves the complete Reynolds-averaged Navier-Stokes equations using the elliptic solver.

In the present calculations a slightly different choice of l_{t0} is used as compared with the calculations in section 6.2.2 (l_{t0} = 42 mm and 24 mm respectively). A thorough comparison of figures 6.6a and 6.9 will therefore reveal a minor difference in the curves obtained with formulation (ii). However, from the results shown in figure 6.9 one can conclude that the streamwise derivatives of the mean velocity field have a non-negligible effect on the position of the transition region. Starting from the boundary layer approximation (formulation (i)), an upstream movement of the predicted transition region can be observed when the additional x-dependent terms are included in the production. A further upstream movement is observed if also the complete formulation of the pressure-strain terms is used.

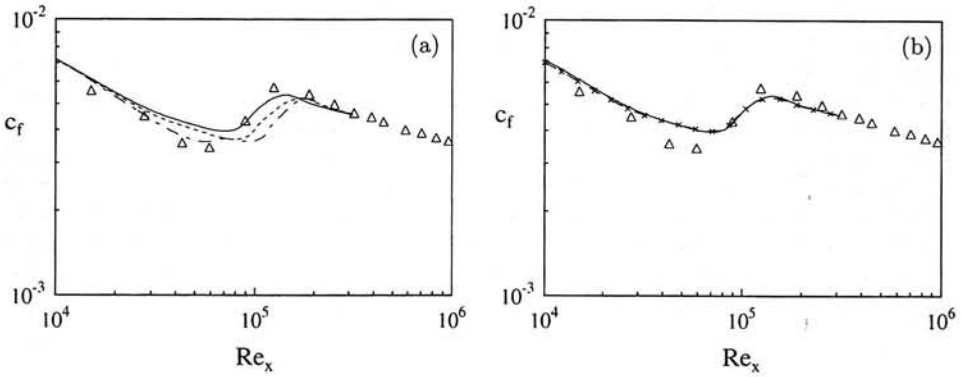

Figure 6.9: Comparison of calculations with different formulations (T3B-case): (a) Formulation (i) (- · -), formulation (i) but complete formulation of production terms (- - -), formulation (ii) (—); (b) formulation (ii) (—), formulation (iii) (elliptic) (- × -)

When the study is extended to elliptic calculations, almost identical results are obtained with formulation (iii) as with formulation (ii) (see figure 6.9b). Apparently the allowance of pressure variations inside the boundary layer and the additional streamwise diffusion has a negligible effect on the present calculations. The small difference between the elliptic and parabolic calculations may not be a general result, but might be due to the exclusion of the leading edge region. In calculations with the Launder & Sharma model carried out at UMIST, in which the elliptic calculations were started upstream of the leading edge, transition occurred further upstream than in the corresponding parabolic calculations. It was suggested that this effect could be ascribed to pressure variations inside the boundary layer. In the present elliptic calculations the wall-pressure increases in the transition region with approximately 0.5–1% of the dynamic pressure in the free stream (figure 6.10a). For comparison with the corresponding calculations by the group at UMIST, also the parameter $\theta^2/(\mu U_0)(\partial p/\partial x)|_w$ is shown in figure 6.10b. The results are qualitatively in agreement with the UMIST-results (cf. Savill 1995c), although the present curve shows a slightly stronger gradient in the transition region. It should be mentioned that the significant decay in wall pressure at the downstream boundary is an influence from the boundary condition, since the flowfield is forced to fulfil homogeneous Neumann conditions at $x = x_{max}$. However, by extending the computational domain in the streamwise direction, it was shown that the

upstream influence of the downstream boundary condition did not affect the transition region.

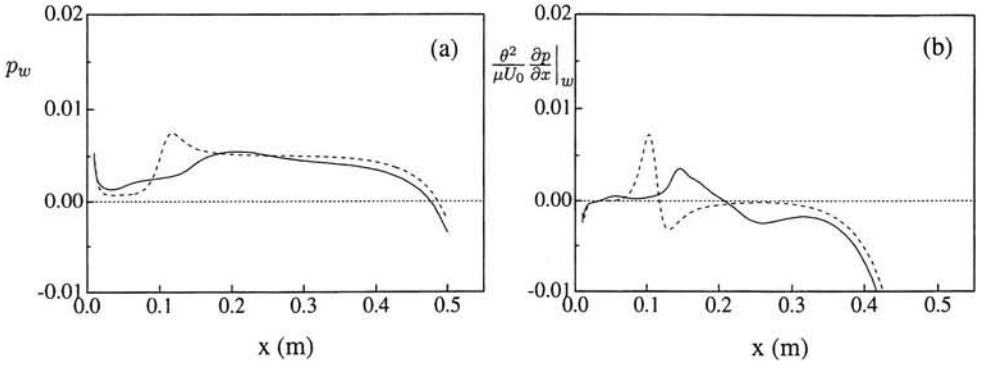

Figure 6.10: Calculated wall-pressure (a) and pressure gradient parameter (b) for test case T3B. Labels: HJH-model (—), Launder & Sharma $k-\epsilon$-model (- - -).

A similar comparison between the boundary layer approximation and the elliptic calculations (formulation (i) and (iii) respectively) was also undertaken for the Launder & Sharma model. In contrast to the results obtained with the HJH-model, the additional production associated with streamwise mean-velocity gradients did not give any observable change in the solution. Thus, in this zero-pressure gradient test case, the boundary layer approximation gave almost identical results as the elliptic calculations.

6.2.4 Influence of initial conditions

In calculations starting downstream of the leading edge some additional arbitrariness is caused by the necessity to specify initial profiles for the different variables. So far all calculations have been carried out with the "standard IC" described in section 5.3, which obviously is rather different from the experimental observations described in chapter 2. In the present section different initial profiles are tested in order to study the influence on the calculated solutions. In figure 6.11 some of the initial profiles are displayed, and the calculated results are shown in figure 6.12. The "standard IC" assumes isotropic normal stresses which are continuously damped towards the wall, there is no contribution from shear stresses, and furthermore the dissipation is assumed to be balanced by the production (based on the eddy-viscosity concept). This choice of initial conditions gives a smooth increase of the different Reynolds stresses without large initial transients (see also figure 6.7a).

The initial conditions that are denoted as rescaled LES-profiles are taken from a simulation by Yang & Voke. This scaling was carried out in the same manner as is described in section 6.1. The rescaling results in an overestimated peak level of $\overline{uu}$ inside the boundary layer, but despite this it gives a damping of the v-fluctuations outside the boundary layer which is closer to experimental observations. Further, the rescaled dissipation profile shows a peak closer to the wall, while in the middle of the boundary layer the dissipation is much smaller than the production. As can be observed from figure 6.12 these initial conditions give an initial transient in u_{rms}, but after a short distance the solution approaches the one obtained with the "standard IC", and the predicted transition region is almost unaffected. It should

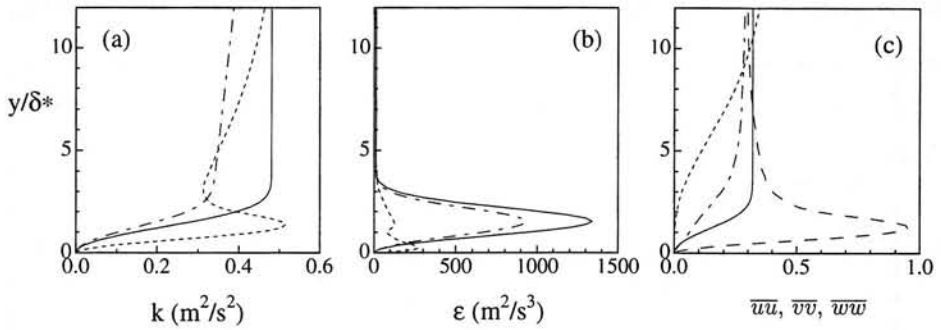

Figure 6.11: Initial profiles at $x = 10$ mm. (a) Kinetic energy with "standard IC" (—), rescaled LES-profiles (- - -), "standard IC" but $\overline{vv}$ damped for $y < 10$ mm (- · -).(b) Dissipation. Labels as in fig a. (c) Normal stresses with "standard IC" (—). Normal stresses with the rescaled LES: $\overline{uu}$ (– –), $\overline{vv}$ (- - -) and $\overline{ww}$ (- · -).

be noted that the choice of initial ϵ-profile is very important for the initial development. If the same rescaled profiles are used for the normal stresses, but with ϵ assumed to be balanced by the production, the growth curve of u_{rms} makes a rapid initial decay before it starts to grow at a lower amplitude than obtained with the "standard IC" (not shown). However, also in this case the effect on the transition region is small.

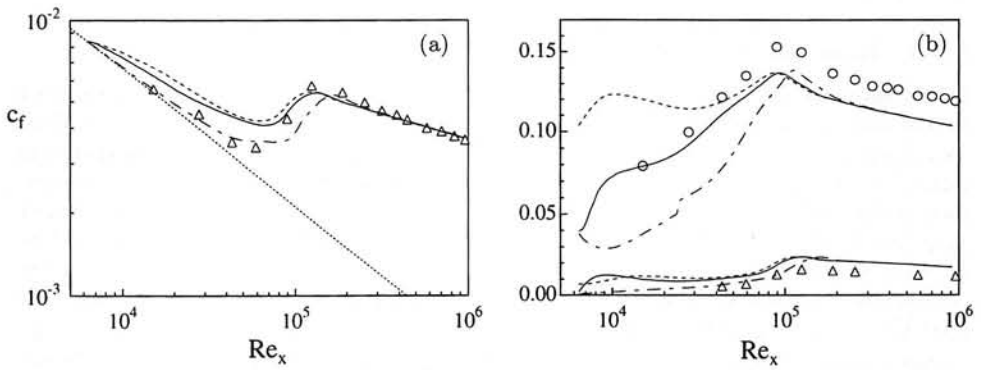

Figure 6.12: (a) Wall-shear stress calculated with different initial conditions for the T3B-case. (b) Downstream development of u_{rms}/U_0 and $-10\,\overline{uv}/U_0^2$. "Standard IC" (—), rescaled LES-profiles (- - -), "standard IC" but $\overline{vv}$ damped for $y < 10$ mm (- · -).

The last curve in figure 6.12 is calculated with the "standard IC", but with the only difference that the $\overline{vv}$-stresses are continuously damped towards the wall starting from a position 10 mm above the surface ($y/\delta^* \approx 45$ in figure 6.11). The reduced level of $\overline{vv}$ close to the boundary layer edge results in a delayed transition, and an improved prediction of the wall-shear stress can be observed in the pseudo-laminar region. Also the shape factor (not shown) and individual mean profiles are in good agreement with experimental data in

the region upstream of transition. However, the reduced v-fluctuations also result in a less satisfactory increase of the $\overline{uu}$-stresses (figure 6.12). As the dominating terms in the $\overline{uu}$-equation are the production and dissipation terms, a major cause for the underestimated growth of $\overline{uu}$ should be found in these two terms. This will be further discussed in section 6.2.8. It should be noted that the wall-normal distances for which $\overline{vv}$ are initially damped (about 5 mm in the rescaled LES-profiles and 10 mm in the last set of initial conditions) are both smaller than the region which was affected in the experiments.

Figure 6.13 shows calculations of the T3A-case with different initial profiles for the dissipation. The profiles for the normal stresses are the same in all three calculations and are specified as in the "standard IC". The ϵ-profiles are: 1) as specified in the "standard IC", 2) a profile with exaggerated dissipation (the dissipation inside the boundary layer is twice as large as the production) and 3) a constant value of ϵ across the boundary layer (same dissipation as in the free stream). Obviously the large differences in the initial dissipation profiles do not change the predicted onset of transition, which is too late as compared to the experiments.

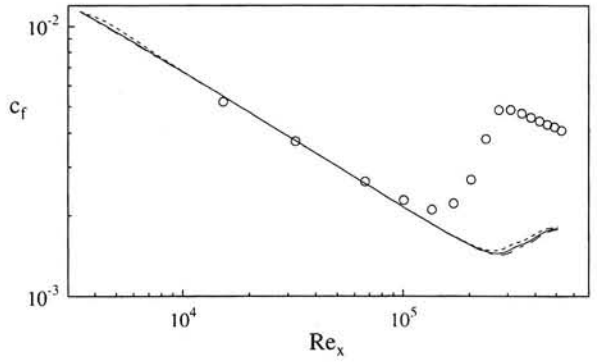

Figure 6.13: Wall-shear stress calculated with different initial ϵ-profiles for the T3A-case (HJH-model). "Standard IC" (ϵ=max$\{\epsilon_0; 0.3\,k\,|\partial U/\partial y|\}$) (—), ϵ=max$\{\epsilon_0; 0.6\,k\,|\partial U/\partial y|\}$ (- · -), ϵ=constant=ϵ_0 (- - -), experiments T3A (o). ϵ_0 is defined as $k_0^{3/2}/l_{t0}$ with l_{t0}=9.8 mm.

Profiles in the pseudo-laminar layer

In the previous section calculations of the T3B-case with a reduced level of $\overline{vv}$ close to the boundary layer edge resulted in an underestimated growth of $\overline{uu}$ in the pseudo-laminar region, while the prediction of the shape factor and the wall shear stress was in good agreement with experiments. In figure 6.14 different profiles are compared at $x = 95$ mm ($Re_x = 5.9 \times 10^4$), which is a position at the end of the pseudo-laminar region, just prior to the rapid increase in the wall-shear stress. It can be observed that the mean profile obtained with the "standard IC" has a more turbulent-like shape than the measured profile, while the calculation with a reduced level of $\overline{vv}$ gives better agreement with experiments. The differences between the profiles become more evident when the deviations from an unperturbed laminar profile are plotted in figure 6.14b.

In the Reynolds-Averaged Navier-Stokes equation for the streamwise velocity the main

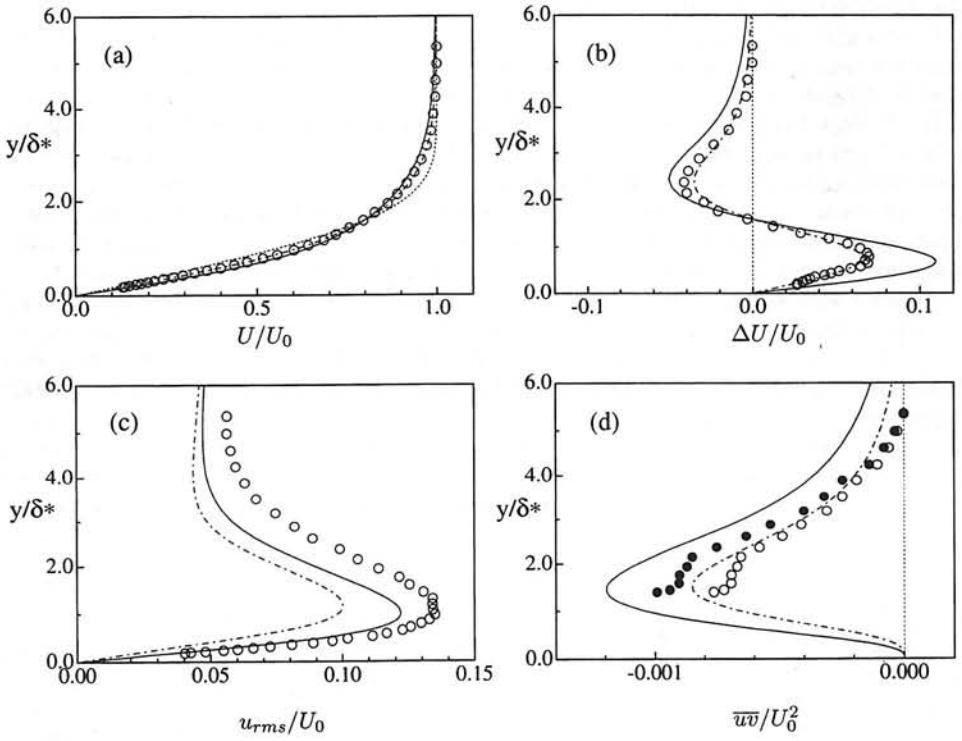

Figure 6.14: Profiles extracted at $x = 95$ mm ($Re_x = 5.9 \times 10^4$) for the T3B-case. (a) Mean velocity profiles; (b) mean velocity deviation from an unperturbed laminar profile; (c) u_{rms}/U_0; (d) $\overline{uv}/U_0^2$. Labels: Experiment (∘), $\overline{uv}$-stresses increased with 30% (•), calculations with "standard IC" (—), "standard IC" but $\overline{vv}$ damped for $y < 10$ mm (– · –) and unperturbed boundary layer (· · ·).

contribution to the distortion of the mean profile is the term $-\partial(\overline{uv})/\partial y$. If the calculated $\overline{uv}$-profiles are compared with experimental data (figure 6.14d), the peak value obtained with the last set of initial conditions (reduced $\overline{vv}$) is about 20% larger than the experiments, while the comparison with the "standard IC" gives a value which is about 70% larger. As mentioned earlier, the $\overline{uv}$-profiles measured by Rolls-Royce should be increased with about 30%. The experimental profile that is obtained after this correction is also shown in figure 6.14d.

One advantage with Reynolds Stress Models is that no modelling of the production term is needed, which means that the production of $\overline{uu}$ is directly dependent on the modelling of $\overline{uv}$. However, in figure 6.14c it can be observed that both calculated u_{rms}-profiles underpredict the fluctuation level, for example the case in which the initial conditions are a damped $\overline{vv}$-profile gives approximately 25% too low u_{rms}. It seems that a correct level of $\overline{uv}$, corroborated by the good agreement in the mean profiles, results in an underprediction of $\overline{uu}$ with the present model.

6.2.5 Comparison with an empirical correlation

In engineering design calculations the start of transition as well as the transition length are usually determined based on empirical correlations. One frequently used correlation is the one by Abu-Ghannam & Shaw (1980), which relates the start and end of transition to the local Reynolds number based on the momentum loss thickness. Analytical expressions for the Reynolds numbers ($Re_{\theta S}$ and $Re_{\theta E}$) are given as functions of the free stream turbulence level and a pressure gradient parameter. The characteristic length scale of the turbulence does not appear explicitly in the correlation, although a small effect of the decay rate of the free stream turbulence is taken into account through the definition of the free stream turbulence level. This is taken as the FST-level midway between the leading edge and the considered x-position (here denoted as $(u_{rms,0}/U_0)_{x/2}$).

In figure 6.15 the Abu-Ghannam & Shaw correlation for a zero-pressure gradient boundary layer is plotted together with experimental results as well as the present calculations. In the calculations the free stream velocity and the turbulent length scale at the starting position were fixed to 5 m/s and 30 mm respectively, while the initial kinetic energy was systematically changed. The start and end of the transition region were in most cases determined from the local maximum and minimum in the wall shear stress curve. However, for the highest levels of FST the transition onset could not be determined unambiguously, and in some cases the start of the transition region is omitted in figure 6.15.

It can be observed that the start of transition extracted from the experiments agrees fairly well with the empirical correlation. Also the Launder & Sharma model shows a good prediction of the start of the transition region for a wide range of turbulence levels, but, as was mentioned before, the extent of the transition region is much underpredicted. However, when considering the predictions by the HJH-model neither the start nor the end of the transition region is well predicted. There is a consistent trend that the transition region in terms of the local parameter θ is shifted from being too early at high FST-levels, to a delayed transition onset and a prolonged transition region for lower Tu.

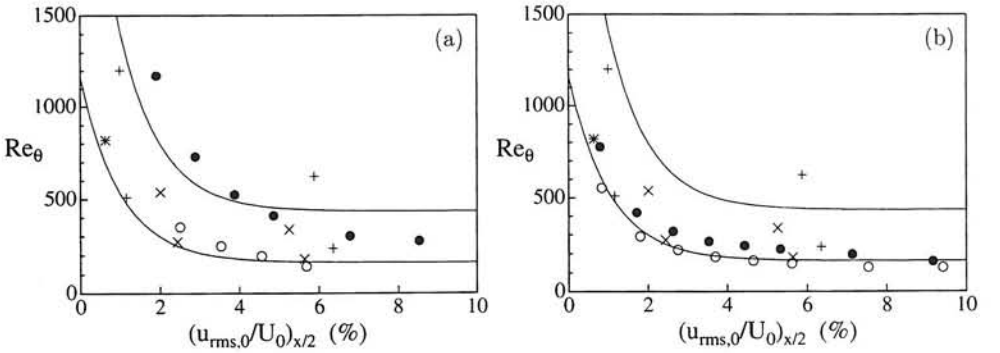

Figure 6.15: The start and end of the transition region (lower and upper curves respectively) in terms of Re_θ as compared with the empirical correlation of Abu-Ghannam & Shaw (1980) for a zero-pressure gradient boundary layer: experiments (KTH) (+), experiments (Rolls-Royce) ($\times, *$), calculated start and end of the transition region ($\circ, \bullet$). (a) Calculations with the HJH-model; (b) calculations with the model by Launder & Sharma. (Note that only the start of the transition region ($*$) is available for the T3A$^-$ case by Rolls-Royce.)

6.2.6 Comparison with predictions based on the e^N-method

The dominating method for transition prediction in external aeronautical applications (i.e. the level of free stream turbulence and noise is relatively low) is the e^N-method. The method was developed independently by Smith & Gamberoni (1956) and van Ingen (1956), and relates the start of the transition region to an empirical value of the maximum amplification rate [1] of Tollmien-Schlichting waves. Thus, in order to predict transition, stability calculations are carried out for the considered geometry, and the start of the transition region is determined as the position where the amplification rate reaches a critical value (typically between 9 and 11).

However, since the method is merely a measure of the amplification rate, and does not take the initial amplitude of the disturbances into account, the use is restricted to small outer disturbance levels. Some attempts to adjust the critical value of the N-factor to the FST-level have been carried out, for instance van Ingen (1977) suggested the following relations for the start (N_{start}) and the end (N_{end}) of the transition region

$$\begin{aligned} N_{start} &= -10.23 - 2.68\ln(Tu) \\ N_{end} &= -7.36 - 2.68\ln(Tu) \end{aligned}$$

and Mack (1977) proposed

$$N_{start} = -8.43 - 2.4\ln(Tu)$$

The described relations are used to calculate the curves displayed in figure 6.16 for a flat plate boundary layer. The amplification rates are calculated using linear parallel theory, and the corresponding critical Reynolds numbers are taken from the Blasius solution. Note that the FST-level for the different experiments are taken at the leading edge of the plate, and not midway between the leading edge and the considered x-position as was the case in the Abu-Ghannam & Shaw correlation. Since the stability calculation assumes that the amplitude of the wave is only dependent on the initial amplitude and the complex part of the wave number, the FST-level at the leading edge seems to be the relevant measure for an adjustment of the critical N-factor.

The predictions of the transition onset for the T3A-case ($Tu = 3\%$) and the KTH-B case ($Tu = 1.35\%$) is rather good, while for higher FST-levels transition starts at a position upstream of the critical Reynolds number for TS-waves ($Re_\theta \approx 200$). The measured end of the transition region differs significantly between different experiments, and also the predictions show large deviations compared with the experimental data. It should be noted that the results differ whether Re_x or Re_θ is considered, since the rapid increase in momentum loss thickness in the transition region is not accounted for in the stability calculations, which assume a Blasius boundary layer throughout the computation domain.

[1] The amplification rate (or N-factor) is defined as $N = ln(A(x)/A(x_0)) = -\int_{x_0}^{x} \alpha_i \, dx$, in which A and α_i are the amplitude and the complex part of the wave number of the TS-wave respectively.

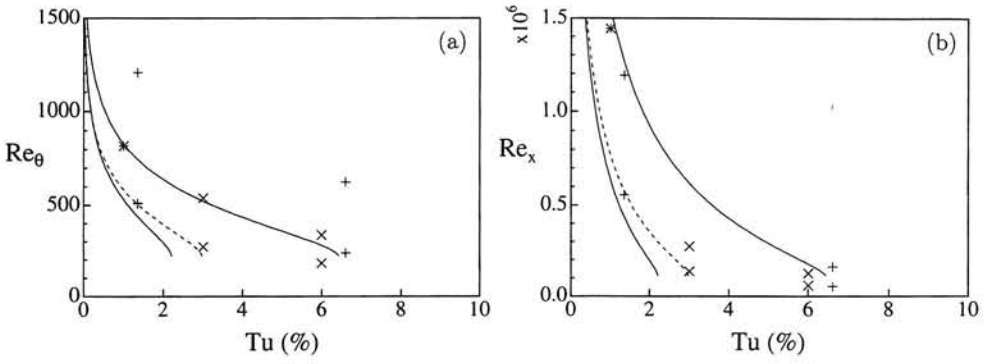

Figure 6.16: Prediction of the start and end of the transition region in terms of (a) Re_θ and (b) Re_x using the e^N-method and the relations suggested by van Ingen (1977) (—) and Mack (1977) (- - -). Experiments: KTH (+); Rolls-Royce ($\times, *$).

6.2.7 Non-zero pressure gradients

The only available test case with non-zero pressure gradient that is meaningful to calculate with the HJH-model is the T3C1-case, which has a FST-level of about 7% at the leading edge. There are a number of cases with $Tu \approx 3\%$, but since the model does not perform well in this range of FST-levels they are not considered here. In the T3C1 experiment transition takes place in the accelerating region of the flow, and the predictions with the HJH-model and the Launder & Sharma model are shown in figure 6.17. Both models predict too early transition, although the deviation from the experimental data is slightly smaller with the HJH-model. At the rear part of the flat plate the turbulent boundary layer is exposed to an adverse pressure gradient, and, as expected, the performance of the HJH-model is clearly better in this region than the $k - \epsilon$ model.

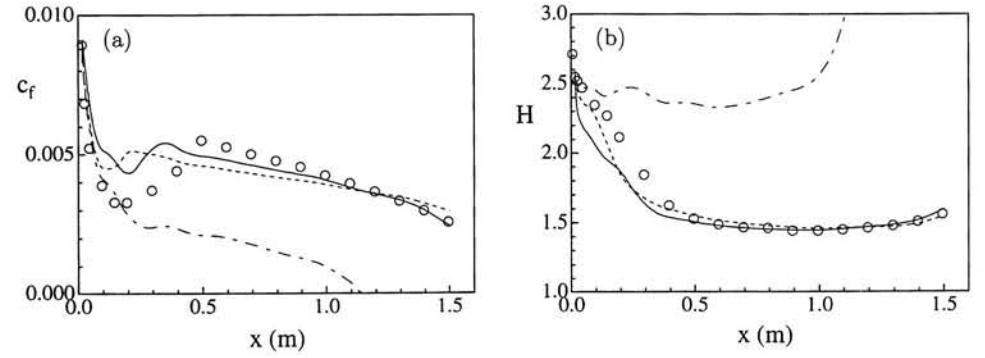

Figure 6.17: (a) Wall-shear stress coefficient and (b) shape factor for a non-zero pressure gradient case (T3C1) at $Tu \approx 7\%$. Experiments (o); calculations with the HJH-model (—), Launder & Sharma $k - \epsilon$ model (- - -) and laminar solution (- · -).

6.2.8 Comparison with LES

The only test case in which the different terms in the transport equations are available is the T3B-LES case. In the present section a detailed comparison between LES-data and calculations with the HJH-model is carried out. The intention is to gain further understanding on how the model behaves through the transition region, and to elucidate the terms that are not satisfactorily modelled. In figure 6.18a the wall-shear stress coefficient extracted from the LES-data is compared with calculations starting from two different initial conditions. The "standard IC" gives a slightly delayed transition, and from figure 6.18b it can be observed that the growth of u_{rms} is underpredicted. The second calculation, starting at $x = 25$ mm with initial conditions from the LES, gives better predictions of both the location of the transition region and the growth of u_{rms}, although the amplitude of the u-perturbations saturates earlier than in the LES. From the second calculation different profiles as well as different terms in the Reynolds stress equations are extracted and compared with the LES data at $x = 45$ mm ($Re_x = 3 \times 10^4$), $x = 95$ mm ($Re_x = 6.3 \times 10^4$) and $x = 195$ mm ($Re_x = 1.3 \times 10^5$).

The profiles shown in figure 6.19a-f are not scaled in the y-direction, which enables a comparison of how the growth of the boundary layer is predicted. Both the shapes of the mean-velocity profiles and the u_{rms} profiles are in relatively good agreement with the LES, and the y-locations where the maxima in u_{rms} appear are also well-predicted for all stations. However, the amplitude of the streamwise fluctuations is considerably underpredicted for the higher Reynolds numbers. The shapes of the calculated v_{rms}- and w_{rms}-profiles reveal larger deviations from the LES-data, and a large overprediction of w_{rms} can be observed at the last station. This is consistent with the experimental T3B-case, in which the calculations overpredict the $\overline{ww}$-stresses in the turbulent region. The profiles of $\overline{uv}$ show a relatively good agreement regarding the shapes, although the amplitude maxima in the pre-transitional profiles are located slightly below the maxima extracted from the LES. The amplitude development is somewhat difficult to interpret, as it is partly overpredicted, partly underpredicted. This makes it difficult to conclude whether $\overline{uv}$ is exaggerated or not in the regions where the amplitude of $\overline{uu}$ is well-predicted (cf. discussion in section 6.2.4). At the first station ($x = 45$ mm) the amplitude of $\overline{uu}$ is in almost perfect agreement with the LES, while the calculated $\overline{uv}$-profile is overpredicted with almost 20%. However, at the consecutive stations both $\overline{uu}$ and $\overline{uv}$ are below the amplitudes extracted from the LES.

The last plot in figure 6.19 shows the dissipation profiles. It is clear that the dissipation is severely overpredicted in the middle of the pre-transitional boundary layer, which will thus counteract the production of $\overline{uu}$. As the boundary layer develops towards the turbulent state, the dissipation profiles become in better agreement with the LES-data. This indicates that the present model is not well-suited to describe the behaviour in the pseudo-laminar layer, despite the fact that the location of the transition region is well-predicted in the present test case. A second discrepancy which is observable in all dissipation profiles is the large near wall peak in the LES-data, which is absent in the modelled profiles. This peak in the LES, however, is to a large extent balanced by the pressure diffusion which in the $\overline{uu}$-equation is significant close to the wall. In the present turbulence model there is no separate term which aims to model the pressure diffusion, and a good agreement close to the wall can not be expected.

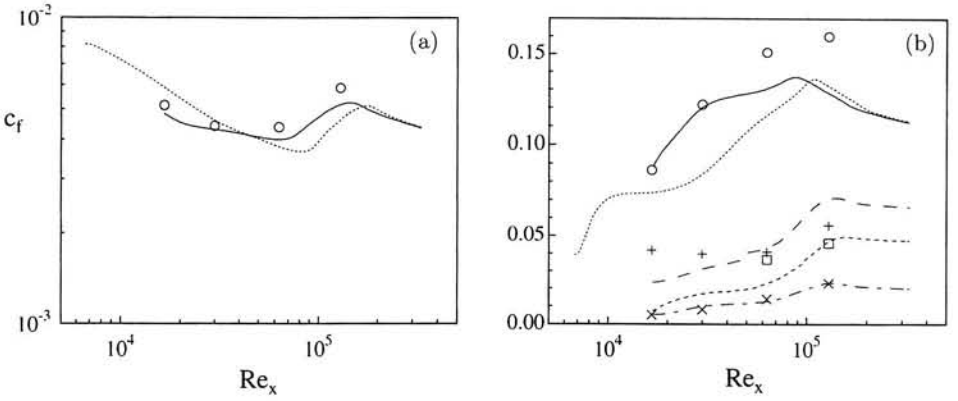

Figure 6.18: (a) Predicted wall-shear stress in the T3B-LES case. LES-data (○), HJH-model with initial conditions from LES (—), HJH-model with "standard IC" (· · ·); (b) Maximum level of u_{rms}/U_0 (○ , —), v_{rms}/U_0 (□ , - - -), w_{rms}/U_0 (+ , – –) and $-10\,\overline{uv}/U_0^2$ (× , – · –) inside the boundary layer. Symbols and lines show results from LES and calculations with the HJH-model (initial conditions from LES) respectively. u_{rms}/U_0 calculated with the HJH-model starting from the "standard IC" (· · ·).

Reynolds stress balances

In figures 6.20 to 6.23 the different terms in the Reynolds stress equations are plotted and compared with the corresponding budgets extracted from the LES. In the present turbulence model the influence from pressure diffusion is not modelled separately, but can be considered as included in the pressure strain terms. Thus, in order to simplify the comparisons, the contribution from pressure diffusion is added to the pressure strain term also in the balances extracted from the LES. In agreement with observations in the previous section the $\overline{uu}$-balance at $x = 45$ mm shows an overestimation of both the production and the dissipation, resulting in a well-predicted amplitude of $\overline{uu}$. At $x = 95$ mm the dissipation in the middle of the boundary layer is in relatively good agreement with the LES, but instead the production is underestimated and the level of $\overline{uu}$ is too low (figure 6.19b). It can also be observed for the downstream x-stations that both the turbulent transport and the viscous diffusion are smaller with the HJH-model compared with the LES-data. This can partly be explained by the underpredicted level of $\overline{uu}$ together with the gradient-diffusion hypothesis, which result in smaller transport terms. It should finally be noted that the pressure terms are overpredicted at the last station, which means that too much energy is redistributed from the streamwise component to the transversal components in the turbulent boundary layer. A corresponding overestimation (with positive sign) can consequently be observed in the balances for $\overline{vv}$ and $\overline{ww}$.

The budgets for $\overline{vv}$ are dominated by the pressure terms and the dissipation, and both terms are overestimated in the modelled equation. A large increase of the pressure strain can be observed in the transition region, which is one of the key-events in the process from laminar to turbulent flow. In figure 6.24 the different pressure-strain terms are plotted for the $\overline{uv}$- and $\overline{vv}$-equation. When transition starts between $x = 95$ mm and 195 mm there is a significant increase in both the rapid and slow pressure strain terms, where especially the

latter ($\phi_{ij,1}$) is enhanced when the transition region is entered.

The $\overline{ww}$-balances resemble in many respects the $\overline{vv}$-balances, with the production being identical to zero and with a main contribution from the pressure strain terms. It is interesting to note that although the pressure diffusion is zero in the LES-data (no spanwise gradients), the dissipation has a maximum at the wall in the last profile. This is not reproduced by the HJH-model, which has the maximum at a distance from the wall. This near-wall behaviour for ϵ is a general shortcoming for many second-order near-wall closures (cf. So *et al.* 1991).

The last transport equation, the $\overline{uv}$-equation, suffers from the general deficiency in the model, i.e. a severe overprediction of the dissipation. In the pseudo-laminar region the production of $\overline{uv}$ is overestimated by the turbulence model due to a larger value of $\overline{vv}$ close to the wall (the production of $\overline{uv}$ is dominated by $-\overline{vv}\,\partial U/\partial y$). The large production is partly balanced by the overestimated dissipation, although the largest counteracting contribution is associated with the pressure strain terms. It should be mentioned that if the pressure term in the LES is split into pressure strain and pressure diffusion, there is a reasonable agreement between the modelled pressure strain and the pressure strain of the LES (except close to the wall). Since the pressure diffusion is counteracting the pressure strain in the middle of the boundary layer, the level of the pressure term in the displayed LES-balance is smaller than the modelled term. Finally, at the last station, the production term is even more overpredicted in the turbulence model. This results in an increased contribution from the rapid pressure strain term, which is modelled in terms of the production.

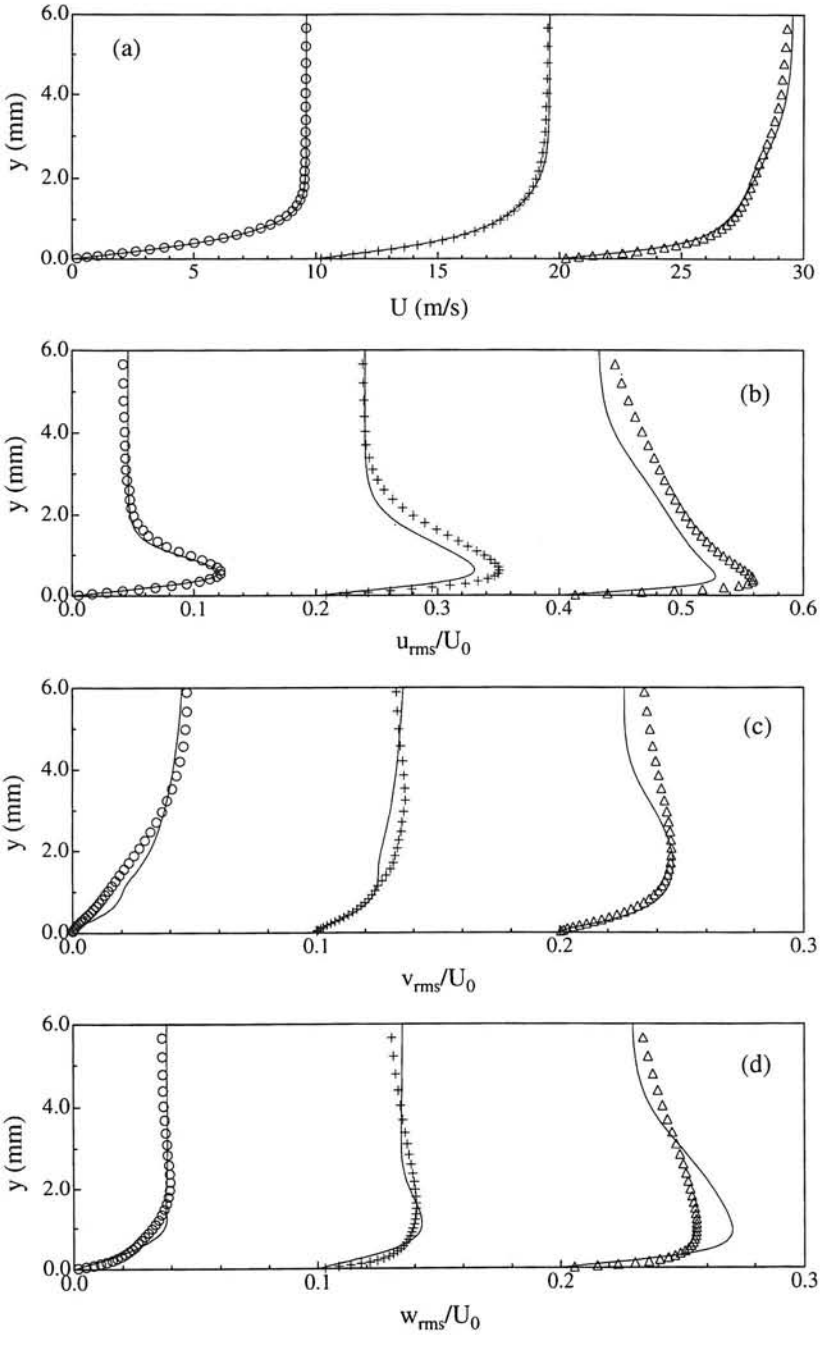
(a)
y (mm)
U (m/s)
(b)
u_{rms}/U_0
(c)
v_{rms}/U_0
(d)
w_{rms}/U_0

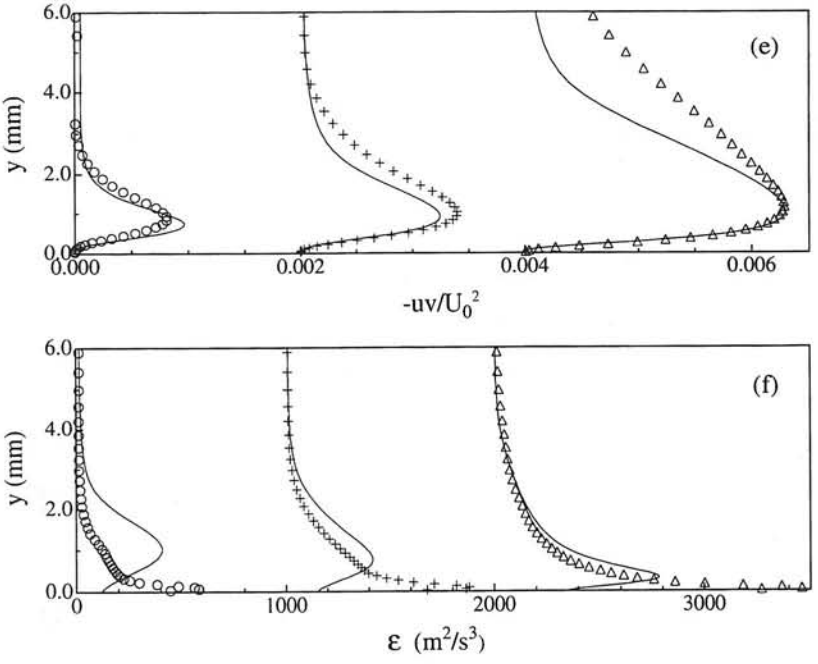

Figure 6.19: Different profiles extracted from LES-data (symbols) and calculations with the HJH-model starting from LES-IC (lines). The x-positions are 45 mm ($Re_x = 3 \times 10^4$) ($\circ$), 95 mm ($Re_x = 6.3 \times 10^4$) ($+$) and 195 mm ($Re_x = 1.3 \times 10^5$) ($\triangle$). (a) Mean velocity profiles (U), (b) u_{rms}/U_0, (c) v_{rms}/U_0, (d) w_{rms}/U_0, (e) $-\overline{uv}/U_0^2$, (f) ϵ.

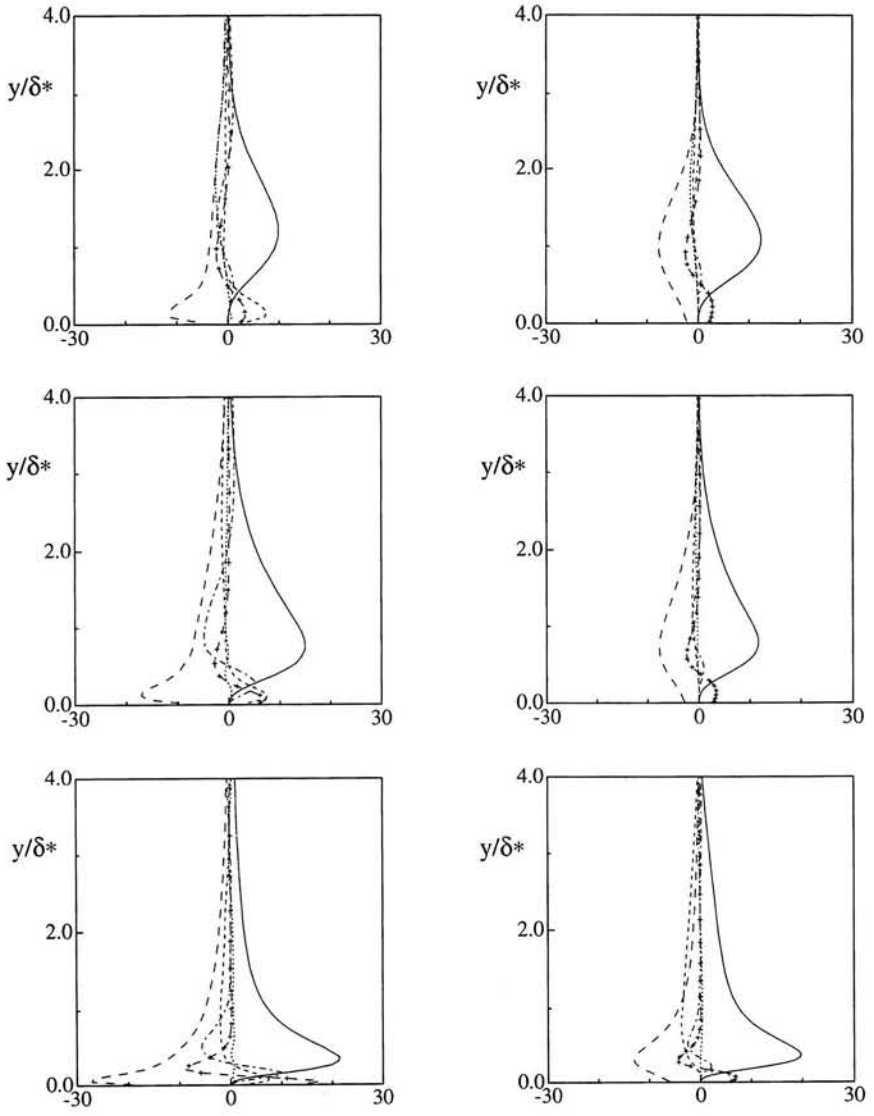

Figure 6.20: Terms in the balance of $\overline{uu}$. Left column: LES, Right column: HJH-model starting from LES-IC. The figures from top to bottom corresponds to $x = 45$, 95 and 195 mm respectively. Labels: production (—), convection ($\cdots$), turbulent transport ($-\cdot-$), pressure terms (total) (---), viscous diffusion ($-+-$), dissipation ($- -$).

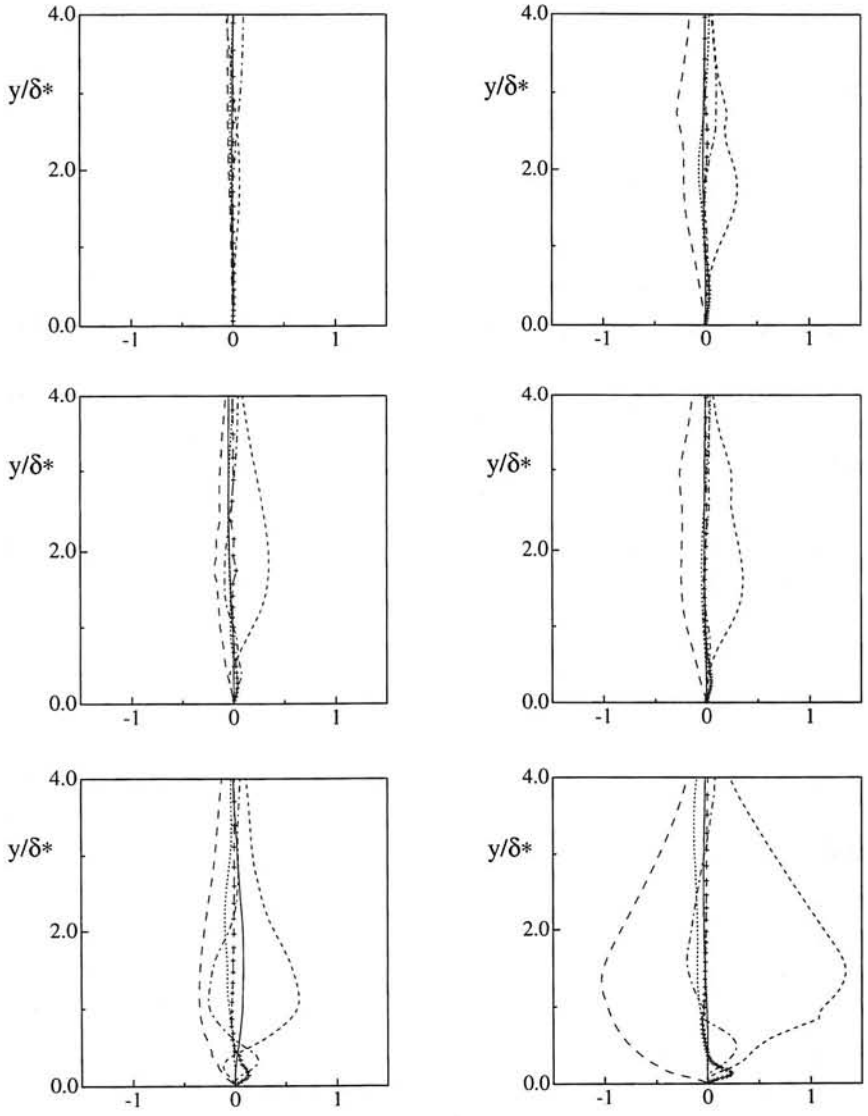

Figure 6.21: Terms in the balance of $\overline{vv}$. Figures and labels as in figure 6.18

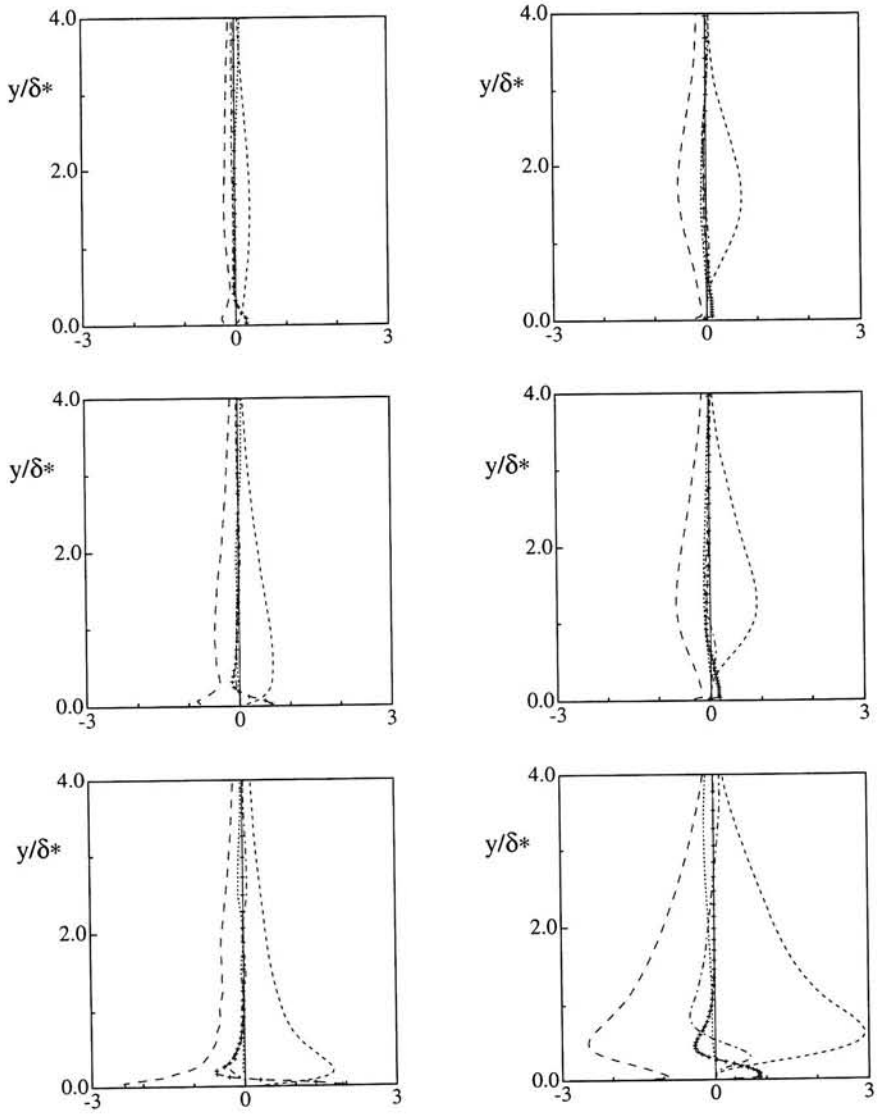

Figure 6.22: Terms in the balance of $\overline{ww}$. Figures and labels as in figure 6.18

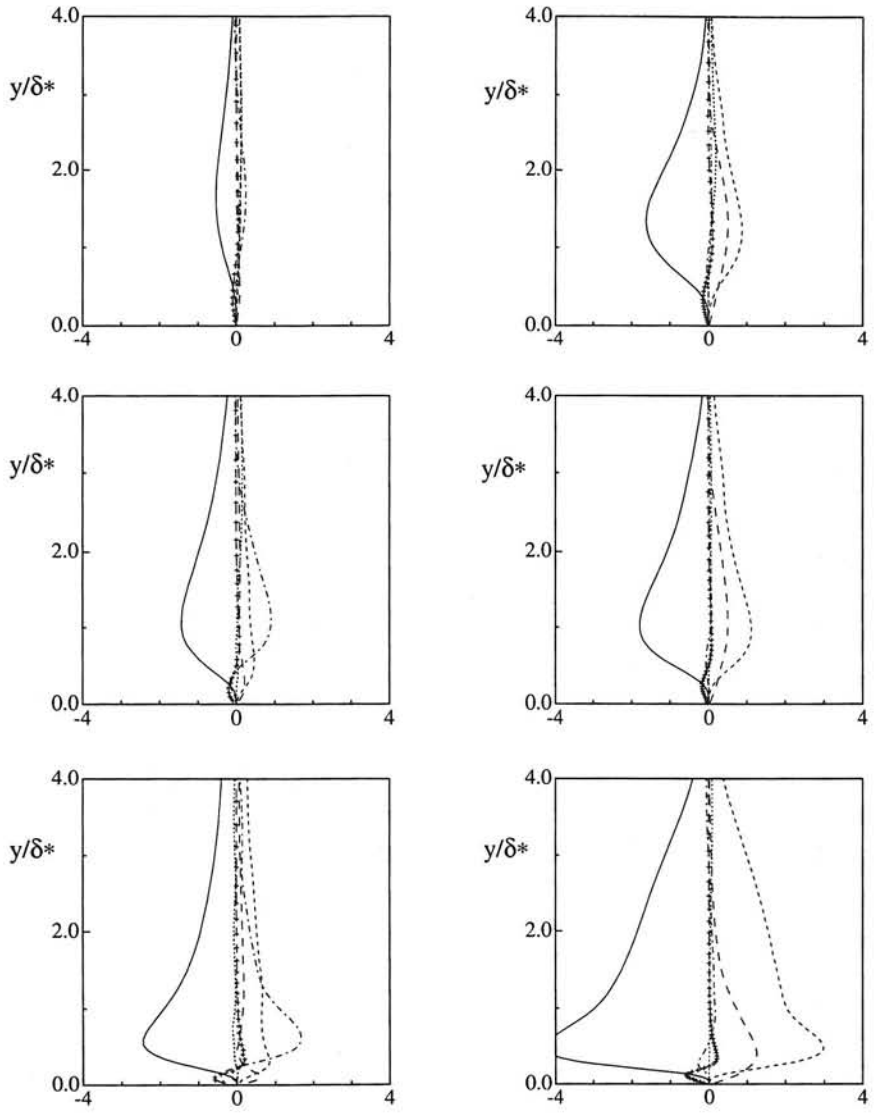

Figure 6.23: Terms in the balance of $\overline{uv}$. Figures and labels as in figure 6.18

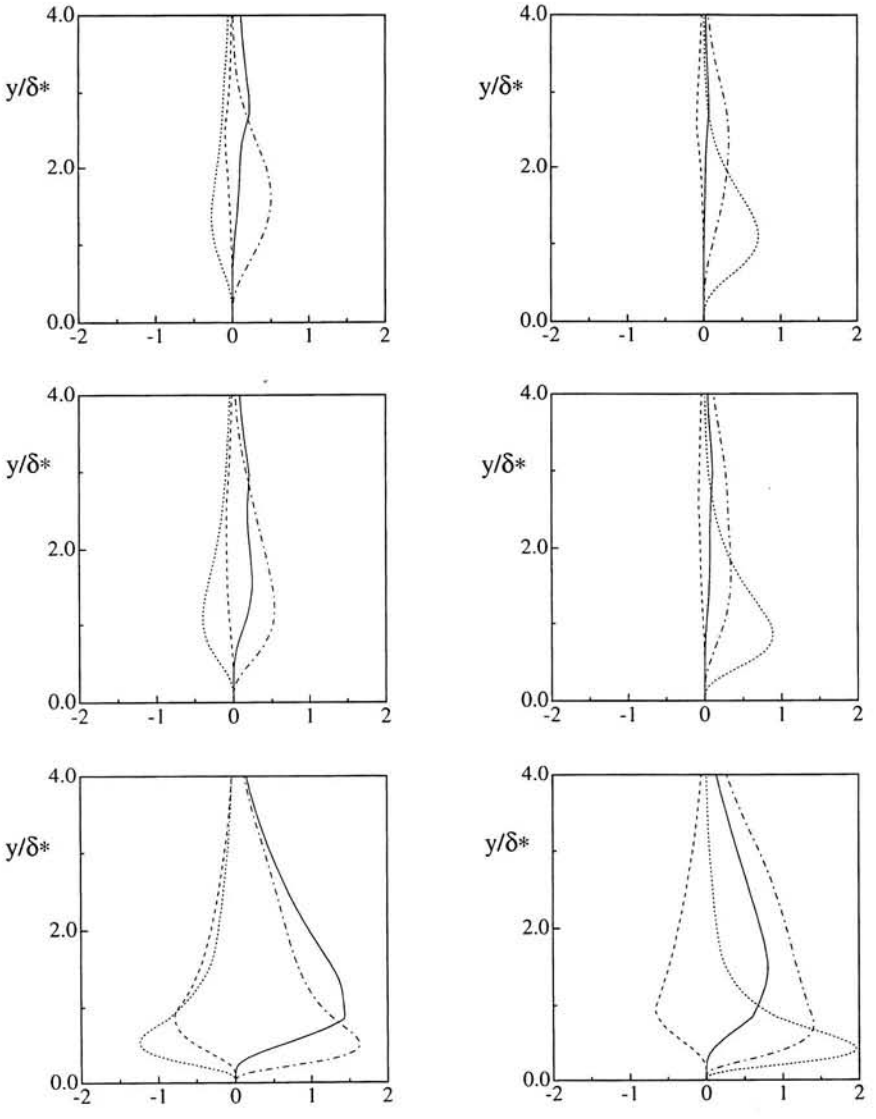

Figure 6.24: Pressure strain terms. Left column: $\overline{vv}$-equation, Right column: $\overline{uv}$-equation. Labels: $\phi_{ij,1}$ (—), $\phi^w_{ij,1}$ ($\cdots$), $\phi_{ij,2}$ (-·-) and $\phi^w_{ij,2}$ (---).

A transition scenario

Although there are several discrepancies between the results from the modelled equations and the LES-data, the general behaviour is in many respects similar. Yang & Voke (1993) have proposed a transition scenario based on the statistical data extracted from the LES, which is schematically summarized by Savill (1996) and shown in figure 6.25. The results elucidate the different roles that the u- and v-fluctuations have in the different stages of the transition process. In the initial stage there is a production of $\overline{uv}$ inside the boundary layer, caused by the overlap between the wall-normal fluctuations in the free stream and the mean shear in the laminar boundary layer. At this stage there is no production or redistribution of energy to the $\overline{vv}$-stresses, and the v-fluctuations observed inside the boundary layer is only dependent on the turbulent free stream. Since the $\overline{vv}$-stresses are continuously decaying towards the wall due to kinematic wall-damping, the magnitude of the production term in the $\overline{uv}$-equation will be dependent both on the level and on the dominating scales in the free stream. If the turbulent scales are large, the damping will start far outside the boundary layer edge, and the remaining level of $\overline{vv}$ inside the boundary layer will be small. The produced $\overline{uv}$ determines the production of $\overline{uu}$ which results in the growth of u_{rms} in the pseudo-laminar boundary layer.

The second stage of the transition process is more rapid, and, as pointed out by Yang & Voke, less clear. After the initial region with growth of $\overline{uu}$ the redistribution of energy to $\overline{vv}$ and $\overline{ww}$ through the pressure strain terms suddenly becomes active. The increase in $\overline{vv}$ will in turn increase the production of $\overline{uv}$ and a feedback loop appears in the scheme shown in figure 6.25. Once the redistribution of energy has started the transition process becomes very rapid.

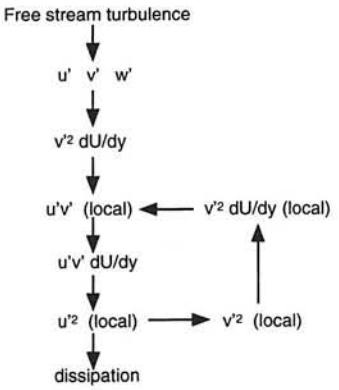

Figure 6.25: Schematic picture over a transition scenario (from Savill 1996).

6.2.9 Attempts to improve the model

During the course of the study different attempts to modify the model have been undertaken, with the intention to improve the prediction for the T3A-case. However, all modifications that have been tested have also affected the behaviour in the T3B-case. A modification that gives an upstream movement of the transition region in the T3A-case, inevitably results in

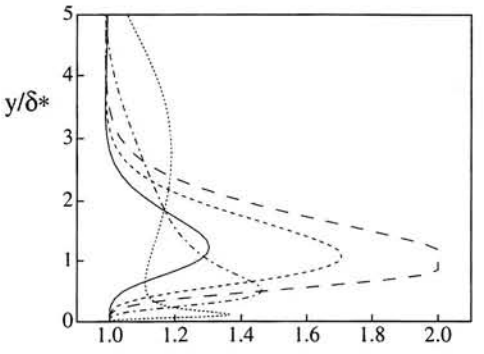

Figure 6.26: The function 6.1 plotted at different streamwise stations in calculations with the HJH-model for the T3B-case. Labels: $x = 45$ mm (—), 70 mm (- - -), 95 mm (– –), 195 mm (– · –) and 1495 mm (· · ·).

too early transition for the T3B-case. This is illustrated with some examples in the sequel of this section.

From the Reynolds-stress balances it was concluded that a major event in the transition process predicted by the HJH-model was an increased redistribution from $\overline{uu}$ to $\overline{vv}$ stresses, due to an increase in both the slow and the rapid pressure strain terms. Both terms are rather small in the pseudo-laminar region (cf. figure 6.24), despite the fact that the fluctuations are very anisotropic in this region, and the production term (which governs the modelled rapid pressure strain) is also large. However, this is mainly because both C_1 and C_2 are functions of the anisotropy measure A, which is one for isotropic turbulence and zero in the two-component limit. Since the fluctuations in the pseudo-laminar region are rather anisotropic also in the central part of the boundary layer, C_1 and C_2 are small in this region and the redistribution does not become as rapid as can be expected in a model where C_1 and C_2 are constants.

One of the initial ideas to modify the model was to stimulate the redistribution of $\overline{uu}$ into $\overline{vv}$ in the central part of the boundary layer, with the intention to increase the production of $\overline{uv}$ in the pre-transitional region, and to speed up the feedback (cf. figure 6.25) that appears at the transition onset. In figure 6.26 the wall-normal profiles of the function

$$1 + \min\left\{\frac{Re_t\, A_3}{100}; 1\right\} \tag{6.1}$$

are plotted at different stations in a calculation of the T3B-case. The function is used to enhance either the slow or the rapid pressure strain by multiplication with the original C_1 or C_2 term. Consequently, the main effect is an increased redistribution in the pre-transitional region, while the effect on the fully turbulent boundary layer is relatively small. It should be emphasized that 6.1 is not based on any physical arguments, but is formulated in order to obtain a function which has a maximum in the central part of the pseudo-laminar layer.

Figures 6.27 and 6.28 show the results when 6.1 is multiplied with the slow and the rapid pressure strain term respectively. It can be observed that the transition becomes much more rapid in the T3A-case, and also the start of the transition region is moved slightly upstream

when the rapid pressure strain is enhanced. However, from the plots of the downstream development of the maximum in $\overline{uu}$ it is clear that the modifications do not improve the prediction of the fluctuations in the pseudo-laminar region. Further, the predictions for the T3B-case become much too early.

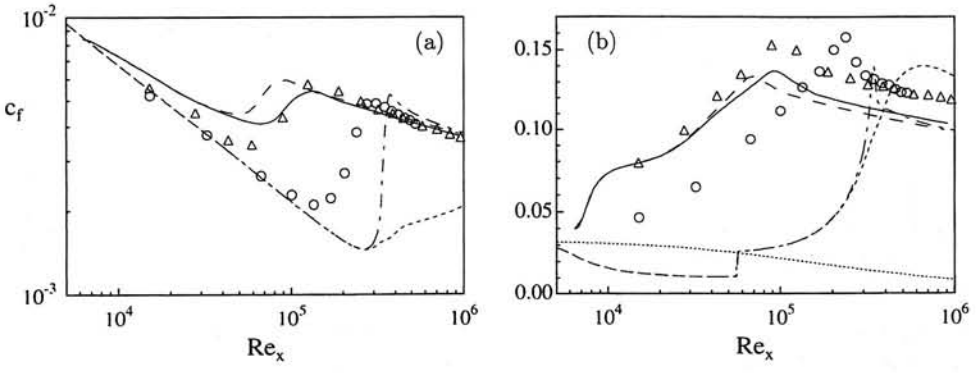

Figure 6.27: (a) Wall-shear stress coefficient and (b) development of maximum u_{rms}/U_0 calculated with the original HJH-model and with the slow pressure strain term (C_1-term) multiplied with the function 6.1. Experiments: T3A (o), T3B ($\triangle$); Original HJH-model: T3A (---), T3B (—); Modified HJH-model: T3A (-·-), T3B (– –); FST-level (· · ·).

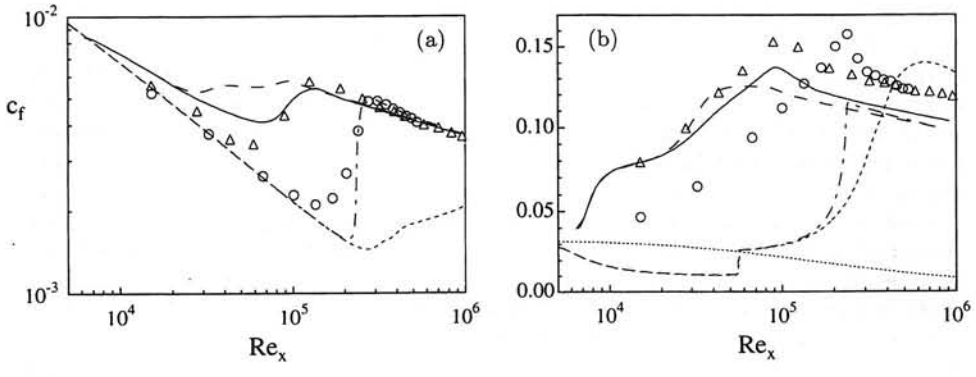

Figure 6.28: (a) Wall-shear stress coefficient and (b) development of maximum u_{rms}/U_0 calculated with original HJH-model and with the rapid pressure strain term (C_2-term) multiplied with the function 6.1. Labels as in previous figure.

Comparison with LES-data in section 6.2.8 revealed discrepancies in the modelled dissipation profiles, especially in the pre-transitional region. In figure 6.29 a minor change to reduce the dissipation has been applied, namely the additional production term (with coefficient $C_{\epsilon 3}$) is switched off. The modification only intends to give a qualitative impression of the effects. The growth of the u-fluctuations is significantly improved in the T3A-case and the start of the transition is moved upstream, although the development inside the transition region is still very slow. However, as can be expected, the reduced dissipation results in an

overpredicted growth of $\overline{uu}$ and an upstream movement of the transition region also in the T3B-case.

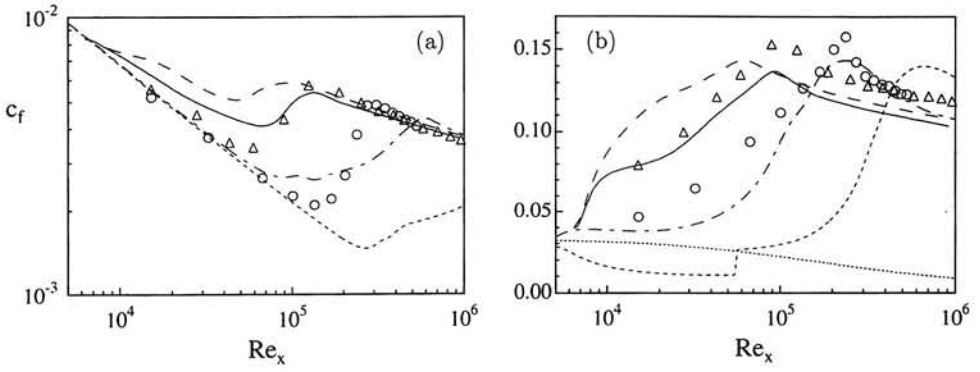

Figure 6.29: (a) Wall-shear stress coefficient and (b) development of maximum u_{rms}/U_0 calculated with the original HJH-model and with a modification in the dissipation equation ($C_{\epsilon 3} = 0$). Labels as in previous figure.

6.2.10 Discussion

When considering the transition scenario of Yang & Voke and the data from the LES it seems that the modelling of the growth of u_{rms} in the pseudo-laminar layer is important. In the cases where the HJH-model gives a good prediction of the location of the transition region, this pre-transitional growth has at least partly been captured. This is somewhat encouraging, although a more detailed investigation reveals that this is attained despite discrepancies in the modelled equations. A general shortcoming which affects all Reynolds Stress equations is the poor prediction of the dissipation in the pre-transitional region of the boundary layer. One can expect that the dissipation in the middle of the boundary layer is very small, since the perturbations are dominated by large scale structures. This is also corroborated by the LES, in which the magnitude of the dissipation profiles is small everywhere except very close to the wall.

The model of the dissipation equation that are used in the present calculations as well as in most one-point closures relies on the high-Reynolds-number hypothesis. This means that the small scales where the dissipation takes place are passive, and that their size is determined from the energy that is transferred from the larger scales. In other words, the dissipation is determined by the larger, energetic vortices, and not by the small viscous scales. This is a basic assumption in the currently used equation for ϵ, which rather serves as a model for the energy transfer from larger to smaller scales, than a model for ϵ itself. However, in the pseudo-laminar boundary layer the energy spectra shows a significant contribution in the larger scales, while the small scale structures are almost absent. Consequently, the assumption that the production of ϵ is directly related to the production of Reynolds stresses may not be a good approximation in the pseudo-laminar layer, and an overpredicted dissipation can be expected.

The modifications in the model that were tested in the previous section confirmed that

the initial growth of $\overline{uu}$ is largely dependent on the dissipation, although some more general modifications than just tuning the constants are necessary. One possibility which has recently been tested in a two-equation model is to introduce a time-lag in the growth of the dissipation by using a separate relaxation equation (Franzmann 1996). The usual model of the dissipation equation is solved also in this case, but the result, which is considered as the energy transfer from the larger to the smaller scales in the spectra, is not directly introduced into the k-equation. Instead the dissipation of energy is determined from the additional relaxation equation. This extension could be interesting to implement with a second-moment closure as well.

In section 6.2.9 it was also confirmed that the pressure strain plays an important role for the development inside the transition region in calculations with a DSM-model. At present time it is unclear what causes the sudden redistribution of $\overline{uu}$ into $\overline{vv}$, which can be observed in the LES, while it is absent during the initial phase of growing u-fluctuations. It is likely that the understanding of this mechanism is the key to the understanding of transition at high levels of FST. One should, however, emphasize that the transition scenario proposed above is based on statistical averages extracted from the LES. Even if the simulation may give a correct description of the dynamics inside the boundary layer, the averaging process can remove many of the important details. In chapter 2 some experiments and simulations were mentioned in which unstationary, longitudinal streaks were observed in the pseudo-laminar boundary layer. There have also been indications both from flow visualizations and simulations that the streaks are subjected to secondary instabilities just prior to breakdown. This is usually observed as spanwise oscillations. A plausible assumption is that the sudden redistribution of energy through the pressure strain terms that can be observed in the $\overline{vv}$- and $\overline{ww}$-balances is caused by those secondary instabilities. Consequently, in order to come up with a model of the pressure strain terms which can correctly describe this mechanism, further understanding of the nature of the secondary instabilities is required.

6.3 The SLY-model

The SLY-model is a Differential Reynolds Stress Model which is tuned in order to perform well for transitional flows. In this study the so-called "basic SLY-model" is used, which does not include terms intending to model pressure diffusion and non-local effects of the pressure strain. These extensions were added in later versions of the model, however, Savill (1995a) reported that also the "basic SLY-model" has shown good results for transition prediction.

In figure 6.30 the calculated wall-shear stress coefficient and shape factor are shown for the T3A and T3B cases. The "standard" initial conditions are used, and the turbulent length scales, which give a decay of the FST in good agreement with experiments, are 9.8 mm and 24 mm for the T3A and T3B-case respectively. For both test cases the predicted location of the transition region is considerably late. The start of transition, estimated from the local minimum in the wall-shear stress curve, is about 50% too late in the T3B-case. Also the length of the transition region is erroneous, with an overestimated length of roughly 70-80%. This is, however, concealed by the logarithmic scale in figure 6.30. In the T3A-case the calculation fails completely, and the transition region starts at a Reynolds number (Re_x) which is almost 600% larger than observed in the experiments. A calculation with an initial turbulent length scale of 30.1 mm is also plotted, which gives a too slow decay of the FST as compared to the experiments (cf. figure 5.2). The slower decay rate turns out to have a

dramatic effect on the predicted transition location, which moves upstream. However, the predicted start of the transition is still approximately 100% too late. Apparently, the model is extremely sensitive to the free stream boundary conditions, at least for relatively low levels of FST. Further, calculations of the T3A$^-$-case ($Tu = 1\%$) did not result in transition within the considered computational domain ($Re_x \leq 6.4 \times 10^6$).

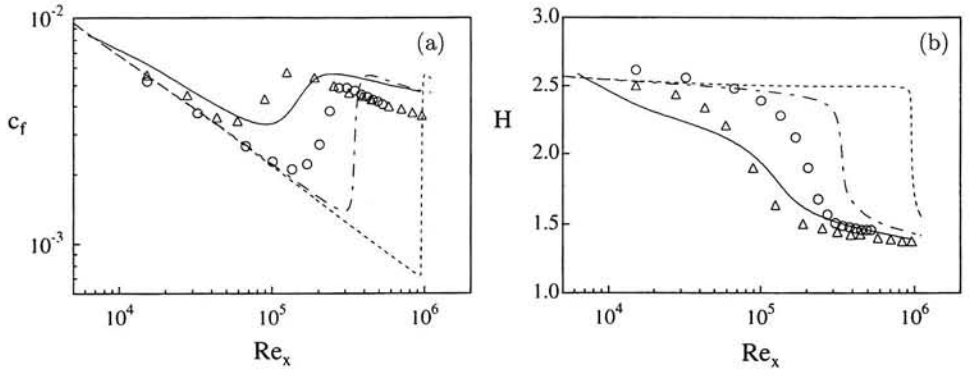

Figure 6.30: Transition prediction with the SLY-model for the T3A and T3B test cases. (a) Wall-shear stress coefficient; (b) Shape factor. Experiments: T3A (○), T3B (△). Calculations: T3B with $l_{t0} = 24$ mm (—), T3A with $l_{t0} = 9.8$ mm (- - -) and T3A with $l_{t0} = 30.1$ mm (-·-).

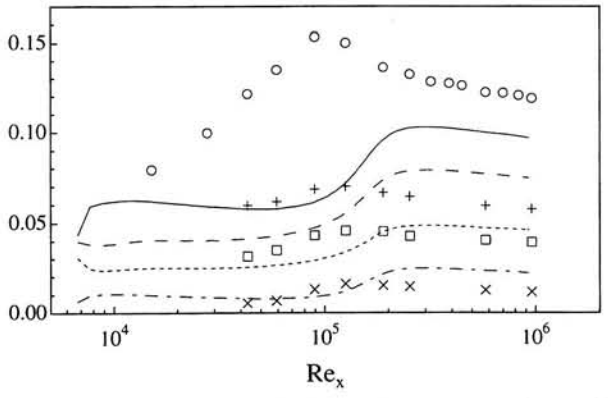

Figure 6.31: Downstream development of the maximum level of u_{rms}/U_0 (○, —),v_{rms}/U_0 (□, - - -),w_{rms}/U_0 (+, – –) and $-10\,\overline{uv}/U_0^2$ (×, -·-) inside the boundary layer for test case T3B.

The downstream development of the maximum level of the Reynolds stresses in the boundary layer are plotted in figure 6.31. The normal stresses show an almost constant level in the pseudo-laminar region, and an increase is only observable close to transition. Thus, the growth of the disturbance energy is very small in the laminar region, and plots of individual profiles of the kinetic energy show a continuous damping of the free stream turbulence to-

wards the wall. This result is in contrast to the predictions with the HJH-model, for which especially the $\overline{uu}$-Reynolds stresses grow significantly in the pre-transitional boundary layer.

The calculated wall-shear stress in the turbulent region is in figure 6.30 much larger than in the experiments. Comparisons with the experiment by Wieghardt & Tillmann in a fully turbulent boundary layer gave an overprediction of c_f with approximately 30% at $Re_\theta \approx 15000$. This discrepancy can be associated with the non-consistent near-wall behaviour of the ϵ-equation in the present formulation of the SLY-model. As pointed out in section 3.2.2 the term $C_{\epsilon 2} f_{\epsilon 2} \epsilon^2 / k$ grows towards infinity close to the wall, which must be balanced by the viscous diffusion term. However, in more recent versions of the model this deficiency has been corrected by an additional pressure diffusion term (Savill, private communication)

The present calculations with the SLY-model show very large discrepancies compared with the results reported by Savill (1995a), in which the transition predictions were in almost perfect agreement with experiments for test cases with Tu ranging from 1%–10%. In contrast, the present calculations predict transition far downstream of the experimentally determined transition locations, especially for lower FST-levels. Reasons for these discrepancies will be discussed in the following sections.

6.3.1 Influence of initial conditions

The influence of the initial conditions was examined in the same manner as in section 6.2.4, using three different sets of initial conditions ("standard IC", rescaled DNS-profiles and "standard IC" with $\overline{vv}$ damped for $y < 10$ mm). For the T3B-case the profiles are identical to the ones shown in figure 6.11, while for the T3A-case the initial profiles differ slightly due to the necessary re-scaling. The calculated wall-shear stress curves in figure 6.32 corroborate earlier observations by Savill, i.e. that the model is relatively insensitive to variations in the initial profiles. This conclusion is valid for both test cases shown in figure 6.32, although there is a delay of the start of transition in the T3A-case when the v-fluctuations are damped outside the boundary layer edge. However, considering the large sensitivity to the decay rate of the FST which could be observed in figure 6.30, this delay is relatively small.

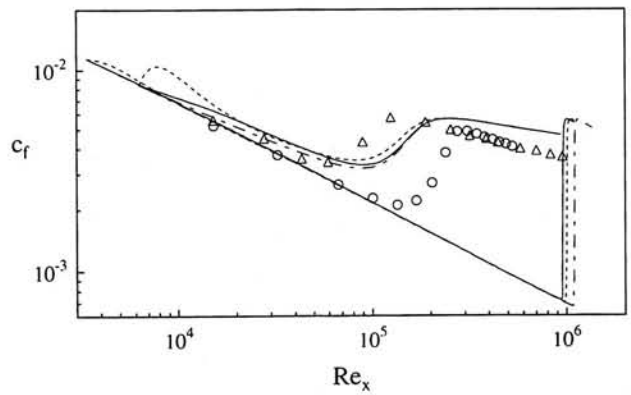

Figure 6.32: Wall-shear stress calculated with different initial conditions for the T3A and T3B-case. "Standard IC" (—), rescaled DNS-profiles (- - -), "standard IC" but $\overline{vv}$ damped for $y < 10$ mm (–·–). Experiments: T3A (o), T3B (△).

A comparison of figures 6.12 and 6.32 indicates that the HJH-model is more sensitive to the initial conditions than the SLY-model, at least for the T3B-case. This may be explained by the different behaviour that the two models exhibit in the pseudo-laminar layer. With the HJH-model the level of $\overline{vv}$ in the vicinity of the boundary layer edge determines to a large extent the production of $\overline{uv}$, which consequently influences the growth of $\overline{uu}$. Thus, a high level of $\overline{vv}$ close to the boundary layer edge enhances the production of $\overline{uu}$ which results in early transition. With the SLY-model, however, the free stream turbulence does not produce a growing maximum of $\overline{uu}$ inside the pseudo-laminar boundary layer (just a slow movement of kinetic energy towards the wall). Although the initial development is affected by changing the initial conditions, these differences are quickly equalized, and after a short distance of adjustments the Reynolds stresses follow the rather constant levels shown in figure 6.31.

6.3.2 Influence of computational domain

In order to detect the discrepancies between the present calculations and the ones by Savill, a thorough comparison between the two computer codes was undertaken. Dr Savill generously provided his computer code, which has an expanding grid in contrast to the fixed domain that is used in the present calculations. Another difference compared with the present code is the free stream boundary conditions. Instead of using homogeneous Neumann boundary conditions, the downstream decay of the free stream turbulence as well as the increase of the turbulent length scale are specified by Dirichlet boundary conditions. These are based on experimentally determined expressions for Tu and l_t. The grid expansion is dependent on the wall-normal growth of the $\overline{uv}$-profiles, i.e. the magnitude of $\overline{uv}$ at a position close to the outer edge of the grid is used to determine the expansion rate for the next streamwise step. Since the magnitude of $\overline{uv}$ usually drops to zero within a short y-distance outside the boundary layer, the grid expansion is proportional to the growth of the boundary layer thickness. It should also be mentioned that the initial conditions are taken from the input file which was enclosed with the code, i.e. $x_0 = 45$ mm and $U_0 = 5.05$ m/s for the T3A-case, which slightly differs from the values used in the previous calculations. The initial turbulent length scale (l_{t0}) is 30.1 mm, which has been shown to be too large, and the initial profiles are the same as specified in the so-called "standard IC".

In figure 6.33 the wall-shear stress curves are calculated using the code by Savill, but with different sizes of the y-domain. The grid is extended in the y-direction by adding grid points outside the previous domain, which means that the same grid resolution is maintained within the boundary layer. In the first calculation the outer boundary of the computational domain is positioned at $y_{max} \approx 1.15\,\delta_{995}$, where δ_{995} denotes the boundary layer thickness defined as the y-position where U reaches 99.5% of U_0. This computational domain is identical to the one specified in the input file by Savill, and results in a location of the transition region in fair agreement with the experiments. However, if the outer edge of the computational domain is extended to $y_{max} \approx 1.9\,\delta_{995}$, the start of transition is delayed with approximately 30%. Further increase of the y-domain leads to slightly further delay, and for $y_{max} > 4\,\delta_{995}$ the solution does not change significantly.

To verify that similar results could be obtained with both computer codes, a calculation was carried out with Savill's code using a non-expanding grid. The grid spacing was specified in order to get almost identical grids in the two codes, and the y-domain was chosen to be $y_{max} = 147.5$ mm. This corresponds to approximately $4\,\delta_{995}$ at the outflow boundary. As can be observed from figure 6.33, the two calculations show good agreement, although there

are small differences observable. However, there are still differences between the two codes, for instance the free stream boundary conditions are specified as Dirichlet and Neumann conditions respectively. With this in mind the agreement can be considered as sufficiently good, and confirms that there are no major numerical differences or discrepancies in the implementation of the turbulence model that affect the transition prediction.

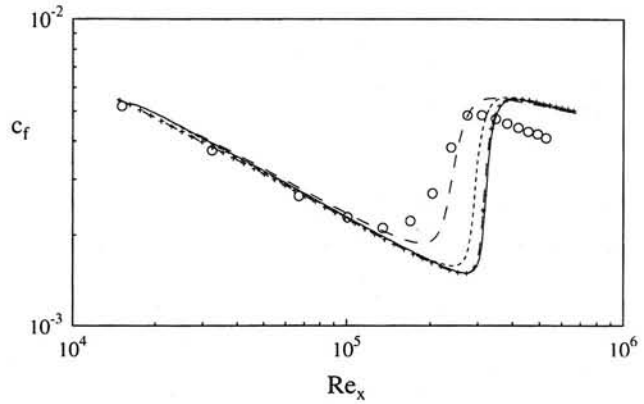

Figure 6.33: Wall-shear stress calculated for the T3A-case, using different size of the computational domain. Expanding grid with $y_{max} \approx 1.15\,\delta_{995}$ (– –), expanding grid with $y_{max} \approx 1.9\,\delta_{995}$ (- - -), non-expanding grid with $y_{max} = 147.5$ mm (—), calculation with the computer code normally used in the present study (–+–).

The significant influence that the computational domain has on the predicted transition position can be understood by comparing individual profiles of the fluctuating components. Figures 6.34a and b show u_{rms} and v_{rms}-profiles at three x-positions, calculated with the three different y-domains. The major reason for the early transition seems to be a combination of a too small computational domain and the use of Dirichlet boundary conditions. In the v_{rms}-profiles, the fluctuation level is continuously damped from the free stream boundary towards the wall. Since the Dirichlet boundary condition implies a predefined turbulence level at the outer edge, a too small y-domain results in an increased v_{rms}-level at the boundary layer edge. In other words, the damping of the v-fluctuations due to the modelled wall-reflection is restricted by the boundary. This gives different results compared with a calculation in which the wall-reflections are allowed to influence on a region solely determined by the model itself.

The last plot in figure 6.34 shows the profiles obtained with the non-expanding grid, using Dirichlet boundary conditions. When the boundary is moved sufficiently far away from the plate, the turbulence level in the free stream is not determined by the boundary condition, but instead determined by the parameters in the turbulence model and the initially specified k_0 and l_{t0}. In the present calculation, using $l_{t0} = 30.1$ mm, the decay rate in the free stream is slower than specified by the boundary conditions, resulting in a kink in the profiles close to the upper boundary. This clearly shows that the length scale (30.1 mm) is incorrect. Another observation is that the redistribution from the v-component to the transversal components is non-zero in the turbulent free stream. This artifact was also observed in the calculations with the HJH-model.

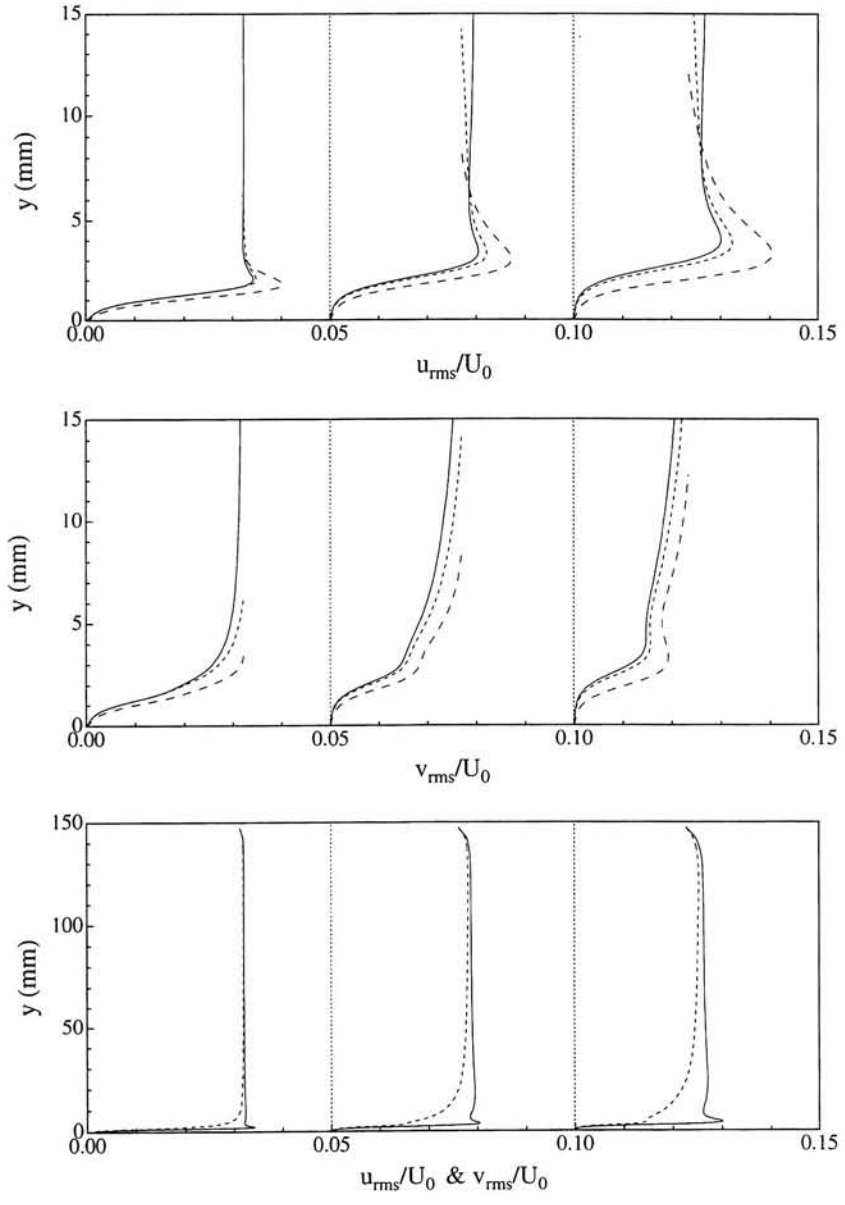

Figure 6.34: Profiles extracted from calculations with the SLY-model using different size of the computational domain. (a) u_{rms}/U_0, (b) v_{rms}/U_0. Labels: expanding grid with $y_{max} \approx 1.15\,\delta_{995}$ (– –), expanding grid with $y_{max} \approx 1.9\,\delta_{995}$ (- - -), non-expanding grid with $y_{max} = 147$ mm (—). (c) u_{rms}/U_0 (—) and v_{rms}/U_0 (- - -) obtained from calculations with a non-expanding grid with $y_{max} = 147$ mm. The x-positions are from left to right 95 mm ($Re_x = 3.2 \times 10^4$), 295 mm ($Re_x = 9.8 \times 10^4$) and 495 mm ($Re_x = 1.64 \times 10^5$).

6.3.3 Discussion

The general conclusion from the calculations with the basic SLY-model is somewhat disappointing, since the model fails to predict the location of the transition region in the simple test cases that are tested in the present study. Also the general behaviour of the model is questionable, as there is almost no energy growth observed in the pseudo-laminar boundary layer. In this respect the behaviour resembles what can be observed in calculations with the Launder & Sharma $k-\epsilon$ model, for which the kinetic energy is fairly constant until it suddenly starts to grow just prior to transition. It seems that the transition process is to a large extent dependent on the coefficients and empirical low-Reynolds number functions in the ϵ-equation. This is not desirable, as the ϵ-equation is the weakest part in turbulence modelling, and, as pointed out in section 6.2.10, is showing severe shortcomings in the pseudo-laminar layer.

A remark should also be made concerning the use of expanding grids. In chapter 2 it was pointed out that the damping of the wall-normal fluctuations usually starts far outside the boundary layer edge, while the $\overline{uv}$-profiles have a non-zero contribution mainly restricted to the boundary layer. The different scaling of the profiles implies that the use of the $\overline{uv}$-profile in order to determine an expansion rate for the grid is not a good choice.

Chapter 7

Final remarks and conclusions

7.1 Two-equation models

From an engineering point of view, two-equation models are attractive due to their simplicity and their relatively low computational cost. In the present study only a few calculations have been performed with a two-equation model, but a rather extensive testing has been performed within the ERCOFTAC Transition SIG. Independent results show that the $k-\epsilon$ model by Launder & Sharma can at least qualitatively give a prediction of the start of the transition region in zero-pressure gradient cases with FST levels from 1% to 6%. However, when the model is applied to different pressure gradients the transition predictions deviate considerably from the experiments. The model by Launder & Sharma also exhibits a general shortcoming for most two-equation models, namely that the length of the transition region is severely underpredicted. Different attempts to correct this has been suggested, for instance the "Production Term Modification" by Schmidt & Patankar (1991), which limits the production term within the transition region.

A sightly more complex approach to improve the modelling of the transition region is to introduce a separate transport equation for the intermittency (cf. Steelant & Dick 1996). The intermittency parameter can be used to weight the contributions from laminar and turbulent flow, in order to prolong the transition region.

A common approach to improve the models with respect to transition prediction is to include empirical information. For instance, the Abu-Ghannam & Shaw (1980) correlation is often used in order to trigger the start of transition, sometimes together with additional modifications to limit the growth of the eddy-viscosity through the transition region. Not surprisingly, models which include a large extent of empirical information usually show the best transition predictions. Impressive results for a wide range of flat plate test cases with and without pressure gradients were obtained by Sieger *et al.* (1995), using a two-layer model. The model combines a $k-\epsilon$ model with a one-equation model close to the wall, and includes various empirical information. However, although the use of empirical information to trigger the start of transition improves the results in relatively simple test cases, it is difficult to judge how these models perform in new and more complicated flow situations.

A common practise to present and compare results from different models within the ERCOFTAC Transition SIG is to plot the wall-shear stress coefficient and the shape factor. This gives a good picture of the location of the transition, but otherwise very limited information about the model behaviour. A thorough comparison of the variations of different terms through the transition region might give some further insight into the mechanisms that

makes the predictive capability of some two-equation models relatively good. At least to the author's knowledge there exist no study which can give a physical explanation, or at least a plausible argument, why it should be possible to predict transition with linear eddy-viscosity models.

One major shortcoming with two-equation models is the assumption of isotropic fluctuations inside the boundary layer, whereas both experiments and simulations show very large anisotropies. Especially from the simulations (Yang & Voke 1993) it can be concluded that the u- and v-fluctuations have very different roles in the different stages of the transition process. In other words it seems unlikely that it should be possible to achieve a general applicability with a $k-\epsilon$ model, as the prospects of giving a realistic description of the dynamics in the boundary layer is small. The poor description of the physical mechanisms in a transitional boundary layer implies a restrictive use for applications which are different from the tested ones. Consequently, the models require a thorough testing and a detailed description of their limitations, before they can be used for any type of design purposes.

7.2 DSM-models

From a physical point of view DSM-models should have better prospects to describe the behaviour in a boundary layer than a two-equation model. The present study has been focussed on the use of Differential Reynolds Stress Models for transition prediction, and some of the more important findings can be summarized as follows:

(i) The HJH-model shows good predictions for zero-pressure gradient test cases at $Tu \approx 5-6\%$ (T3B and T3B-LES). Also the growth of $\overline{uu}$-stresses in the pseudo-laminar boundary layer is partly captured by the model.
(ii) Despite the good predictions at large Tu some severe shortcomings in the modelled terms are detected. A major problem seems to be an overestimation of the dissipation in the pre-transitional boundary layer. It is proposed that this deficiency is associated with the different characteristics of the fluctuations in the pseudo-laminar boundary layer as compared to turbulence at high Reynolds numbers.
(iii) As the level of Tu is reduced, the HJH-model predicts transition much further downstream compared with experiments. Still at a relatively high level of FST ($Tu = 3\%$) the predictions deviate considerably from the experiments. Comparisons with the empirical correlation by Abu-Ghannam & Shaw (1980) show that this is a continuous trend, i.e. the HJH-model predicts too early transition for $Tu > 6\%$ and too late for FST-levels below 5-6%.
(iv) Calculations with the SLY-model show that also this model predicts transition far too late as compared with experiments when the free-stream turbulence level is not very large. Our results are in conflict with existing other results, but in the present study it is shown that inappropriate free stream boundary conditions and the use of too small computational domains have affected those other studies.

The main outcome of the present work is somewhat discouraging, since both tested DSM-models can not correctly predict the transition location for a wide range of FST-levels. In fact, the results are worse than obtained with the Launder & Sharma $k-\epsilon$ model, at least as far as the location of the transition region is concerned. Earlier publications using the SLY-model (e.g. Savill 1995a), have shown very impressive results for a wide range of FST-levels (1–10%), and also good predictive capability at various pressure gradients. However,

the present study clearly shows that those results are too optimistic, as the model turns out to be extremely sensitive to the level of FST at the outer edge of the boundary layer, and only small changes in the decay rate of the turbulence can vary the start of transition dramatically. This can not be considered as a desirable characteristic, and it is difficult to see how the model can serve as a useful design tool for engineering applications, in which the flow conditions usually are less well-known.

Another DSM-model, which has to a smaller extent been tested in transitional test cases, is the model currently under development by Launder and co-workers. It has interesting properties, as it makes use of cubic pressure strain terms which do neither include the wall-distance, nor any wall-normal vectors. This is desirable for any turbulence model, since the implementation in unstructured grids, and thus the application to more complex geometries, becomes simplified if the model does not include explicit information of the position of the wall. The model is described in Launder & Li (1994), but is still continuously under development. A slightly different version of the model was applied to the T3A and the T3B-case (see Cho *et al.* 1995), which resulted in good predictions as far as the transition location is considered, but some problems with a large overshoot in c_f were observable at the end of the transition region.

7.3 Prospects for the future

In section 2.4 it was questioned whether the use of turbulence models for transition prediction has any prospects to become successful. Many experimental results show that the disturbances in the pseudo-laminar boundary layer are very different from turbulence, and some of the assumptions which are the basis for the currently used turbulence models are invalid in the pre-transitional region. The modelling of the dissipation equation is in many respects primitive, and the most frequently used version of the equation can be considered as a model of the energy transfer from the larger to the smaller scales in the turbulence. Consequently, it is assumed that the turbulence consists of a spectrum similar to the ones measured in experiments at high Re_t, and that the dissipation, which mainly takes place in the smaller scales, is determined by the larger energetic scales. This assumption is certainly not valid in the pseudo-laminar boundary-layer, which is dominated by large-scale, low-frequency motions. An improvement in the modelling might be possible by the use of multi-scale models, in which the introduction of additional length scales can give a better description of the disturbance spectra in the pseudo-laminar boundary layer.

However, it is likely that other deficiencies in the present approach will become visible if the modelling of the dissipation is improved. For instance, just prior to the start of the transition region, the LES-data shows a sudden increase in the pressure strain terms which redistribute energy from the streamwise to the lateral and vertical components. Most likely this redistribution is caused by some instability mechanism, and further understanding of the physics behind the breakdown of a boundary layer subjected to high levels of FST is probably necessary in order to improve the modelling. Since the breakdown stage is an intricate task to study experimentally, additional simulations (LES and DNS) is of highest importance.

Although some time-averaged effects of the growth of time-dependent disturbances can be included in a turbulence model, there are limitations associated with the Reynolds-averaged equations. A link between stability calculations and turbulence modelling may be the only approach which can give a sufficiently good description of the physics in a transitional boundary

layer.

Another approach, which might be of interest if a shorter time perspective is considered, is to develop alternative empirical data. At least to the author's knowledge, the presently used empirical correlations directly relate the transition location to parameters like free stream turbulence and pressure gradient coefficients. Maybe it could be fruitful to compare the development of the induced u-fluctuations and the fluctuation level just prior to the transition onset in a large number of experiments. If there exist some threshold values which can be related to different pressure gradients and FST-levels (this can not be expected to be the case at rather small Tu, but maybe at higher FST-levels), this could be used as a transition criteria. That would simplify the modelling work, which then could be focussed on the prediction of the fluctuations in the pre-transitional boundary layer.

Acknowledgements

The first author would like to thank Dr. R.A.W.M. Henkes for the invitation to Delft, and for the continuous support and encouragement during the course of the present study. He also wants to thank the students and the employees at the low-speed lab for a memorable year in Delft.

Dr. A.M. Savill is acknowledged for generously providing his computer code, as well as answering all questions and comments during the efforts to understand the reasons for the discrepancies between our results.

The visit of K.J.A. Westin to the Netherlands was supported by the Swedish Institute (SI) and the Swedish National Board for Industrial and Technical Development (NUTEK), and Dr. R.A.W.M. Henkes was supported by the Royal Netherlands Academy of Art and Sciences (KNAW).

Bibliography

ABU-GHANNAM, B. J. & SHAW, R. 1980 Natural transition of boundary layers – the effects of turbulence, pressure gradient, and flow history. *J. Mech. Eng. Sci.* **22** (5), 213–228.

ALFREDSSON, P. H. & MATSUBARA, M. 1996 Streaky structures in transition. In *Proc. Transitional Boundary Layers in Aeronautics*, (Henkes, R.A.W.M. & van Ingen, J.L., editors), pp. 373–386. Elsevier Science Publishers.

ARNAL, D. & JUILLEN, J. C. 1978 Contribution expérimentale à l'etude de la receptivité d'une couche limite laminaire, à la turbulence de l'écoulement general. ONERA Rapport Technique No 1/5018 AYD.

BAKCHINOV, A. V., WESTIN, K. J. A., KOZLOV, V. V. & ALFREDSSON, P. H. 1995 On the receptivity of a flat plate boundary layer to localized free stream disturbances. In *Laminar-Turbulent Transition* (Kobayashi, R., editor), pp. 341–348. Springer.

BERLIN, S. & HENNINGSON, D. S. 1994 A study of boundary layer receptivity to disturbances in the free stream. In *Bypass Transition - Proceedings from a Mini - Workshop* (Henningson, D. S., editor), pp. 29–41, Stockholm. TRITA-MEK, Technical Report 1994:14.

BERLIN, S., LUNDBLADH, A. & HENNINGSON, D. S. 1994 Spatial simulations of oblique transition in a boundary layer. *Phys. Fluids.* **6**, 1949–1951.

BOIKO, A. V., WESTIN, K. J. A., KLINGMANN, B. G. B., KOZLOV, V. V. & ALFREDSSON, P. H. 1994 Experiments in a boundary layer subjected to free stream turbulence. Part 2. The role of TS-waves in the transition process. *J. Fluid Mech.* **281**, 219–245.

BUTLER, K. M. & FARRELL, B. F. 1992 Three-dimensional optimal perturbations in viscous shear flow. *Phys. Fluids A.* **4**, 1637–1650.

CHO, J. R., CRAFT, T. J., LAUNDER, B. E. & SUGA, K. 1995 Development of turbulence models for transition prediction. *ERCOFTAC Bulletin.* **24**, 26–30.

DALY, B. J. & HARLOW, F. H. 1970 Transport equations in turbulence. *Phys. Fluids.* **13**, 2634–2649.

DICK, E. & VANCOILLIE, G. 1988 Simulation of instability of laminar flows with the $k-\epsilon$ turbulence model. *Int. J. Eng. Fluid Mechanics.* **1** (2), 151–167.

FRANZMANN, D. 1996 By-pass transition modelling based on an extended single-point closure. Technical Report TRITA-MEK 1996:4, Royal Institute of Technology, Stockholm.

GIBSON, M. M. & LAUNDER, B. E. 1978 Ground effects on pressure fluctuations in the atmospheric boundary layer. *J. Fluid Mech.* **86**, 491–511.

GULYAEV, A. N., KOZLOV, V. E., KUZNETSOV, V. R., MINEEV, B. I. & SEKUNDOV, A. N. 1989 Interaction of a laminar boundary layer with external turbulence. *Izv. Akad. Nauk SSSR, Mekh. Zhid. Gaza.* **5**, 55–65. (in Russian, English transl. 1990 in *Fluid Dyn.* **24**:5, 700–710).

HANJALIĆ, K., JAKIRLIĆ, S. & HADŽIĆ, I. 1995 Computation of oscillating turbulent flows at transitional Re-numbers. In *Turbulent Shear Flows 9*, (Durst, F., Kasagi, N., Launder, B. E., Schmidt, F. W., Suzuki, K. & Whitelaw, J. H., editors), pp. 323–342. Springer-Verlag.

HANJALIĆ, K. & LAUNDER, B. E. 1980 Sensitizing the dissipation equation to irrotational strains. *ASME J. Fluids Eng.* **102**, 34–40.

HENNINGSON, D. S. 1994 Bypass transition and linear growth mechanisms. In *Advances in Turbulence V* (Benzi, R., editor). Kluwer.

HENNINGSON, D. S. & REDDY, S. C. 1994 On the role of linear mechanisms in transition to turbulence. *Phys. Fluids.* **6**, 1396–1398.

HINZE, J. O. 1975 *Turbulence.* Second Edn. McGraw-Hill.

JAKIRLIĆ, S., HADŽIĆ, I. & HANJALIĆ, K. 1994 Computation of non-equilibrium and separating flows at transitional and high Re-numbers with a new low-Re-number second-moment closure model. In *Proc. Strömungen mit Ablösung*, AGSTAB, DGLR Congress, Erlangen, Germany.

JONES, W. P. & LAUNDER, B. E. 1972 The prediction of laminarization with a two-equation model of turbulence. *Int. J. Heat Mass Transfer.* **15**, 301–314.

KEBEDE, W., LAUNDER, B. & YOUNIS, B. A. 1985 Large amplitude periodic flow: A second moment closure study. In *Proc. 5th Turbulent Shear Flows Symposium*, Cornell, Ithaca.

KENDALL, J. M. 1985 Experimental study of disturbances produced in a pre-transitional laminar boundary layer by weak freestream turbulence. *AIAA Paper 85-1695.*

KREISS, G., LUNDBLADH, A. & HENNINGSON, D. S. 1994 Bounds for threshold amplitudes in subcritical shear flows. *J. Fluid Mech.* **270**, 175–198.

LANDAHL, M. T. 1975 Wave breakdown and turbulence. *SIAM J. Appl. Math.* **28**, 735–756.

LAUNDER, B. E. & LI, S. P. 1994 On the elimination of wall-topography parameters from second-moment closure. *Phys. Fluids.* **6** (2), 999–1006.

LAUNDER, B. E. & SHARMA, B. I. 1974 Application of energy-dissipation model of turbulence to the calculation of flow near a spinning disc. *Letters in Heat and Mass Transfer.* **1**, 131.

LUNDBLADH, A., HENNINGSON, D. S. & REDDY, S. C. 1994 Threshold amplitudes for transition in channel flows. In *Transition, Turbulence and Combustion Vol 1* (Hussaini, M. Y., Gatski, T. B. & Jackson, T. L., editors), pp. 309–318. Kluwer.

MACK, L. M. 1977 Transition prediction and linear stability theory. *AGARD Conference proceedings No. 224*, pp. 1.1–1.22, NATO, Paris.

MORKOVIN, M. V. 1969 The many faces of transition. In *Viscous Drag Reduction* (Wells, C. S., editor). Plenum Press.

ROACH, P. E. & BRIERLEY, D. H. 1992 The influence of a turbulent free-stream on zero pressure gradient transitional boundary layer development. Part I: Test cases T3A and T3B. In *Numerical Simulation of Unsteady Flows and Transition to Turbulence* (Pironneau, O., Rodi, W., Ryhming, I. L., Savill, A. M. & Truong, T. V., editors), pp. 319–347. Cambridge Univ. Press.

SAMUEL, A. E. & JOUBERT, P. N. 1974 A boundary layer developing in an increasingly adverse pressure gradient. *J. Fluid Mech.* **66**, 481–505.

SAVILL, A. M. 1992 A synthesis of T3 test case predictions. In *Numerical Simulation of Unsteady Flows and Transition to Turbulence* (Pironneau, O., Rodi, W., Ryhming, I. L., Savill, A. M. & Truong, T. V., editors), pp. 405–442. Cambridge Univ. Press.

SAVILL, A. M. 1995a The Savill-Launder-Younis (SLY) RST intermittency model for predicting transition. *ERCOFTAC Bulletin.* **24**, 37–41.

SAVILL, A. M. 1995b A summary report on the COST ERCOFTAC transition SIG project evaluating turbulence models for predicting transition. *ERCOFTAC Bulletin.* **24**, 57–61.

SAVILL, A. M. 1995c Transition modelling for turbomachinery III. Summary proceedings of the 3rd ERCOFTAC Transition SIG workshop of the BRITE-EURAM AERO-CT92-0052 project workshop on Transition in Turbomachinery.

SAVILL, A. M. 1996 One point closures applied to transition. In *Turbulence and transition modelling* (Hallbäck, M., Henningson, D. S., Johansson, A. V. & Alfredsson, P. H., editors), pp. 233–268. Kluwer.

SCHMIDT, R. C. & PATANKAR, S. V. 1991 Simulating boundary layer transition with low-Reynolds-number $k-\epsilon$ turbulence models: Part 2 – An approach to improve the predictions. *J. of Turbomachinery.* **113**, 18–26.

SIEGER, K., SCHIELE, R., KAUFMAN, F., WITTIG, S. & RODI, W. 1995 A two-layer turbulence model for the calculation of transitional boundary-layers. *ERCOFTAC Bulletin.* **24**, 21–25.

SMITH, A. M. O. & GAMBERONI, N. 1956 Transition, pressure gradient and stability theory. Technical Report ES 26388, Douglas Aircraft Co.

SO, R. M. C., LAI, Y. G., ZHANG, H. S. & HWANG, B. C. 1991 Second-order near-wall turbulence closures: A review. *AIAA Journal.* **29** (11), 1819–1835.

SPALART, P. R. 1988 Direct numerical simulations of a turbulent boundary layer up to $Re_\theta = 1410$. *J. Fluid Mech.* **187**, 61–98.

STEELANT, J. & DICK, E. 1996 Modelling of bypass transition with conditioned Navier-Stokes equations coupled to an intermittency transport equation. *Int. J. Num. Methods in Fluids.* **23**, 193–220.

VAN INGEN, J. L. 1956 A suggested semiempirical method for the calculation of the boundary layer transition region. Technical Report VTH-74, Department of Aeronautical Engineering, University of Delft.

VAN INGEN, J. L. 1977 Transition, pressure gradient, suction, separation and stability theory. *AGARD paper* 20, CP-224.

VOKE, P. R. & YANG, Z. 1995 Numerical study of bypass transition. *Phys. Fluids.* **7** (9), 2256–2264.

WESTIN, K. J. A., BOIKO, A. V., KLINGMANN, B. G. B., KOZLOV, V. V. & ALFREDSSON, P. H. 1994 Experiments in a boundary layer subjected to free-stream turbulence. Part I. Boundary layer structure and receptivity. *J. Fluid Mech.* **281**, 193–218.

WIEGHARDT & TILLMAN 1951 On the turbulent friction layer for rising pressure. Technical Report TM 1314, NACA.

YANG, Z. & VOKE, P. R. 1993 Large-eddy simulation of transition under turbulence. Technical Report ME-FD/93.12, Dept. Mech. Eng., University of Surrey.

Series 01: Aerodynamics

01. F. Motallebi, 'Prediction of Mean Flow Data for Adiabatic 2-D Compressible Turbulent Boundary Layers'
1997 / VI + 90 pages / ISBN 90-407-1564-5
02. P.E. Skåre, 'Flow Measurements for an Afterbody in a Vertical Wind Tunnel'
1997 / XIV + 98 pages / ISBN 90-407-1565-3
03. B.W. van Oudheusden, 'Investigation of Large-Amplitude 1-DOF Rotational Galloping'
1998 / IV + 100 pages / ISBN 90-407-1566-1
04. E.M. Houtman / W.J. Bannink / B.H. Timmerman, 'Experimental and Computational Study of a Blunt Cylinder-Flare Model in High Supersonic Flow'
1998 / VIII + 40 pages / ISBN 90-407-1567-X
05. G.J.D. Zondervan, 'A Review of Propeller Modelling Techniques Based on Euler Methods'
1998 / IV + 84 pages / ISBN 90-407-1568-8
06. M.J. Tummers / D.M. Passchier, 'Spectral Analysis of Individual Realization LDA Data'
1998 / VIII + 36 pages / ISBN 90-407-1569-6
07. P.J.J. Moeleker, 'Linear Temporal Stability Analysis'
1998 / VI + 74 pages / ISBN 90-407-1570-X
08. B.W. van Oudheusden, 'Galloping Behaviour of an Aeroelastic Oscillator with Two Degrees of Freedom'
1998 / IV + 128 pages / ISBN 90-407-1571-8
09. R. Mayer, 'Orientation on Quantitative IR-thermografy in Wall-shear Stress Measurements'
1998 / XII + 108 pages / ISBN 90-407-1572-6
10. K.J.A. Westin / R.A.W.M. Henkes, 'Prediction of Bypass Transition with Differential Reynolds Stress Models'
1998 / VI + 78 pages / ISBN 90-407-1573-4
11. J.L.M. Nijholt, 'Design of a Michelson Interferometer for Quantitative Refraction Index Profile Measurements'
1998 / 60 pages / ISBN 90-407-1574-2
12. R.A.W.M. Henkes / J.L. van Ingen, 'Overview of Stability and Transition in External Aerodynamics'
1998 / IV + 48 pages / ISBN 90-407-1575-0
13. R.A.W.M. Henkes, 'Overview of Turbulence Models for External Aerodynamics'
1998 / IV + 40 pages / ISBN 90-407-1576-9

Series 02: Flight Mechanics

01. E. Obert, 'A Method for the Determination of the Effect of Propeller Slipstream on a Static Longitudinal Stability and Control of Multi-engined Aircraft'
    1997 / IV + 276 pages / ISBN 90-407-1577-7
02. C. Bill / F. van Dalen / A. Rothwell, 'Aircraft Design and Analysis System (ADAS)'
    1997 / X + 222 pages / ISBN 90-407-1578-5
03. E. Torenbeek, 'Optimum Cruise Performance of Subsonic Transport Aircraft'
    1998 / X + 66 pages / ISBN 90-407-1579-3

Series 03: Control and Simulation

01. J.C. Gibson, 'The Definition, Understanding and Design of Aircraft Handling Qualities'
    1997 / X + 162 pages / ISBN 90-407-1580-7
02. E.A. Lomonova, 'A System Look at Electromechanical Actuation for Primary Flight Control'
    1997 / XIV + 110 pages / ISBN 90-407-1581-5
03. C.A.A.M. van der Linden, 'DASMAT-Delft University Aircraft Simulation Model and Analysis Tool. A Matlab/Simulink Environment for Flight Dynamics and Control Analysis'
    1998 / XII + 220 pages / ISBN 90-407-1582-3

Series 05: Aerospace Structures and Computional Mechanics

01. A.J. van Eekelen, 'Review and Selection of Methods for Structural Reliability Analysis'
    1997 / XIV + 50 pages / ISBN 90-407-1583-1
02. M.E. Heerschap, 'User's Manual for the Computer Program Cufus. Quick Design Procedure for a CUt-out in a FUSelage version 1.0'
    1997 / VIII + 144 pages / ISBN 90-407-1584-X
03. C. Wohlever, 'A Preliminary Evaluation of the B2000 Nonlinear Shell Element Q8N.SM'
    1998 / IV + 44 pages / ISBN 90-407-1585-8
04. L. Gunawan, 'Imperfections Measurements of a Perfect Shell with Specially Designed Equipment (UNIVIMP)
    1998 / VIII + 52 pages / ISBN 90-407-1586-6

Series 07: Aerospace Materials

01. A. Vašek / J. Schijve, 'Residual Strenght of Cracked 7075 T6 Al-alloy Sheets under High Loading Rates'
1997 / VI + 70 pages / ISBN 90-407-1587-4
02. I. Kunes, 'FEM Modelling of Elastoplastic Stress and Strain Field in Centre-cracked Plate'
1997 / IV + 32 pages / ISBN 90-407-1588-2
03. K. Verolme, 'The Initial Buckling Behavior of Flat and Curved Fiber Metal Laminate Panels'
1998 / VIII + 60 pages / ISBN 90-407-1589-0
04. P.W.C. Provó Kluit, 'A New Method of Impregnating PEI Sheets for the *In-Situ* Foaming of Sandwiches'
1998 / IV + 28 pages / ISBN 90-407-1590-4
05. A. Vlot / T. Soerjanto / I. Yeri / J.A. Schelling, 'Residual Thermal Stresses around Bonded Fibre Metal Laminate Repair Patches on an Aircraft Fuselage'
1998 / IV + 24 pages / ISBN 90-407-1591-2
06. A. Vlot, 'High Strain Rate Tests on Fibre Metal Laminates'
1998 / IV + 44 pages / ISBN 90-407-1592-0
07. S. Fawaz, 'Application of the Virtual Crack Closure Technique to Calculate Stress Intensity Factors for Through Cracks with an Oblique Elliptical Crack Front'
1998 / VIII + 56 pages / ISBN 90-407-1593-9
08. J. Schijve, 'Fatigue Specimens for Sheet and Plate Material'
1998 / VI + 18 pages / ISBN 90-407-1594-7

Series 08: Astrodynamics and Satellite Systems

01. E. Mooij, 'The Motion of a Vehicle in a Planetary Atmosphere'
1997 / XVI + 156 pages / ISBN 90-407-1595-5
02. G.A. Bartels, 'GPS-Antenna Phase Center Measurements Performed in an Anechoic Chamber'
1997 / X + 70 pages / ISBN 90-407-1596-3
03. E. Mooij, 'Linear Quadratic Regulator Design for an Unpowered, Winged Re-entry Vehicle'
1998 / X + 154 pages / ISBN 90-407-1597-1

3021857

Boundary layer transition induced by high levels of free stream turbulence (FST), so called bypass transition, can not be predicted with conventional stability calculations (e.g. the en-method). The use of turbulence models for transition prediction has shown some success for this type of flows, and the present study is a further investigation on the use of low-Reynolds number, single-point closures for transition prediction. The work is focused on two Differential Reynolds Stress Models (DSM), which are compared with the in previous studies more elaborately tested two-equation model by Launder Sharma. The results obtained with the DSM are relatively promising in some test cases, with a qualitatively correct description of the different normal stresses throughout the computational domain. However, the applicability of the models is very limited if a wider range of test cases are considered. Although the Differential Reynolds Stress Models have better prospects to describe the very anisotropic fluctuations that are observed in transitional boundary layers, the overall predictions of the location of the transition region are worse than obtained with the two-equation model. Detailed comparisons with results from Large Eddy Simulations have revealed significant shortcomings in the modelling of the dissipation. The DSM suffer from a large overprediction of the dissipation in the pre-transitional boundary layer, which also affects the modelling of the pressure strain terms. The present study also shows that some of the results reported in the literature may be too optimistic, since they seem to be affected by the implementation of the free stream boundary conditions. The predictions are sensitive to the FST-level in the vicinity of the boundary layer edge, and large variations in the predicted transition location can be obtained depending on how the free stream boundary is treated. The outcome of the present study indicates that, if single-point closures are going to be considered as a realistic transition prediction tool for industrial applications, some major improvements in the modelling are necessary.

ISBN 90-407-1573-4

DELFT AEROSPACE
ENGINEERING & TECHNOLOGY